LASER-DRIVEN MICRO-TRANSFER PRINTING FOR MEMS/NEMS INTEGRATION

BY

ALA'A MOUFAQ AL-OKAILY

DISSERTATION

Submitted in partial fulfillment of the requirements
for the degree of Doctor of Philosophy in Mechanical Engineering
in the Graduate College of the
University of Illinois at Urbana-Champaign, 2014

Urbana, Illinois

Doctoral Committee:

      Professor Placid Ferreira, Chair, Director of Research
      Professor John Rogers
      Professor Shiv Kapoor
      Professor Harley Johnson

ABSTRACT

Heterogeneous materials integration, motivated by material transfer processes, has evolved to address the technology gap between the conventional micro-fabrication processes and multi-layer functional device integration. In its basic embodiment, micro-transfer printing is used to deterministically transfer and micro-assemble prefabricated microstructures/devices, referred to as "ink," from donor substrates to receiving substrates using a viscoelastic elastomer stamp, usually made out of polydimethylsiloxane (PDMS). Thin-film release is, in general, difficult to achieve at the micro-scale (surface effects dominate). Furthermore, the release process becomes dependent on the receiving substrate's properties and preparation. Laser Micro-Transfer Printing (LMTP) is a laser-driven version of the micro-transfer printing process that enables non-contact release of the microstructure by inducing mismatch thermal stresses at the ink-stamp interface; making the transfer printing process independent from the properties or preparation of the receiving substrate. In this work, extensive studies are conducted to characterize, model, predict, and improve the capabilities of the LMTP process in developing a robust non-contact pattern transfer process.

Using micro-fabricated square silicon inks and varying the lateral dimensions and thickness of the ink, the laser pulse duration required to drive the delamination, referred to as "delamination time," is experimentally observed using high-speed camera recordings of the delamination process for different laser beam powers. The power absorbed by the ink is measured to estimate the total energy stored in the ink-stamp system and available to initiate and propagate the delamination crack at the interface. These experiments are used as inputs for an opto-thermo-mechanical model to understand how the laser energy is converted to thermally-induced stresses at the ink-stamp interface to release the inks. The modeling approach is based on first developing an analytical optical absorption model, based on Beer-Lambert law, under the assumption that optical

absorption during the LMTP process is decoupled from thermo-mechanical physics. The optical absorption model is used to estimate the heating rate of the ink-stamp system during the LMTP process that, in turn, is used as an input to the coupled thermo-mechanical Finite Element Analysis (FEA) model. Fracture mechanics quantities such as the Energy Release Rate (ERR) and the Stress Intensity Factors (SIFs) are estimated using the model. Then, the thermal stresses at the crack tip, evaluated by the SIFs, are decomposed into two components based on originating causes: CTE mismatch between the ink and the stamp, and thermal gradient within the PDMS stamp.

Both the delamination time from the high-speed camera experiments and thermo-mechanical FEA model predictions are used to understand and improve the process's performance under different printing conditions. Several studies are conducted to understand the effect of other process parameters such as the dimensions and materials of the stamp, the ink-stamp alignment, and the transferred silicon ink shape on the process performance and mechanism. With an objective of reducing the delamination time, the delamination energy, and the temperature of the ink-stamp interface during printing, different patterned stamp designs (cavity, preloading, and thin-walls) have been proposed. Cavity, preloading, and thin-wall stamps are designed to generate thermally-induced air pressure at the ink-stamp interface, to store strain energy at the interface, and to generate thermally-induced air pressure at the preloaded interface, respectively. Cohesive Zone Modeling (CZM) based models are developed to estimate the equilibrium solution of the collapsed patterned stamp after the ink pick-up process, and to evaluate the patterned stamps' performance during the LMTP process. The patterned stamps show significant improvements in delamination times and delamination energies (up to 35%) and acceptable improvement of the interface temperature at the delamination point (up to 16%) for given printing conditions.

For My Parents

ACKNOWLEDGMENTS

LIST OF FIGURES

x

xiii

LIST OF TABLES

NOMENCLATURE

A_a Area of an aperture that has the same dimensions as the ink

E^* Equivalent ink-stamp interface Young's modulus

E_d Energy required to drive delamination

E_p Young's modulus of the stamp

E_s Young's modulus of the ink

G Energy release rate value

G_c Critical energy release rate value

G_I Opening mode (mode I) energy release rate

G_{II} Shear mode (mode II) energy release rate

H_c Cavity stamp feature height

H_{cd} Dimensionless number of cavity stamp feature height

H_l Preloaded stamp feature height

H_{ld} Dimensionless number of preloaded stamp feature height

H_t Thin-wall stamp feature height

h_p Height of PDMS stamp post

h_s Thickness of silicon ink

I Intensity of Gaussian laser beam on ink surface

I_a Intensity of uniform laser beam on ink surface

$I_{i,B}$ Intensity of uniform laser beam at the beginning of the ith internally-reflected pass

$I_{i,E}$ Intensity of uniform laser beam at the end of the ith internally-reflected pass

I_o Intensity of Gaussian laser beam on ink surface at the center axis

J J-integral value

K_I Opening mode (mode I) stress intensity factor value

K_{II} Shear mode (mode II) stress intensity factor value

k Vector outward normal to the Γ integration path

L_p Size of square PDMS stamp post

L_s Size of square silicon ink

n Number of internally-reflected passes

n_a Index of refraction of air

n_p Index of refraction of PDMS

n_s Index of refraction of silicon

P_a Power of laser beam incident on the ink

P_b Power of laser beam absorbed by ink

P_i Power absorbed by the ink on the ith internally-reflected pass

Q_i Power density absorbed by the ink on the ith internally-reflected pass

R Ratio of post to ink size

R_s Surface reflectivity

R_B Reflectivity of ink bottom surface

R_T Reflectivity of ink top surface

r_o Radius of an aperture that has the same ink size

r_p Radius of equivalent area of the axisymmetric PDMS stamp

r_s Radius of equivalent area of the axisymmetric silicon ink

S_c Cavity stamp size

S_{cd} Dimensionless cavity stamp size

S_l Preloaded stamp's step size

S_{ld}	Dimensionless preloaded stamp size
S_{t1}	Thin-wall stamp inner diameter
S_{t2}	Thin-wall stamp outer diameter
T	Traction vector normal to the interface
T_{max}	Maximum traction in traction-separation curve
t_d	Laser pulse duration required to start delamination of ink
U	Strain energy density
u	Displacement vector
v_p	Poisson's ratio of the stamp
v_s	Poisson's ratio of the ink
W_I	Opening mode (mode I) interfacial work of adhesion value
W_{II}	Shear mode (mode II) interfacial work of adhesion value
w_o	Radius of Gaussian laser beam at the focus plane
α	Optical absorption coefficient of ink
β	Second Dunder's parameter for interface Young's modulus mismatch
Γ	Integration path for j-integral
δ	Interface separation
δ_{max}	Maximum separation in traction-separation curve

CHAPTER 1: INTRODUCTION

1.1 MEMS/NEMS Integration

Micro/Nano-Electro-Mechanical Systems (MEMS/NEMS) fabrication has evolved to become a key technology for developing electro-mechanical functional devices for sensing and actuation. MEMS/NEMS technology has been used to realize many functional devices in many engineering fields such as bio-engineering (i.e. micro-fluidic devices and micro-needles), optics and display (i.e. imaging sensors, optical switches, and optical resonators), energy conversion (i.e. micro-fuel-cells, 3D photovoltaic devices, and energy harvesters), radio frequency (i.e. switches, transmitters/receivers, and antennas), and chemical analysis (i.e. tuned-wavelength optical sensors). A wide selection of materials (semiconductors, ceramics, metals, and polymers) is involved in the fabrication of MEMS/NEMS devices through a series of multi-layer material patterning processes (deposition, photo-lithography, and etching). The thermal, chemical, and mechanical compatibility and the etching selectivity of the different multi-layered materials have always been an issue, limiting the fabrication process development and the device functionality. Therefore, heterogeneous material integration has been introduced as an alternative approach to micro-assemble prefabricated devices/structures to eliminate the need for compatibility and selectivity in multi-layer devices, to enhance the device's functionality, and to improve the process yield. Various techniques have been introduced to achieve heterogeneous material integration using different methods of collecting, handling, and releasing the devices/structures. Transfer printing technology, due to its simplicity, accuracy, repeatability, and large-scale material integration, is rapidly emerging as an effective pathway to achieve large-scale heterogeneous material integration.

"Micro-transfer printing," as a parallel micro-assembly process, transfers prefabricated micro/nano-scale structures/devices, referred to as "ink," from growth donor substrates to functional receiving substrates. As a primary means of heterogeneous integration, Micro-transfer printing enables various applications such as flexible, stretchable, and large-area electronics, bio-integrated sensing, and energy harvesting and conversion. Figure 1.1 shows some examples of functional devices that would be difficult or impossible to realize using conventional semiconductors or MEMS/NEMS fabrication approaches. Micro-transfer printing leverages the convectional lithography-based techniques to produce dense arrays of different functional inks (i.e. thin-films, transistors, LEDs). The inks are partially undercut to hold the inks in place while they are easy to release from the growth donor substrate. Then, a viscoelastic elastomer tool, referred to as a "stamp," with micro-patterned posts, usually made out of PDMS, is used to selectively pick up the prefabricated structures from the donor substrates and transfer them to the receiving substrates. Different techniques have been developed to release ink materials and structures from the post, and transfer them to receiving substrates made from different materials. For example, in the basic "micro-transfer printing," inks are released from the stamp by kinetically controlling the interface strength [1]; while in "microtipped transfer printing," inks are released by controlling the contact area and geometry of the interface [2] (more details are discussed in Chapter 2). In "Laser Micro-Transfer Printing (LMTP)," thermally-induced stresses at the contact interface are used [3] [4]. As a non-contact process, LMTP provides important new capabilities to transfer printing technology making it independent from the properties and preparation of the surface of the receiving substrate.
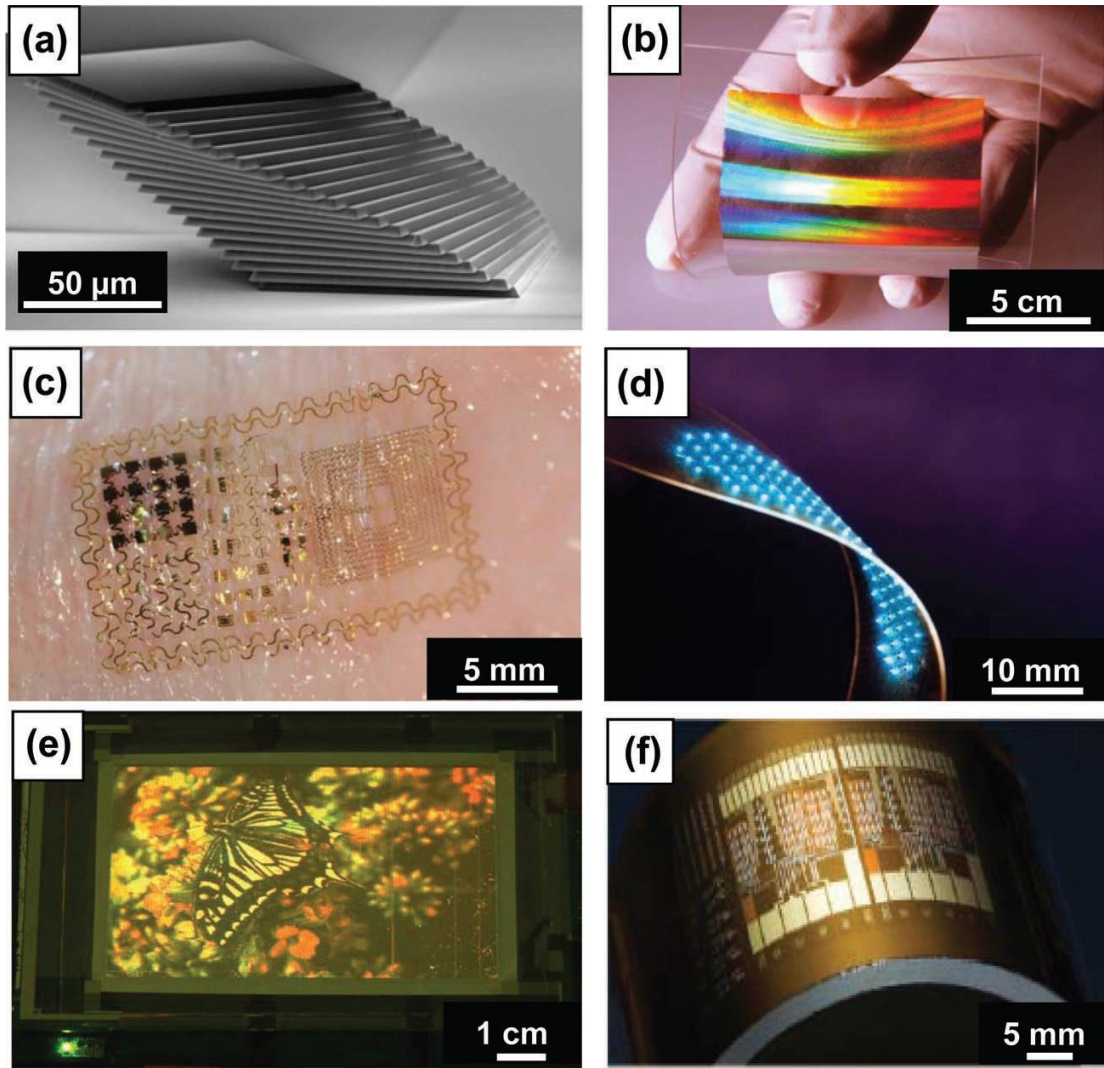
Figure 1.1. Examples of uncommon constructs, devices, and integrated systems realized by micro-transfer printing: (a) SEM image of a printed multilayer stack of silicon platelets [2]; **(b)** photograph of a large area (10×10 cm) Negative Index Metamaterial (NIM) comprised of alternating layers of Ag and MgF_2 in a nano-scale fishnet pattern printed onto a flexible substrate [5]; **(c)** photograph of an "epidermal" electronic device, conformally laminated onto the surface of the skin. The key components of the system: radio frequency antennae, inductive coils, inductors, capacitors, silicon diodes, strain gauges, Light Emitting Diodes (LEDs), temperature sensors, electrophysiological sensors, and field effect transistors, are all fabricated by transfer printing; **(d)** image of a mechanically flexed array of ultrathin, micro-scale, blue LEDs printed from a source wafer onto a thin strip of plastic [6]; **(e)** picture of a 4-inch, full-color Quantum Dot (QD) LED display that uses printed collections of QDs in an active matrix configuration of 320×240 pixels [7]; and **(f)** photograph of a flexible integrated circuit (four-bit decoder composed of 88 transistors) that uses printed networks of single walled carbon nanotubes for the semiconductor [8]. (Composite figure taken from [9]).

1.2 Laser Micro-Transfer Printing

The LMTP printing cycle steps are shown in Fig. 1.2 where a stamp, made of a material transparent to the laser, is positioned to pick up ink from the donor substrate using Van der Waals forces (Fig. 1.2-a and 1.2-b). The stamp is then moved to the placement location and positioned at a specified stand-off distance from the receiving substrate (Fig. 1.2-c). A laser beam, focused on the ink through the stamp, is pulsed for a specified time to produce local heating at the ink-stamp interface, leading to the delamination and transfer of the ink to the receiving substrate (Fig. 1.2-d).

Because the stamp (typically PDMS) is transparent to the laser (805 nm wavelength), the radiation absorbed by the ink heats up the interface and PDMS post. The thermally-induced stresses drive the delamination process, causing the ink-stamp interface to crack, which leads to ink being released from the stamp. The generated stresses have two components: one is due to the Coefficient of Thermal Expansion (CTE) mismatched between the ink and the stamp (For example, silicon has a CTE of 2.6 ppm/°C and PDMS has a CTE of 310 ppm/°C), and another is because of temperature gradients within the PDMS stamp. This process has been successfully demonstrated to print different ink materials such as Si and GaAs printed on textured, curved, and partial surfaces and even on liquids and free-standing structures [3] as shown in Fig. 1.3 and 1.4. Because the LMTP is one of the more recently introduced transfer printing technologies, the focus of this dissertation is on studying the process behavior with an objective of developing a non-contact robust manufacturing process for heterogeneous material MEMS integration.
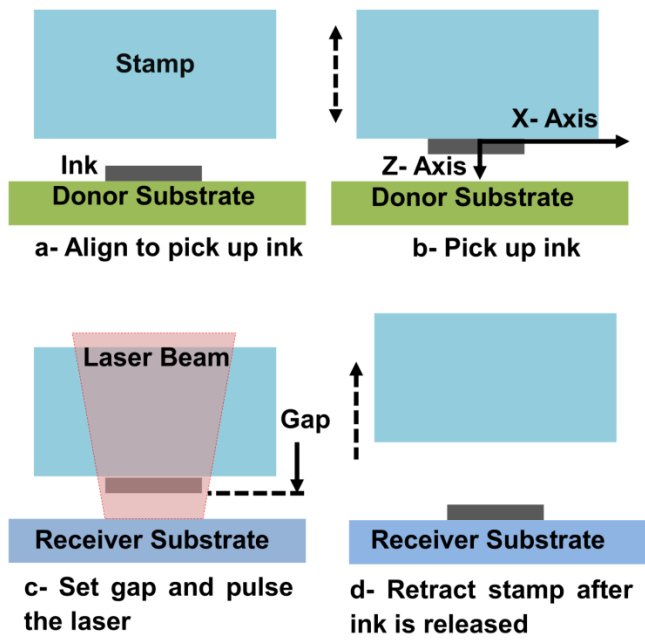
Figure 1.2. A typical laser micro-transfer printing cycle.
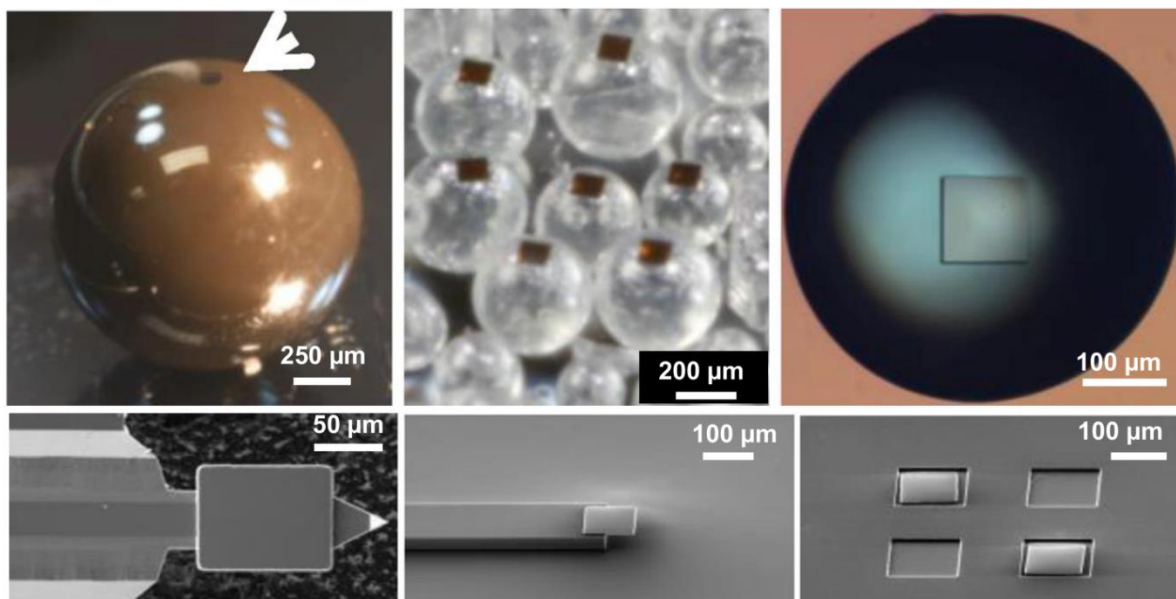
Figure 1.3. Examples of printing on different surfaces: (left-top) printing on a single 1 mm ceramic sphere; (middle-top) printing on a non-uniform array of 500 µm silica beads; (right-top) printing on to a liquid NOA droplet; (left-bottom) a silicon square printed on to a AFM cantilever, demonstrating assembly on an active structure; (middle-bottom) printing on a ledge; and (right-bottom) printing into recessed spaces. (Composite figure taken from [3]).
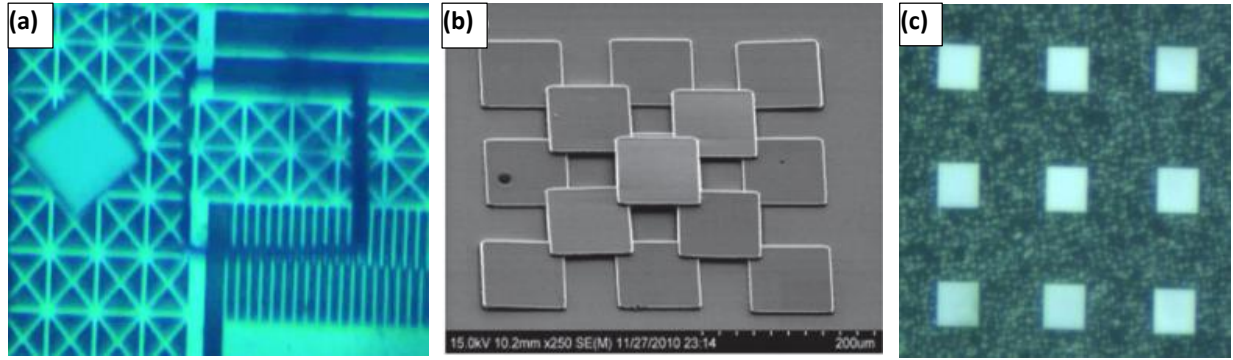
Figure 1.4. Examples of printing different microstructures using LMTP process: (a) 200×200×50 μm ink printed on MEMS a nano-positioning's suspended structure as a proof mass form calibration; (b) printing 3D microstructures of 100×100×3 μm inks [3]; and (c) printing 2D array of 100×100×3 μm inks.

1.3 Research Objectives

The proposed thesis research seeks to develop a robust laser-driven heterogeneous material integration module based on the LMTP process. Therefore, the objectives of this research are:

➢ To develop a laser-driven heterogeneous material integration printer to automate the print cycle and achieve high integration throughput, accuracy, and repeatability.

➢ To characterize, model, and predict the LMTP opto-thermo-mechanical induced delamination process at the ink-stamp interface by:

- developing a two-stage multi-physics model (Stage I: opto-thermal analytical model to estimate the ink heating rates from absorbed laser power, Stage II: thermo-mechanical Finite Element Analysis (FEA) model to understand the effect of the thermal strains on the delamination process) to understand the LMTP process behavior,

- conducting a series of experiments to study the effect of the major process parameters (ink's geometry and dimensions, stamp's geometry, dimensions, and PDMS formulation, and laser beam power) on the delamination process performance, and,

6

- using the developed models and experimental procedures to characterize the delamination in the LMTP process.

➤ To use the developed models to improve and optimize the LMTP process performance (reduce time and energy required to drive the delamination, reduce interface temperature at delamination point, and enhance the thermo-mechanical energy conversion).

1.4 Impact of Research

The proposed work will lead to the development of a comprehensive understanding of the LMTP process to be able to print functionally active devices, thereby investigating the issues of high temperature printing, and energy conversion during printing. The results will be used as a guideline to plan the LMTP process control parameters, and study the effect of the process parameters on the printing process performance. Moreover, characterizing the delamination process during the printing will provide a fundamental tool to understand the process's capability to improve and mature the LMTP process to be used as a standard industrial tool for MEMS/NEMS integration.

Further, the proposed work will have an impact on developing the laser-based MEMS/NEMS integration module (LMTP process and laser-induced bonding). Therefore, the work should enhance the robustness of transfer printing technology to account for complex functional devices by using conventional micro-transfer printing (printing on a polymeric substrate), LMTP (non-contact printing on different substrate form factors), and laser-induced bonding (intermediate step among the assembled layers). Such a module will eliminate the need for post-processing steps currently required for multi-layer or low adhesion substrate bonding. Furthermore, it will improve the material integration process accuracy and repeatability because the printing (either micro-transfer printing or LMTP) and laser-induced bonding can be performed in the same setup.

1.5 Dissertation Organization

Chapter 2 consists of a literature review of micro-assembly integration, laser-based micro-fabrication processes, recent research on micro-transfer printing technology, as well as LMTP processes, and fracture mechanics of the delamination.

Chapter 3 describes the LMTP printer design, and the developed experimental approach to characterize the LMTP process performance by measuring the laser pulse time and energy required to drive the delamination, and the power absorbed by the ink.

Chapter 4 describes the multi-physics model that is used to understand the opto-thermo-mechanical delamination process at the ink-stamp interface with an objective of understanding the delamination process mechanism.

In Chapter 5, several studies are conducted to understand the effects of other LMTP process parameters such as the dimensions and materials of the stamp, the ink-stamp alignment, and the transferred silicon ink shape on the process performance and mechanism.

Chapter 6 introduces novel patterned stamp designs with an objective of enhancing the process performance by reducing the laser pulse time and energy required to drive the delamination, and the interface temperature at the delamination point.

Chapter 7 summarizes the conclusions of the dissertation and the recommendations for future work.

CHAPTER 2: LITERATURE REVIEW

2.1 Micro-Integration Technologies

Originally, MEMS and IC semiconductor fabrication technologies have evolved and optimized to produce uni-functional micro/nano-scale devices such as memory chipsets, logic processors, RF modulation chips, sensors, and actuators. The need for small-scale multi-functional integrated devices, where either dual technologies (MEMS and IC semiconductors) or different fabrication schemes within the same technology are used, has become a challenge due to the increasing complexity of the devices. Although the fabrication technologies for micro/nano-scale uni-functional devices are well established, such devices require a macro-scale packaging interface to different/components and with the external environment. These challenges have introduced the concept of "multi-functional device integration," where different fabrication technologies are used to make heterogeneously-integrated functional devices. Figure 2.1 shows the schemes for the different multi-functional device integration methods (monotonic, hybrid, and heterogeneous). The monotonic integration technology is usually achieved by increasing the number of sequential layers on the same wafer [10-12]. The monolithic integration can be classified based on the fabrication order into "MEMS/IC mixed," "MEMS post IC," or "IC post MEMS" approaches. Because monolithic integration methods are complex and reduce process yield, a hybrid functional integration approach [13] was first proposed to account for these issues by fabricating devices/structures on different donor wafers and then transferring them to a functional substrate. For hybrid-functional integration, the devices/structures are integrated side-to-side and the electrical interconnects are introduced through wire bonding or a bonding substrate [13]. Further, hybrid integration can be achieved by integrating devices (not wafer scale) vertically using "Through-Substrate-Vias (TSV)" [14] [15]. As a follow up from hybrid integration, heterogeneous

integration was proposed to address the issue of the material incompatibility and to improve the process yield for wafer-scale integration [16-18]. Further, 3D heterogeneous integration can be used to integrate multi-layer devices and interconnect those using TSVs. Therefore, the development of micro-scale multi-layer heterogeneous assembly, bonding, and packaging processes is considered to be one of the most challenging issues in this field.
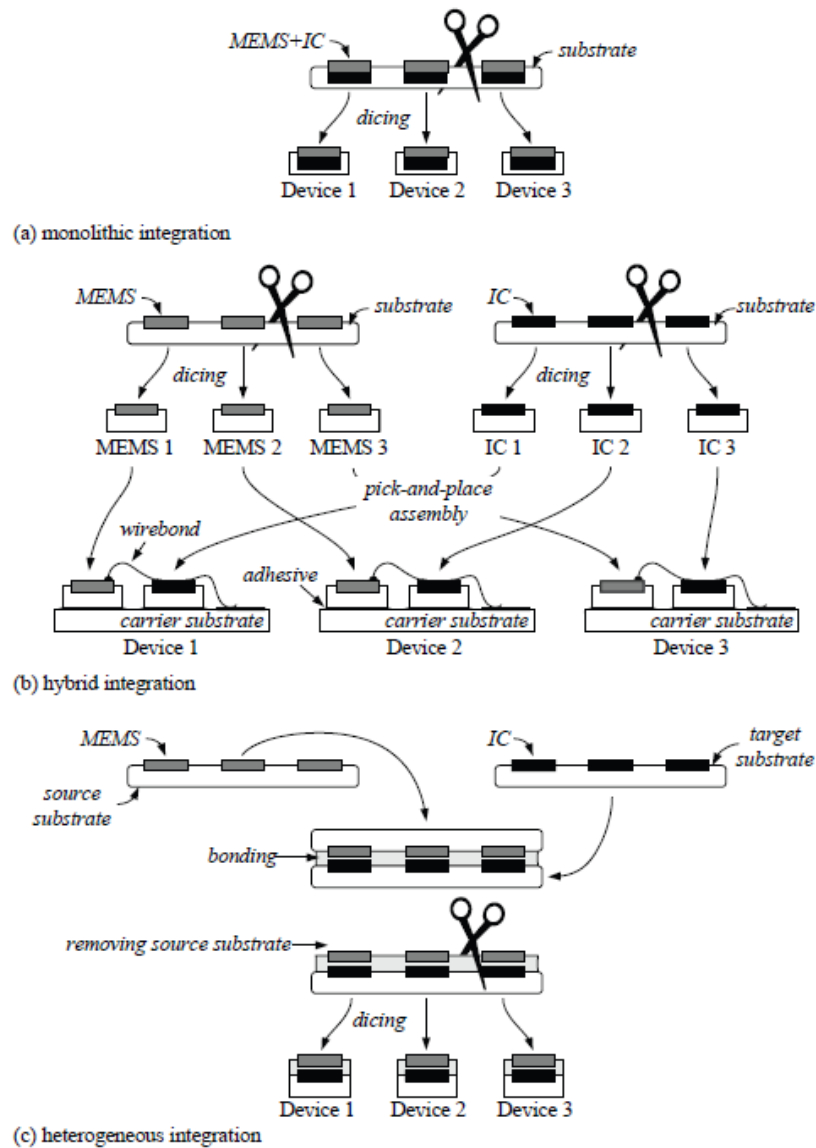
Figure 2.1. Schemes for the different multi-functional device integration methods (monotonic, hybrid, and heterogeneous) [38].

2.1.1 Micro-Scale Assembly

To achieve hybrid or heterogeneous integration, several micro-assembly methods have been used. These methods can be classified as:

➢ Hinged MEMS integration: This technique is developed to micro-assemble either fixed or movable hinged devices, which are usually produced using MEMS surface micromachining processes [19] [20]. Different techniques have been used to achieve hinged micro-assemblies such as on-chip-actuation [10] (i.e. comb-drives, and vibro-motors were used to push hinges into assembly position), hinge creation [21] (i.e. resistive heating), and external actuation methods [22-24] (i.e. fluidic agitation, ultrasonic forces, magnetic deflection, polymer shrinkage, and surface tension of droplets).

➢ Serial (pick-and-place) micro-assembly: The devices/structures are individually picked up from a donor substrate and then placed into a receiving substrate. Because the dominant force at the micro-scale (surface tension, electrostatic, and Van der Waals) are different from those at the macro-scale (gravitational and inertial forces), new micro-gripper designs are needed to overcome the gripping adhesion. The most common methods are serial robotic micro-assembly methods using mechanical [25] [26], optical [27] [28], electrical [29] [30], aerodynamic [31], or magnetic [20] [32] transfer and release mechanisms.

➢ Parallel micro-assembly: serial micro-assembly techniques suffer from low throughput and high cost due to the need for handling and manipulating each component individually, parallel micro-assembly methods have evolved. These processes can assemble many components simultaneously. Parallel micro-assembly methods can also be sub-classified into stochastic and deterministic processes:

- Stochastic micro-assembly: The assembled devices/structures and the receiving substrate have special geometrical features that facilitate the self-assembly using different techniques such as fluidic agitation and mating part shapes, vibratory agitation and electrostatic force fields, vibratory agitation and mating part shapes, centrifugal forces, and mating patterns of self-assembling monolayers [33] [34].

- Deterministic micro-assembly: These methods are designed to pick up larger numbers of devices/structures, usually at wafer level, then systemically release all of them simultaneously [25] [30]. The most common ways to achieve this are by using flip-chip wafer-to-wafer transfer [21] [35] and micro-gripper array mechanisms [36].

➢ Collect-and-place micro-assembly: In this type, many devices are continually or simultaneously collected. However, each device is individually released [37].

2.1.2 Micro-Scale Bonding

Bonding as a post-processing step for micro-assembled devices/structures are required to hold the assembled devices in place and to establish interconnects with the other devices. Many bonding methods such as soldering [39-41], metal welding [41] [42], ceramic bonding [41], adhesive bonding [41] [43], and wafer-level bonding [41] (i.e. anodic [44], fusion [45], eutectic [45] [46], via-first and via-last solder bonding [40]) have been used. Because most of the bonding techniques require higher temperatures, compared to room temperature, for the bonded stack at the interface, different energy supply mechanisms such as electromagnetic inductive heating [47], resistive heating [21], uniform furnace heating [46], ultrasonic vibration [48] and laser beam [49] [50] bonding have been investigated.

2.2 Micro-Scale Laser-Induced Fabrication Processes

Lasers, as coherent light sources with narrow bandwidths, are commonly used in micro/nano-scale fabrication due to their non-contact, high power, instant, and localized nature. Table 2.1 lists some of the micro/nano-scale processes in which laser beams are used. Photo-lithography is a standard fabrication technique that is used to transfer patterns on photosensitive polymer, known as photoresist, by using masks. In photo-lithography, the photoresist is exposed with a single wavelength source of light (usually UV light). Both lasers and incoherent light sources can be used to expose the photoresist. On the other hand, many maskless lithography techniques such as laser, X-ray, electron beam, and focused ion beam lithography methods are also proposed to direct-write patterns without the need for a mask.

Laser Direct-Write (LDW) processes are a class of fabrication processes that use a focused laser beam to create two- and three-dimensional patterns by modifying, subtracting, or adding materials without the need for pattern transfer through a mask. The LDW processes are used to create patterns by a series of spot-by-spot interaction with the material, where the relative location of the laser beam to substrate is precisely controlled. This can be achieved either by moving the substrate while the laser beam is stationary or scanning the laser beam while the substrate is held to create the desired patterns. Leveraging the non-contact and instantaneous laser-material interaction, LWD processes are used to create micro/nano-scale masters for molding or producing patterns (photoresist or film patterning). Based on the physical and chemical interaction between the laser and the substrate, the LDW process can be classified into [51]:

➤ Laser Direct-Write Subtraction (LDW⁻): A laser beam is used to provide enough energy to remove the material by photo-chemical, photo-physical, or/and photo-thermal ablation (i.e. laser micromachining and Laser-Induced Backside Wet Etching (LIBWE)).

Table 2.1. Laser based micro-scale fabrication process.

Process	Process Type	Purpose of Laser	Capabilities	Reference
Laser micromachining	Subtractive	Material removal by laser ablation	Wide range of material can be machined to produce 2D and 3D microstructures with high accuracy	[54] [55]
Laser-assisted chemical etching	Subtractive	Thermal activation of the reaction or active etchant species (photo- or pyrolytic-activation)	Enhance etching rate for silicon and metals to achieve selective etching	[56]
Laser Chemical Vapor Deposition (LCVD)	Additive	A laser beam thermally activates the CVD to deposit metals	Selectively deposition	[57]
Stereolithograpy (SLA)	Additive	A laser beam locally solidifies a polymer resin material (layer-by-layer)	Create 3D complex polymeric structures	[58]
LIFT micro-assembly	Additive	A laser beam transfers or releases prefabricated structures	Transfer, release, and bond of thin films	[59] [60]
LIFT	Additive	A laser beam initiates the process of material transfer and deposition	Wide-range material deposition and transfer	[52]
Laser bonding	Modification	A laser is used as an energy source for bonding	Non-contact bonding	[61]
Pulsed Laser Deposition (PLD)	Additive	A laser is used to evaporate target material to be deposited onto the target substrate	Material deposition	[62]
Laser-LIGA	Modification or subtractive	Patterns are created on a polymeric substrate, then a metal film is deposited	Master mold is used for mass production of metallic structure replication	[63]
Laser-assisted dicing	Modification	A pulsed laser is introduced to internally transform the material structure, then the material is separated by applying pressure only	Clean and dry process for wafer scale dicing	[64]

Table 2.1. Laser based micro-scale fabrication process (Cont.).

Process	Process Type	Purpose of Laser	Capabilities	Reference
Laser-assisted annealing	Modification	-A laser is introduced during poly-silicon growth to produce larger grains -Surface annealing of metallic structures	-Improve charge mobility in poly-silicon -Relief internal stresses	[65]
Laser surface handing	Modification	A pulsed laser is used to locally raise the temperature above the recrystallization point to harden surface	Selective and accurate hardening	[66]

➢ Laser Direct-Write Modification (LDWM): The energy provided by the laser beam is not enough to remove the material but it can modify the material's structural or chemical properties (for example, laser surface hardening, Selective Laser Sintering (SLS)).

➢ Laser Direct-Write Addition (LDW⁺): The laser energy is used to add material by the laser-substrate interaction (for example, Laser-Induced Forward Transfer (LIFT) and Laser-Induced Chemical Vapor Deposition (LICVD)).

Because the LMTP can be considered as a LDW⁺ micro-assembly process, other LDW⁺ micro-assembly processes (mainly LIFT) are discussed further to provide more insight into the LMTP process capabilities. Originally, the LIFT process was introduced in 1986 by Bohandy et al. [52] to deposit metals from a metal-coated fused silica donor substrate onto a receiving substrate using laser ablation. Therefore, the LIFT process can be considered as a LDW⁺ in which the material transfers to a receiving substrate after it has been melted from the donor substrate using laser-induced vapor pressure. Because the transferred materials usually experience high temperatures,

due to melting or evaporation, several modifications (see Fig. 2.2) were introduced to print temperature sensitive materials, such as [53]:

➢ Dynamic Release Layer (DRL)-assisted LIFT: A DRL is added between the transferred material and the donor substrate. The DRL (i.e. polyimide) should absorb the laser wavelength while having a low melting temperature. The advantage of using the DRL-assisted LIFT is that a lower temperature is required for the material transfer.
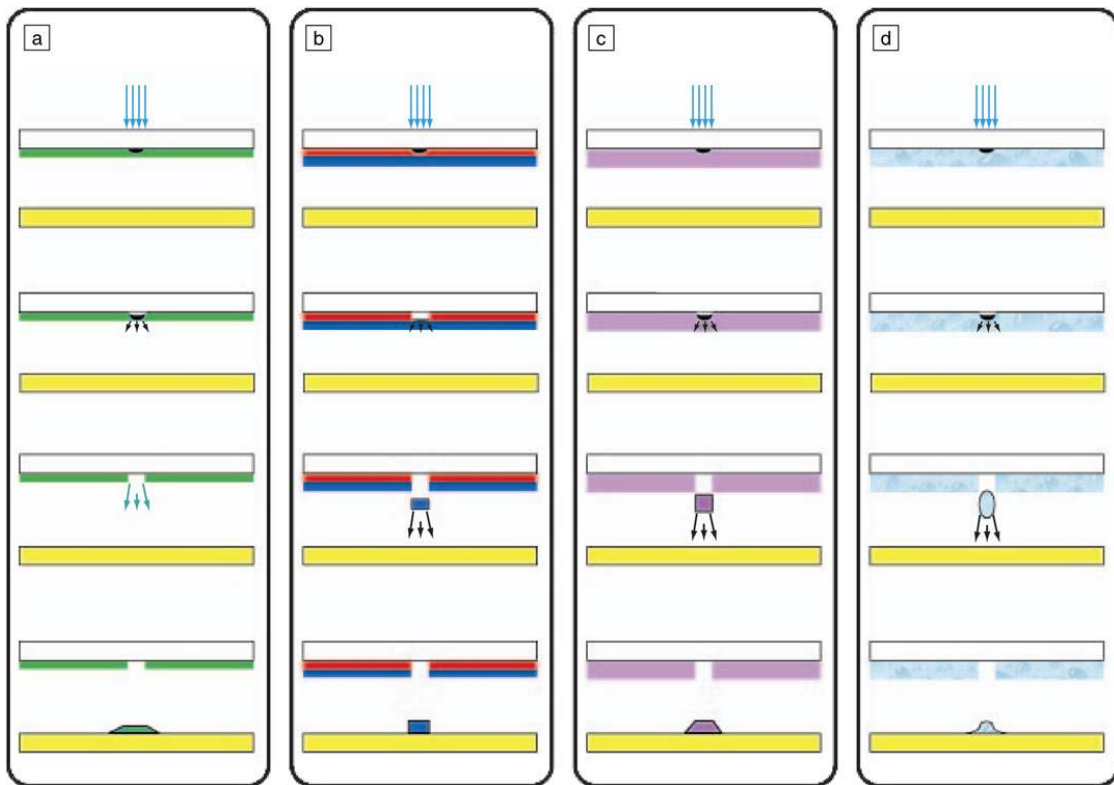
Figure 2.2. Schematic illustration of LDW$^+$ mechanisms. In all parts, the receiving substrate is pictured in yellow, (a) traditional LIFT, in which the laser vaporizes the entire thin film in the region of laser focus, (b) LIFT with a dynamic release layer (DRL) (red) that is vaporized and propels the intact film (blue) forward, (c) Matrix-Assisted Pulsed Laser Evaporation Direct-Write (MAPLE-DW), in which the laser is absorbed by a sacrificial matrix (not shown) that must be removed after deposition, and (d) LDW$^+$ printing of rheological systems in which the laser is absorbed by a thin layer near the substrate and propels the remaining ink forward [53].

➢ Matrix-assisted LIFT: An absorbing powder is mixed with an organic or polymer binder to create a matrix. The matrix is then coated uniformly onto the donor substrate. During the laser heating, the powder is evaporated by the laser beam leading to transfer the binder to the receiving substrate. The advantage of using the matrix-assisted LIFT is that thicker material layers can be transferred.

➢ Multi-component or multi-phase-assisted LIFT (also known as rheological systems): The transfer material is dissolved or suspended in a liquid/gel medium to produce multiphase or multi-component ink. The ink is then coated uniformly onto the donor substrate where the liquid/gel is completely or partially evaporates by the laser beam leading to transfer the material to the receiving substrate.

In most LIFT processes, pulsed lasers with different wavelengths and pulse durations were used to print different materials as shown in Table 2.2. In contexts of MEMS integration, the DRL-assisted LIFT process (see Fig. 2.3) was used to transfer and bond prefabricated metallic microstructures to realize hybrid structure integration [59] [60]. The LMTP process has a similar process scheme and operational principle, compared to the LIFT micro-assembly process. However, the LMTP release mechanism, as shown in [4], is based on interfacial delamination of the ink driven by laser-induced thermal strains. Therefore, the advantages of using the LMTP process over the LIFT process as micro-assembly methods are as follows:

➢ Because LMTP is a delamination based process, the required energy and temperature to release the pattern, especially thin films, are lower. This follows from the fact that a Near-Infrared (NIR) continuous diode laser source is used in the LMTP process, where high power with short pulse Excimer lasers are usually used in LIFT to induce ablation of the film.

17

➢ The LMTP process does not require pre-processing steps to attach the pattern to the donor substrate because a standard PDMS tool is used to pick up the structures/devices.

➢ The LMTP process does not require post-processing cleaning steps to remove the residue after the DRL ablation.

Because the laser beam is integrated for the setup, laser bonding for dissimilar materials can be performed on the same setup. Therefore, laser bonding, as the non-contact localized heating bonding method, has advantages in reducing the mismatch in the thermally-induced strain, generating a shallow heat affected zone, and increasing the bonding process yield [50] [61] [67].
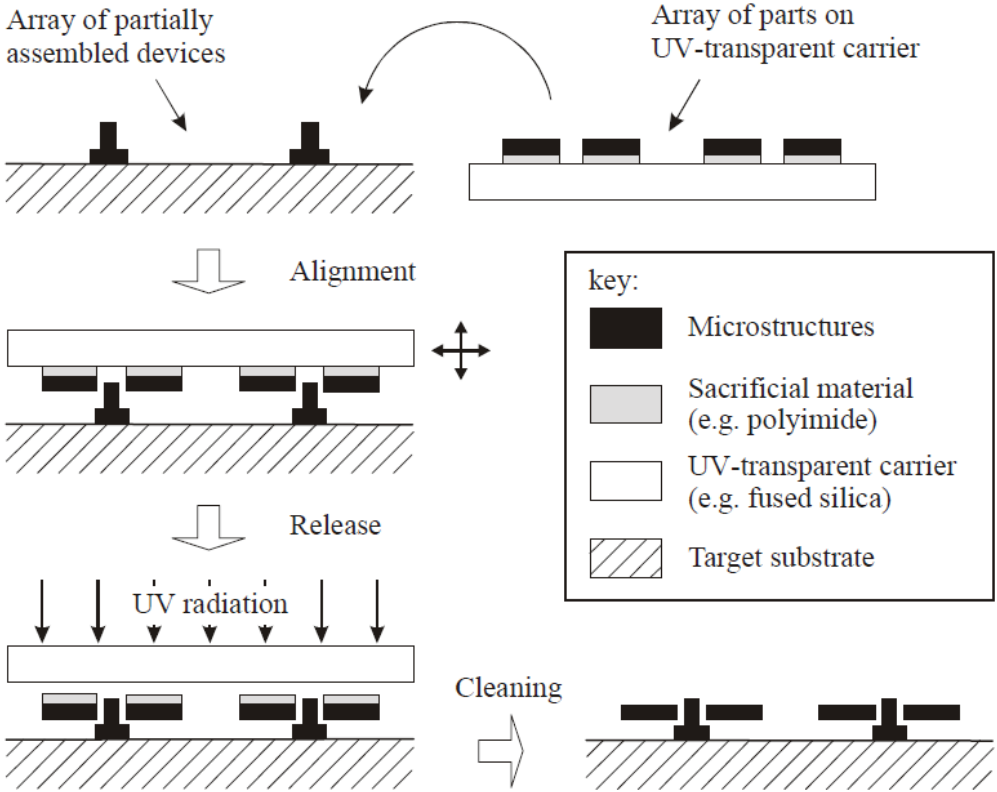
Figure 2.3. Laser MEMS micro-assembly using LIFT process [59].

Table 2.2. Summary of studies reported on the LIFT process.

LIFT Type	Donor Substrate	Transferred Material	Laser Beam	Application	Reference
Basic LIFT	Metal coated fused silica	Gold and copper	193 nm Excimer single pulsed with 12 nsec, 50 µm spot size, and 60-139 mJ pulse energy	Metal deposition	[52]
DRL-assisted LIFT (laser is induced through the receiving substrate)	Super Glue@ DRL layer attaching the LED to the transfer rod (non-transparent)	(In, Ga)N LEDs	Excimer laser	Micro-assembly Pd-In transient liquid phase bonding to make fluorescence detection micro-system	[68]
Multi-phase-assisted LIFT	Compound ink spin coated into a glass substrate	Li-ion battery electrodes: - Positive electrode: powder (LiCoO$_2$, carbon black, and polyvinylidene fluoride (PVDF)) is mixed in a balance of 1-methyl-2-pyrrolidone (NMP) - Negative electrode: powder (carbon super P and 7% PVDF) is mixed with NMP	Nd:YVO$_4$ laser with wavelength of 355 nm, 30 nsec pulse duration, 50 um spot size, and 25 µJ pulse energy	Printing micro-batteries electrodes	[69] [70]
DRL-assisted LIFT	Fused silica with polyimide DRL layer	100 µm thick nickel microstructures	-Excimer laser with wavelength of 248 nm is used -500 µm diameter aperture for step-and-repeat mode or release a group of 50 inks without the use of an aperture -Single laser pulse with 100 mJ/cm^2 energy density is used	Batch micro-assembly and bonding for MEMS	[59] [60]

Table 2.2. Summary of studies reported on the LIFT process (Cont.).

LIFT Type	Donor Substrate	Transferred Material	Laser Beam	Application	Reference
DRL-assisted LIFT and matrix-assisted LIFT	-Titanium coated glass -Polyimide coated glass (with and without ruptures in polyimide film)	-Aqueous solution of glycerol with Triton X-100 surfactant - 9-anthracenemethanol AM and Alq3 are added to (NMP)	Single pulse 355 nm wavelength laser, 20 nsec pulse duration, 2.5-10 μm spot size, and of 1-2.7 μJ pulse energy	Nozzleless inkjet printing of biological materials (i.e. light emitting organic molecules)	[71] [72]
Basic LIFT and matrix-assisted LIFT (MAPLE-DW)	Basic LIFT: fused silica coated with gold or nichrome MAPLE-DW: mixing powders with poly(butyl methacrylate in a chloroform solution	LIFT: silver, nichrome MAPLE-DW powders: BaTiO3 (BTO), SrTiO3 (STO),and Y3Fe5O12 (YIG)	Single pulse laser with 248 nm wavelength, 20 nsec pulse duration, and 8-200 μm spot size	Transfer of electronic and sensor materials	[73] [74]
Rheological systems	Protein-coated glass substrate	Protein-containing solution (human IgG in a solution of PBS with glycerol)	Laser beam with 355 nm wavelength and 10 nsec pulse duration	Transferring biomaterials for biosensors	[75]
Basic LIFT	Borosilicate glass coated with tine	Tine	Femtosecond laser with 800 nm wavelength, 130 fsec pulse duration, 10-15 μm laser spot size, and 0.4-1.2 J/cm^2 energy intensity	Metal deposition for fabrication of photonic devices	[76]
Basic LIFT	Glass coated with nichrome (as antireflection layer) and aluminum as material deposition source	Aluminum	-Q-switched Nd:YAG laser with a single pulse duration 120 nsec - Nd:glass laser system with 1.06 μm wavelength, and single pulse duration of 40 nsec	Metal deposition	[77]

Table 2.2. Summary of studies reported on the LIFT process (Cont.).

LIFT Type	Donor Substrate	Transferred Material	Laser Beam	Application	Reference
Basic LIFT	Titanium coated glass substrate	Titanium	He-Ne single pulses laser with 694 nm wavelength, and 20 nsec FWHM	Metal deposition	[78]
Basic LIFT	Tungsten coated glass substrate	Tungsten	Diode-pumped YAG continuous laser with 1064 nm wavelength, 9 μm spot size, 35-135 mW pulse power for durations of 0.1 or 1 sec	Metal deposition	[79]
Basic LIFT	Gold and Nickel coated quartz substrate	Gold and nickel	KrF laser with 248 nm wavelength, 30 nsec single pulse duration, and 0.2-4 J/cm^2 energy intensity	Metal deposition	[80]
Basic LIFT	Chromium or indium oxide coated quartz	Chromium or indium oxide	KrF laser with 248 nm wavelength, 13 mJ pulse energy, 500 fsec pulse duration, and 1-64 μm spot size	Metal and oxide films deposition	[81]
Basic LIFT	Quartz substrate where aluminum layer is sandwiched between two aluminum oxide layers	Aluminum oxide	- Nd:YAG lasers with 1064 nm with pulse duration of 70 nsec or 200 nsec - ArF laser with 193 nm wavelength	Oxide deposition	[82]
Basic LIFT	Vanadium oxide coated glass	Vanadium oxide	Q-switched Nd:YAG laser with 200 μm spot size, 1.4 J/pulse energy, and 10 nsec pulse duration with frequency of repetition of 10 Hz	Oxide deposition	[83]
Basic LIFT	Quartz wafers coated with zinc, then chemically treated to form zinc oxide	Zinc oxide	248 nm wavelength laser beam with 450 fsec pulse duration, and 170 mJ/cm^2 energy density	Oxide deposition	[84]

Table 2.2. Summary of studies reported on the LIFT process (Cont.).

LIFT Type	Donor Substrate	Transferred Material	Laser Beam	Application	Reference
Basic LIFT	Superconductors (YBaCuO and BiSrCaCuO) coated transparent substrate	High-temperature superconductors (YBaCuO and BiSrCaCuO)	- ArF Excimer laser with 193 nm wavelength, 20 nsec pulse duration, 0.1 and 0.5 J/cm^2 energy density per pulse - Pulsed (Nd:YAG) laser with 1064 nm wavelength, 5 nsec pulse duration, and 0.1 and 1 J/cm^2 energy density per pulse	Superconductors disposition	[85]
Multi-phase-assisted LIFT with DRL layer	Using Triazene Polymers (TP) as DRL layer, then coated with the liquid-phase solution	Liquid-phase solution made of distilled water and glycerol both plus the surfactant SDS, solution used to carry biomolecules (i.e. liposomes and DNA)	- XeCl Excimer laser with 308 nm wavelength, 25-30 nsec pulse duration, and 1 Hz repetition rate - Nd:YAG laser with 266 nm wavelength, 6 nsec pulse duration, and 2 Hz repetition rate	Biomolecules transfer	[86]
Rheological system with DRL layer	Itanium (DRL) coated glass substrate is used to hold the DNA solution	DNA molecules	Nd:YAG laser with 355 nm wavelength, 10 nsec pulse duration, and 10 µJ pulse energy	Biomolecules transfer	[87]
Basic LIFT	Composite coated quartz	Composite materials poly acrylicacid/Carbon Nano Tube (CNT) and polyvinylpyrrolidone/CNT	Nd:YAG laser with 266 nm wavelength, and 4 sec pulse duration	CNT based composite transfer	[88]
Multi-phase-assisted LIFT	Titanium coated quartz substrate	Ultra-dispersed diamond (UDD) powder mixed with water	Nd:YAG laser with 532 nm wavelength, 50 psec laser pulse duration, and 10 Hz repetition rate	Nanoparticles transfer	[89]
Basic LIFT	Silicon hyperbranched nanowires coated silicon substrate	Silicon hyperbranched nanowires	Q-switched Nd:YAG laser with 1064 nm wavelength, 100 µm spot size, 5-7 nsec. pulse duration, and 8.5-17 W power	Silicon nanowire transfer	[90]

Table 2.2. Summary of studies reported on the LIFT process (Cont.).

LIFT Type	Donor Substrate	Transferred Material	Laser Beam	Application	Reference
Basic LIFT	Aluminum or tine coated glass substrate	Aluminum and tine	Pulsed Ytterbium fiber laser with 532 nm wavelength, 1 nsec pulse duration, and 16 μJ pulse energy	Integrating solar cell electrodes	[91]
DRL-assisted LIFT	Dyes glued to the quartz wafer by a thin layer of dried FSC-L surface coating	InGaN bare dyes	A 248 nm wavelenght laser with 20 nsec pulse duration, and 8-200 μm spot size	InGaN bare dye LEDs	[92]

2.3 Micro-Transfer Printing

Micro-transfer printing uses a simple patterned stamp as a tool to pick up patterns selectively from a dense array of under-cut and ready-to-pick microstructures using Van der Waals forces between the ink and the stamp. Because micro-transfer printing technology uses an easy-to-make inexpensive elastomer stamp and has the capabilities to transfer thin films (< 10 μm thickness), the process has an advantage over the other parallel micro-assembly methods (flip-chip wafer-to-wafer transfer or array of micro-grippers mechanisms). In its basic embodiment, the mechanism of ink pickup and release is based on kinetically modulating the strain rate dependent adhesion strength at the ink-stamp interface (strong adhesion at high stamp retraction speed for pickup vs. weak adhesion at low speeds for release [1]). To enhance and extend the transfer printing technology capabilities and performance, several deterministic transfer variants of the process have been introduced (see Table 2.3) by modifying the stamp's geometry (patterned stamps [93], pedestal-shaped stamps [94], and microtipped stamps [2]) or by enhancing the transfer mechanism (shear-enhanced [95] and fluidic-chamber actuated [96]). Other process modes, besides the deterministic assembly, are introduced to subtract/add a thin film on the receiving substrate using an inked stamp from a spin-coated donor layer (see Fig. 2.4). The process has been used to heterogeneously integrate functional devices using a wide selection of materials [9] such as inorganic semiconductors, metals, carbons, organic materials, colloids, and biological materials.

Because the LMTP process leverages the non-contact laser nature, it is used to avoid the regular micro-assembly contact adhesion issues making the process independent from the receiving substrate properties and preparation [3] [4]. The previous work on the LMTP process focused on designing a prototype printer to demonstrate the LMTP process [3] and to show that the LMTP process is based on the ink-stamp interface delamination [4]. Further, Li, R., et al. used an

analytical axisymmetric thermo-mechanical model to estimate the Energy Release Rate (ERR) in the LMTP process based on the CTE mismatch strains [97]. Because the LMTP process has recently been introduced, this dissertation focuses on characterizing and modeling the LMTP process delamination to improve and optimize the process performance. On the other hand, post-processing steps are required to bond the printed inks to the receiving substrate. With the advantage of using the laser as a bonding tool, given the fact it is available on the printer, one can consider laser bonding to be the most suitable approach for the required post-processing steps in the LMTP process.

Table 2.3. Transfer printing technology variants.

Printing Type	Description	Reference
Patterned stamps	Patterns are fabricated on the stamp to reduce ink-stamp contact area and adhesion energy	[93]
Microtipped stamps	Preloading the ink-stamp interface using microtipped features on stamp to print on low adhesion surfaces	[2]
Pedestal-shaped stamps	Enhance the ink-stamp interface adhesion during ink pick up to increase the process yield	[94]
Shear-enhanced printing	Printing using shear loading to reduce energy required for delamination	[95]
Instrumented stamps	- Selective printing by actuating the stamps - Online force sensing for printing diagnostic and monitoring	[96]
Laser transfer printing	Laser beam is used to induce thermal strains at the ink-stamp interface to achieve non-contact printing	[3] [4]
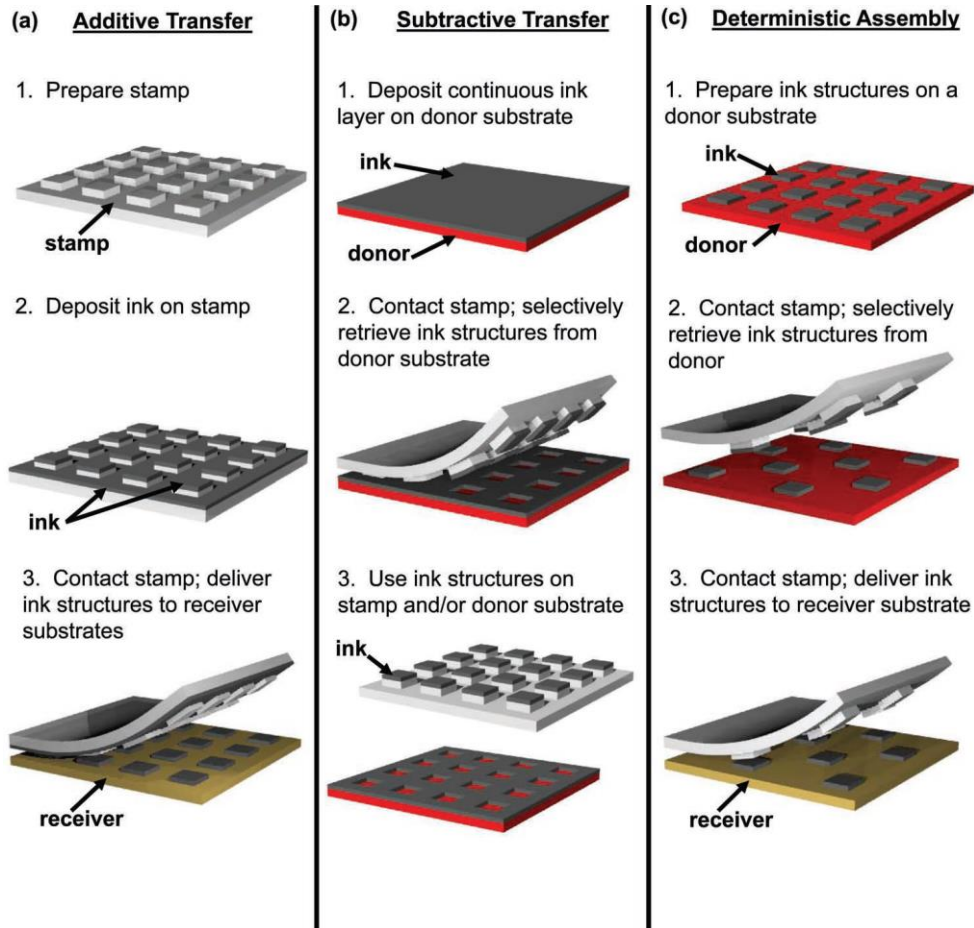
Figure 2.4. Schematic illustrations of the three basic modes of transfer printing [9].

2.4 Delamination Fracture Mechanics

As described in fracture mechanics theory, interfaces delaminate due to opening, shear, and/or tearing loads (also known as mode I, mode II, and mode III, respectively). Because the laser beam is always centered with the ink in the LMTP process, the generated strains at the ink-stamp interface are symmetric around any given center plane. This implies that only mode I and mode II loading can be generated at the ink-stamp interface. The intensity of the stress field in any fracture mode around the crack tip is usually quantified using the Stress Intensity Factor (SIF) corresponding to the fracture mode. The ERR is another measure for the rate of change of available strain energy at the crack tip as a function of the change of the crack length to drive the

26

delamination. Assuming linear elastic fracture, the ERR value G can be evaluated as a combination of the squares of the stress intensity factors in both fracture modes (opening mode SIF (K_I) and shear mode SIF (K_{II})) as shown in Eq. (2.1):

$$G = \frac{(1-\beta)}{\overset{*}{E}}(K_I^2 + K_{II}^2) \tag{2.1}$$

where $\overset{*}{E} = \frac{2\,\bar{E}_s\bar{E}_p}{(\bar{E}_s+\bar{E}_p)}$ is the effective interface Young's modulus and it is a function of Young's modulus of the ink and the stamp, and β is the second Dunder's parameter for Young's modulus mismatch interface. Therefore, the ERR components in the opening mode G_I and the shear mode G_{II} are given by Eq. 2.2 and 2.3, respectively:

$$G_I = \frac{(1-\beta)K_I^2}{\overset{*}{E}} \tag{2.2}$$

$$G_{II} = \frac{(1-\beta)K_{II}^2}{\overset{*}{E}} \tag{2.3}$$

Mode I   Mode II   Mode III
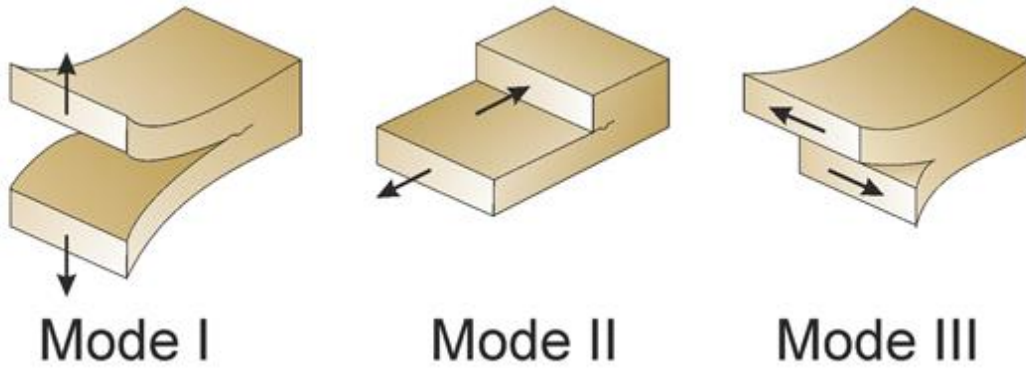
Figure 2.5. Fracture modes due to different loading types [98].

Because the Young's modulus of the Si ink is usually around five orders of magnitude higher than that of the PDMS stamp ($E_s >> E_p$) in the LMTP process, the equivalent interface Young's modules can be approximated as:

$$\overset{*}{E} \sim 2\, \bar{E}_p \tag{2.4}$$

Where for plane stress $\bar{E}_p = E_p$ and $\bar{E}_s = E_s$, and for plane strain $\bar{E}_p = \frac{E_p}{(1-v_p)}$ and $\bar{E}_s = \frac{E_s}{(1-v_s)}$.

The ERR value for quasi-static loading can also be evaluated directly using energy contour integral methods (i.e. J-Integral). Under the linear elastic fracture mechanics assumption, the J-integral value J for an arbitrary contour Γ around a crack tip (see Fig. 2.6) equals the ERR value G, as described in Eq. 2.5 [99]:

$$G = J = \int_\Gamma \left(U dy - \boldsymbol{T}.\frac{d\boldsymbol{u}}{dx}\, ds \right) \tag{2.5}$$

Where U is the strain energy density, $\boldsymbol{T}$ is the traction vector defined according to the outward normal k along the path Γ, $\boldsymbol{u}$ is the displacement vector, and ds is an element along the integral path Γ. Further, an "interaction integral" iterative algorithm can then be used to determine the SIFs from the ERR evaluated using the J-integral method [100]. For a given simple loading and geometry, the SIFs and ERR have analytical exact solutions for a crack initiated in homogenous materials. Suo, Z. found that the ERR and SIFs at the interface between two dissimilar materials follows the same nature and values compared to that of homogenous materials [101]. Therefore, the ERR and SIFs for homogenous material crack can be used to estimate the ERR at the ink-stamp interface in micro-transfer printing [102][103]. Once the estimated ERR reaches the work of adhesion of the interface, the available strain energy at the crack tip, measured by the critical ERR G_c, is enough to drive the delamination process based on Griffith's criterion. For two-dimensional

mixed-mode (mode I and mode II) problems, different fracture criteria [104] have been suggested to estimate the delamination point based on the work of the adhesions and the estimated ERRs in the different fracture modes. The linear power law is the most common criterion to estimate the point where the fracture occurs in mixed-mode problems (see Eq. 2.6).

$$\frac{G_I}{W_I} + \frac{G_{II}}{W_{II}} = 1 \tag{2.6}$$
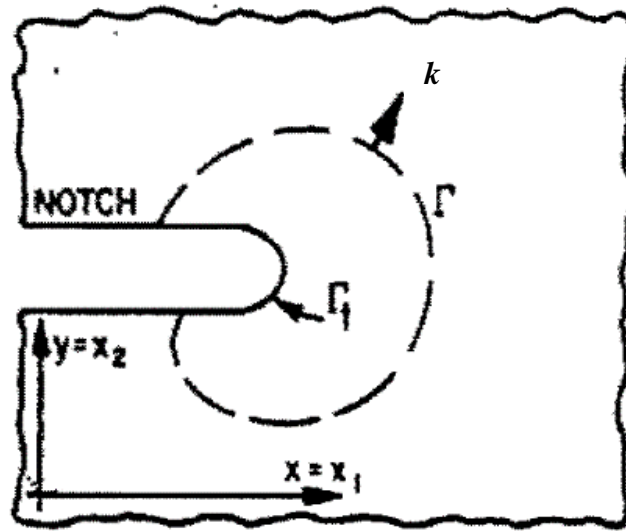
Figure 2.6. Evaluating the ERR value using the J-integral method in a two-dimensional problem [99].

The effects of thermal heating, due to heat conduction, in building up the SIFs or the ERR at the interface between two dissimilar materials have been investigated [105] [106-108]. These studies focus on understanding the geometrical effect of the singularity at the crack tip under uniform heating [106], the CTE mismatch between two materials at the interface [108], and the thermal gradients within the heated material stack [107]. Further, several studies have been conducted to investigate the effects of laser-driven thermal delamination between two dissimilar materials with the objectives of characterizing the dynamic thermal delamination at the interface [109], measuring the work of adhesion of opening and mixed-mode delamination problems [110],

and identifying the fatigue failure parameters [111]. Li, R. et al., developed an analytical thermo-mechanical model to estimate the laser-induced ERR based on the CTE mismatch strains in the LMTP process [97]. Using this approach, one then uses the ERR to estimate the mechanical load at the delamination point based on Griffith's criterion for a given work of adhesion of the ink-stamp interface.

Because the linear elastic fracture theory, described above, only estimates the energy required to start the crack propagation, the theory is not effective in understanding crack nucleation and the progressive nature of the crack propagation. On the other hand, the Cohesive Zone Modeling (CZM) approach [112] has the capabilities to model and simulate these phenomena. The major limitation of using the CZM approach is that a path for crack propagation has to be predefined, which is not an issue in interfacial delamination problems like micro-transfer printing. In CZM, a cohesive interface is defined at the interface and a traction-separation law (see Fig. 2.7 for mode I failure) is used to describe the non-linear nature of the interface strength. As demonstrated in the figure and by applying a load normal to the interface, the normal traction to the interface increases with the increase of the displacement up to the point where the maximum traction T_{max} is achieved. After this point, the traction at the interface decreases when the displacement increases. This softening behavior is described by the second traction-separation curve shapes; the bi-linear law is sufficiently accurate and widely accepted [113]. Because the traction-separation curve includes information about both the work of adhesion, the area under the curve, and the interface, i.e. the maximum traction to break the interface, the crack nucleation and propagation can be modeled to follow the interface traction-separation curve. Because the FEA method is more suitable for estimating the mechanical loads at the interface for complex shape multi-mode problems, discrete CZM is usually used where the traction-separation curve is imposed at each node on the interface.

The CZM approach has been used to model the thermo-mechanical delamination under thermal gradient in composite material [114], and CTE mismatch strains for MEMS packaging [115]. Further, the CZM approach is used to measure the work of adhesion of the interface during the laser-induced delamination for mixed-mode problems [111]. Therefore, in this work, both the linear fracture mechanics theory and the CZM approaches have been employed to understand the delamination at the ink-stamp interface for the laser-induced fracture.
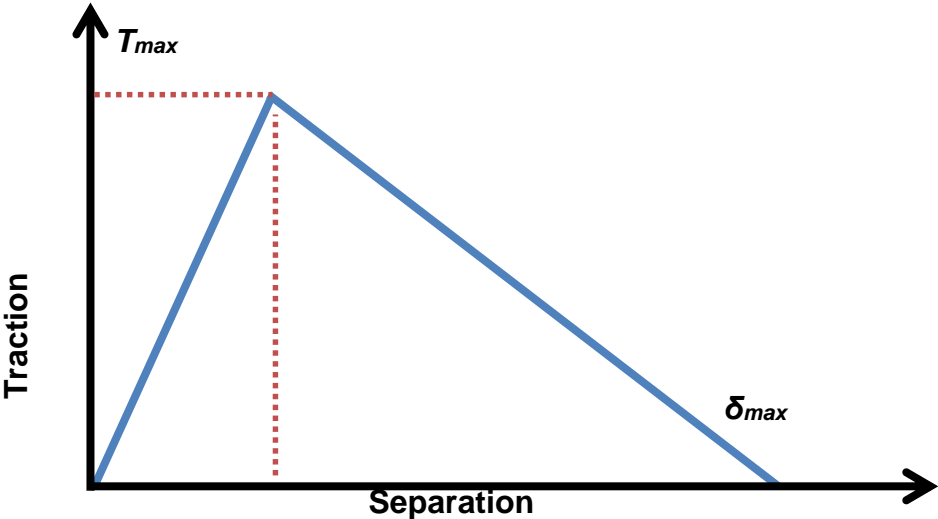
Figure 2.7. Bi-linear traction-separation curve for CZM.

2.5 Summary

Since the LMTP process avoids the need of contact between the ink and the substrate during printing, unlike regular transfer printing, it enhances the transfer printing technology to be independent of the receiving substrate's properties and preparation. Both the LMTP and the LIFT processes have similar process schemes and operational principles as non-contact pattern transfer processes. However, the LMTP release mechanism is based on interfacial delamination of the ink driven by laser-induced thermal strains. Therefore, the required energy and temperature to release the pattern are lower compared to the LIFT process. Further, the LMTP process does not require pre-processing steps to attach the pattern to the donor substrate or post-processing cleaning steps to remove the residue after the DRL ablation as in the LIFT processes. Therefore, the LMTP process, integrated with other transfer printing modes, makes for a more suitable and widely used pattern transfer technology. Because the LMTP is a recently introduced process, the focus of this dissertation is on characterizing, modeling, predicting, and improving the LMTP process.

CHAPTER 3: EXPERIMENTAL CHARACTERIZATION OF THE LMTP PROCESS[*]

3.1 Introduction

Because the LMTP is a recently introduced transfer printing technology, the focus of this chapter is on experimentally characterizing the process behavior by varying the key process parameters (ink's lateral dimension and thickness, and laser beam power). The laser beam pulse duration required to start the delamination, referred to as "delamination time," is measured using a high-speed camera. Because high temperatures could be damaging to active micro-devices, this study investigates the power absorbed by the ink and the energy input requirements, referred to as "delamination energy," as a function of ink dimension with a view to assess the temperatures reached by the inks during the process.

3.2 LMTP Printer Development and Calibration

A second-generation laser micro-transfer printer has been developed to automate the printing cycle, to improve the printing accuracy and repeatability, as well as to provide setup adjustment. As shown in Fig. 3.1, the new printer uses a high-precision, three-axis gantry system (ATS100-100; Aerotech, Inc.; USA) for positioning with an accuracy of ± 0.5 µm and a bidirectional repeatability of ± 0.3 µm over 100 mm travel range. Manual dual-axis tilt and rotary stages, mounted on the table, are used to adjust the angular alignment between the stamp and the donor and receiving substrates. Vacuum chucks, placed at the top of each rotary stage, are used to hold the substrates. A LabVIEW® (National Instruments Corporation; USA) program integrates the gantry's motion control drivers (Ndrive-CP; Aerotech, Inc.; USA) with the laser controller used

---

in the print head to automate the printing cycle. A LabVIEW user interface allows the operator to set process parameters and program multiple print cycles with automatic advancement of pickup and printing locations so that complete transfer print jobs can be automated.
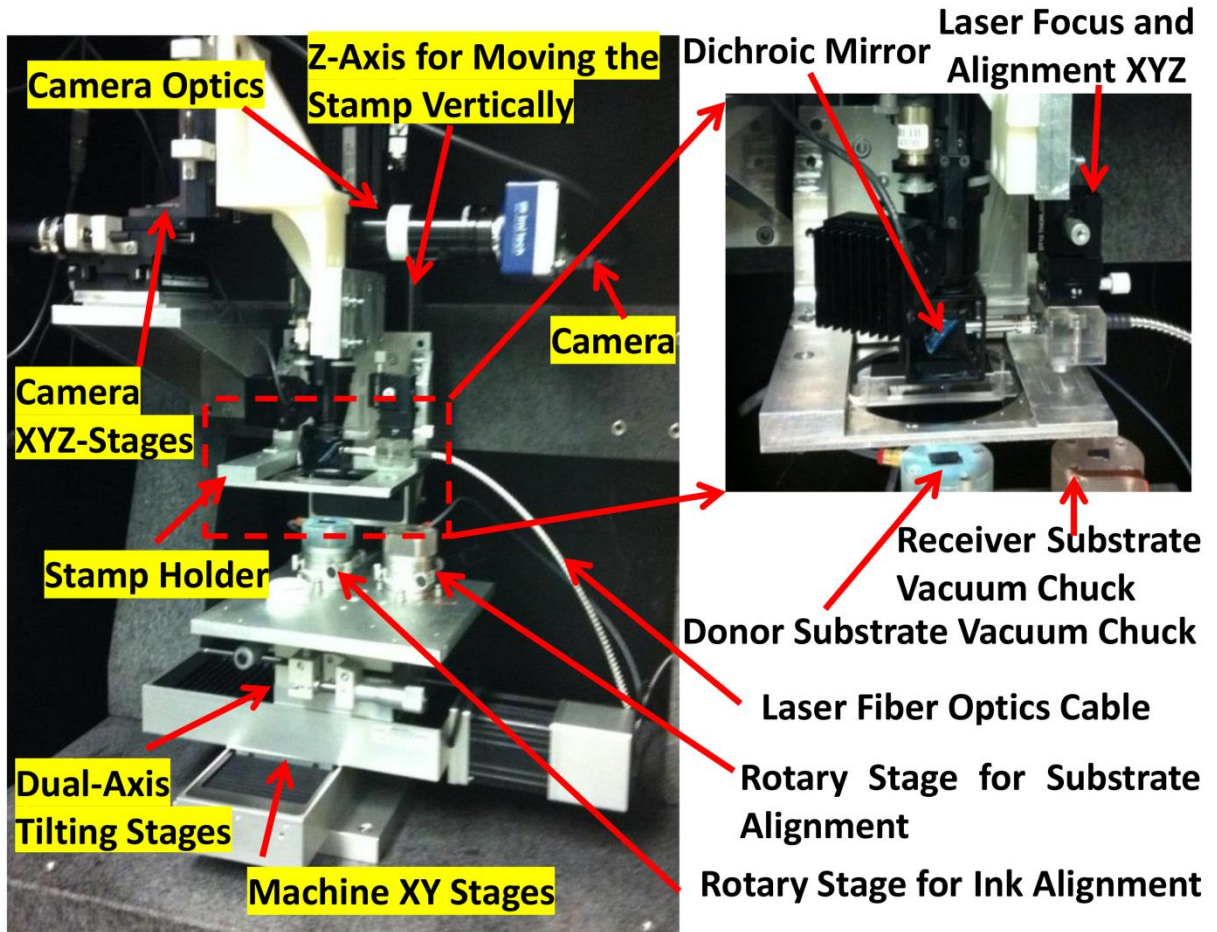
Figure 3.1. A second-generation laser micro-transfer printer.
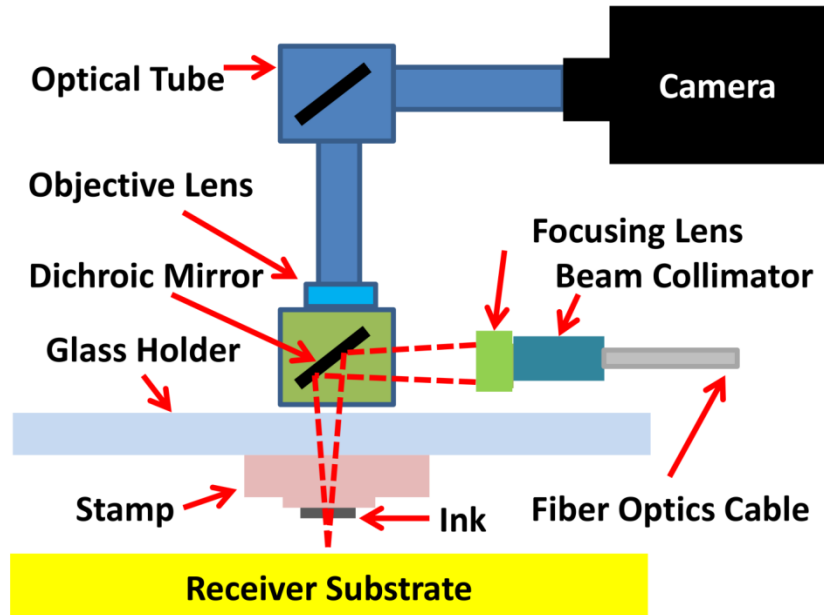
Figure 3.2. Schematic of the laser micro-transfer print head.

For set-up and monitoring purposes, a three-axis (XYZ) stage-controlled camera system with a long focal length allows for viewing the inks and substrates through the stamp. As shown in Fig. 3.2, the laser print head is attached to an optical tube of the camera with an optical cube that houses a dichroic mirror (transmission% > 85 for 425-675 nm wavelengths, reflection% > 90 for 750-1125 nm wavelengths). A 200 μm diameter (F-200 SMA-HP-3m; JENOPTIK Laser GmbH; Germany) optical fiber supplies the print head with laser radiation from a 805 nm wavelength 30 W, electronically pulsed, laser diode (JOLD-30-FC-12; JENOPTIK Laser GmbH; Germany). At the end of the fiber optics cable, a 4 mm diameter collimator and a focusing lens with a 51 mm focal distance is attached to focus the laser beam so that the beam, after being folded by the dichroic mirror, is focused to a spot diameter of 600-700 μm (Gaussian beam diameter definition) at the ink-stamp interface. Because the dichroic mirror is approximately 85% transparent to 425–675 nm wavelengths, this configuration allows the camera and the laser beam to simultaneously access the printing zone to permit recording by the CCD camera (pixel resolution of 1 μm). The stamp holder

is carried by the Z-stage of the gantry and thus its position relative to the laser beam and camera can be adjusted so that the beam can be accurately located with respect to the ink-stamp interface.

Measurements are performed to calibrate the power of the laser beam arriving at the print zone (after reflecting off the dichroic mirror) as a function of the laser diode current. These measurements are conducted using a 5.2 W maximum multi-wavelength power meter (PM100D; Thorlabs Inc.; USA) with a neutral density filter that has an optical density of 1.3 (5% transmission) to keep the measurements within the power meter's operational range. The results, shown in Fig. 3.3, indicate that the laser beam power still has a linear relationship with the laser diode current, but with a slope of 0.667 W/A compared to 0.9 W/A for the laser diode output. Such a drop in the laser beam power is due to losses in the optical components (such as the couplers, the cable, and the dichroic mirror) and interfaces.

To ensure consistent process behavior, it is also necessary to characterize the spatial distribution of the laser beam power. This is done by scanning a 100 μm diameter pinhole across the cross-section of the beam in steps of 20 μm in different axial planes. Figure 3.4 shows a schematic of this measurement, while Fig. 3.5 shows the beam profile for different axial planes, positioned relative to the focal plane. In this figure f_0 is the focal plane imaging the fiber cable end while f_6 (for example) is a plane 6 mm away from f_0 plane, moving toward the lens while f_{-8} is a plane 8 mm from the f_0 plane, moving away from the lens. With the exceptions of the f_6 and f_{-8}, the beam profile has a mesa shaped profile, i.e., flat-top with Gaussian-like side walls. For these LMTP experiments, the f_0 plane was used because it provides uniform laser intensity for any ink with a lateral dimension less than about 400 μm.
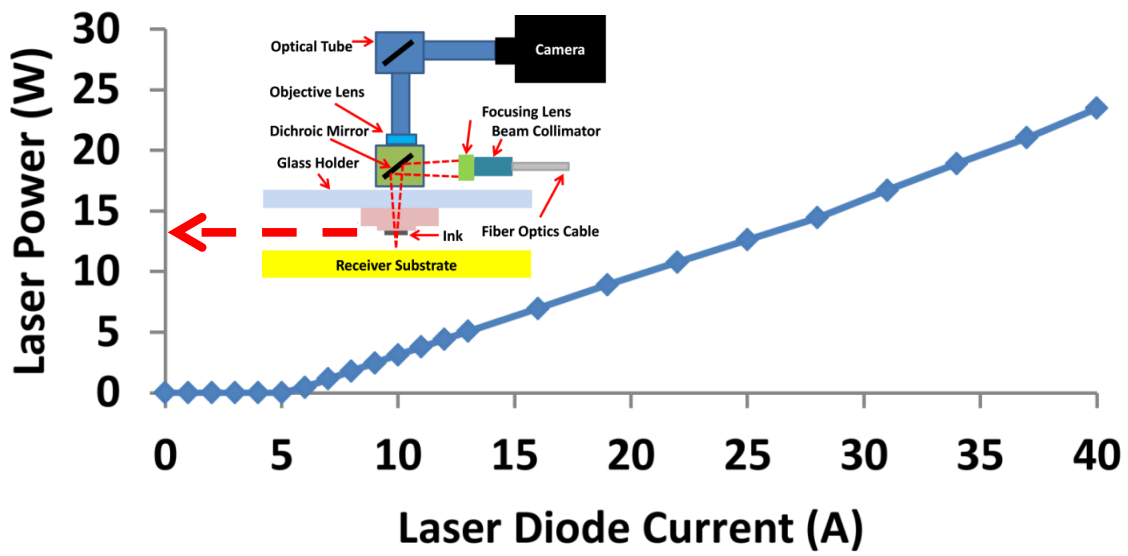
Figure 3.3. Measured laser beam power at the print zone as a function of the laser diode current.
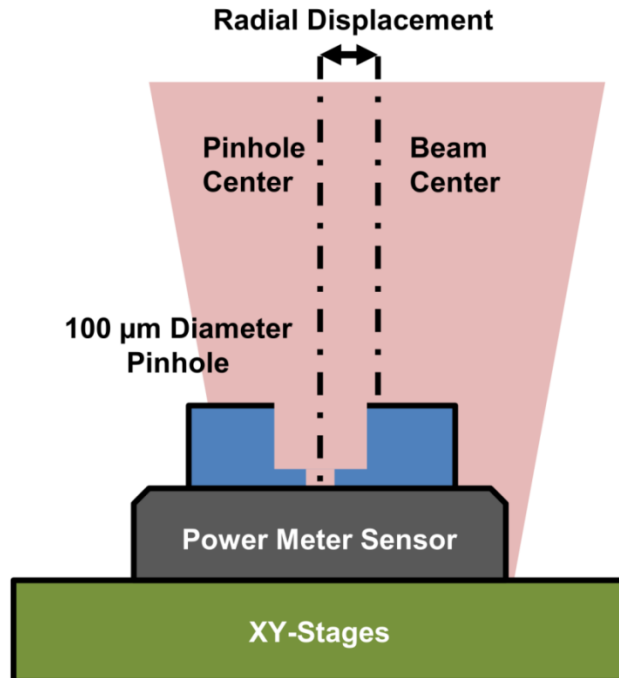
Figure 3.4. Schematic of experimental setup used to characterize the laser beam in the print zone.
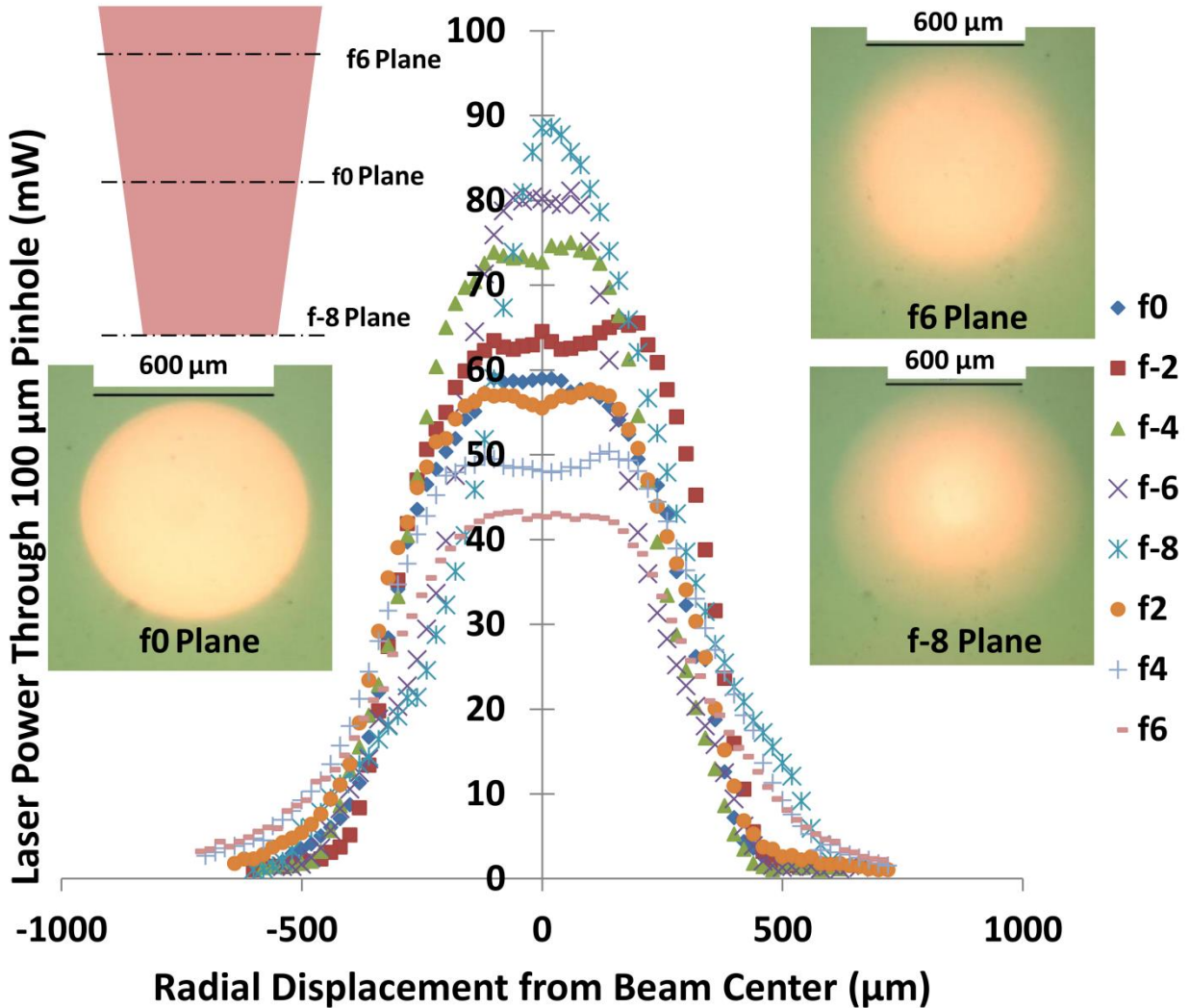
Figure 3.5. Laser beam profile at different imaging planes (images were captured using a 4 A laser beam current level reflected from a gold substrate).

3.3 Process Parameters and Design of Experiments

A number of factors can influence the behavior of LMTP as indicated in the fishbone diagram of Fig. 3.6. The figure shows that the process parameters can be classified into those related to ink, stamp, receiving substrate, laser beam, and printing process. These parameters directly affect process performance measures such as print quality (accuracy, repeatability, and surface quality), productivity (printing cycle time), and process performance measures (delamination time,

delamination temperatures, and delamination energy). While using silicon micro squares as model ink, this chapter studies the effects of ink dimensions and the laser beam power on the major process performance measures such as delamination time, and the energy required for delamination. Nine square silicon ink sets are fabricated to demonstrate the laser micro-transfer printing processes of devices with three different thicknesses (thin inks with 3 μm thickness, medium thickness inks with 10 μm thickness, and large thickness inks with 50 μm thickness) and with three different sizes (small-size square silicon inks with 100 μm sides, medium-size square silicon inks with 150 μm sides, and large-size square silicon inks with 200 μm sides). These silicon ink sets are used to study and characterize the delamination of the LMTP process at three different power levels (low-power level of 3.126 W at 10 A current, medium-power level of 6.301 W at 15 A current, and high-power level of 9.524 W at 20 A current) indicated by the laser diode current-power output graph of Fig. 3.3.
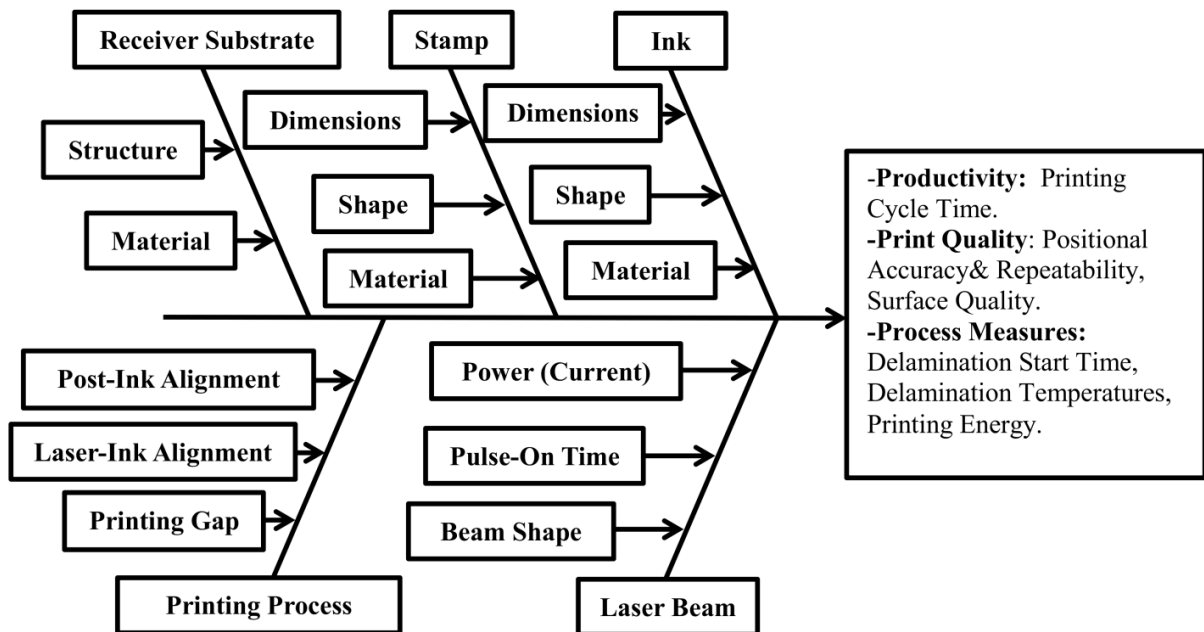
Figure 3.6. Fishbone diagram of factors affecting the LMTP process.

39

3.4 Delamination Time

The delamination time is a key process parameter in characterizing the energy requirements for delamination. Longer delamination times lead to low printing rates and, more importantly, potential damage to the stamp and the ink. As it will described later in Section 3.5, the sizes and thickness of the different square silicon inks affect the laser heating rates differently. To experimentally measure the delamination time, a high-speed camera (Phantom v7.3; Vision Research, Inc.; USA) is used in place of the standard camera in the printing setup. The modified printer schematic, shown in Fig. 3.7, has a NIR filter placed between the high-speed camera and the optical tube to protect the camera sensor from the high intensity laser pulse. Additionally, the laser diode's pulsing (start and pulse width) is externally controlled by a signal generator and synchronized with the high-speed camera through a 50 μs response time relay (PLA160; Clare, Inc.; USA). Using this setup, 4000 frame/sec. videos of the delamination process of LMTP are recorded.
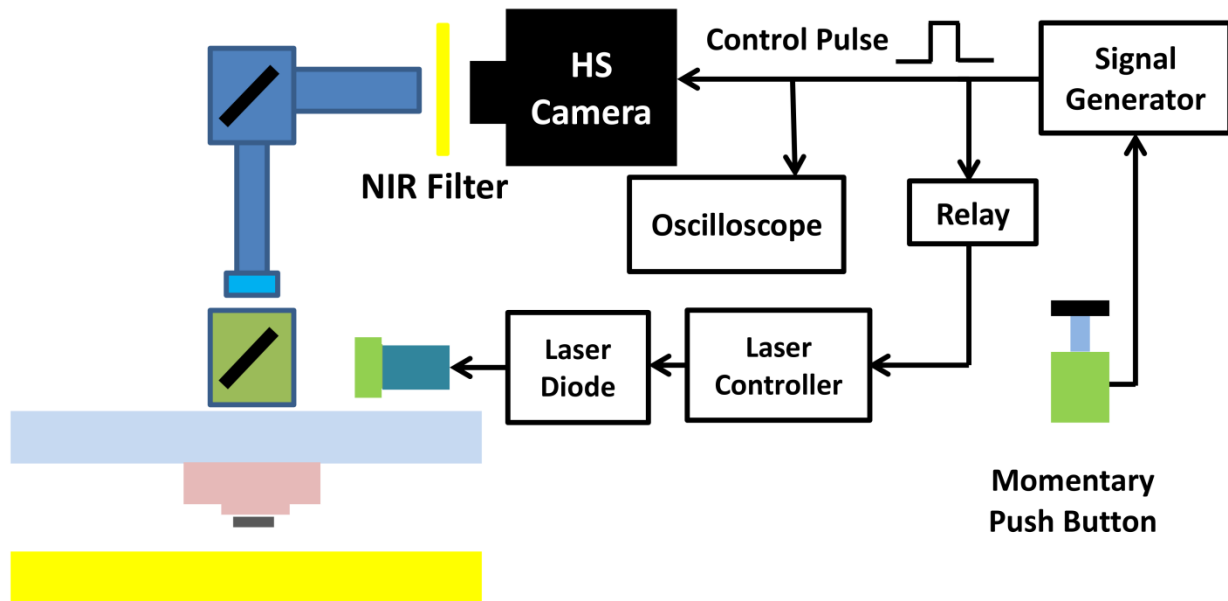
Figure 3.7. Schematic of hardware configuration for measuring of delamination time.

A factorial design experiment was used to collect the videos at three different thicknesses (3 µm, 10 µm, and 50 µm thicknesses), three different sizes (100 µm, 150 µm, and 200 µm inks sizes), and three different laser beam current levels (10, 15, and 20 A current levels). Each experiment was repeated three times. For all experiments, the ratio of the size of the square post on the PDMS stamp to that of the square silicon ink was kept constant (at a value of $R = 2$), while the post height was kept constant $h_p = 50$ µm with a backing layer of about 1 mm. The experiments were conducted at an f_0 focus laser beam profile with the laser beam center aligned with that of the inks. The standoff distance, i.e. the gap between the bottom surface of the ink and the receiving substrate, was kept at 500 µm to ensure minimal interaction between the flat silicon receiving substrate and the ink-stamp system. The signal generator was set up to provide a single 20 msec. laser pulse, even though the required delamination time for most of experiments is less than 20 msec. Figure 3.8 shows an illustration of how the delamination time was observed for printing 150×150×3 µm square silicon ink at 10 A current level. The micrographs show how the delamination time was observed at the beginning of frame 19 (4.75 msec.), while the delamination process was completed within one time frame (less than 250 µsec.). At the end of the laser printing process, the images show that the regions of PDMS in contact with the ink experience larger deformations compared to the rest of the PDMS post.

A statistical analysis is performed on the delamination time to identify the significant LMTP delamination process parameters (current levels, ink size, and ink thickness) along with the replication number (Trial No.) as shown in the ANOVA table in Fig. 3.9-a. The analysis shows that the process parameters (current levels, ink size levels, and the ink thickness levels) are all statistically significant based on 99% confidence (P-value is less than 0.01). The number of replications is statistically insignificant (P-value is higher than 0.01), indicating that delamination

41
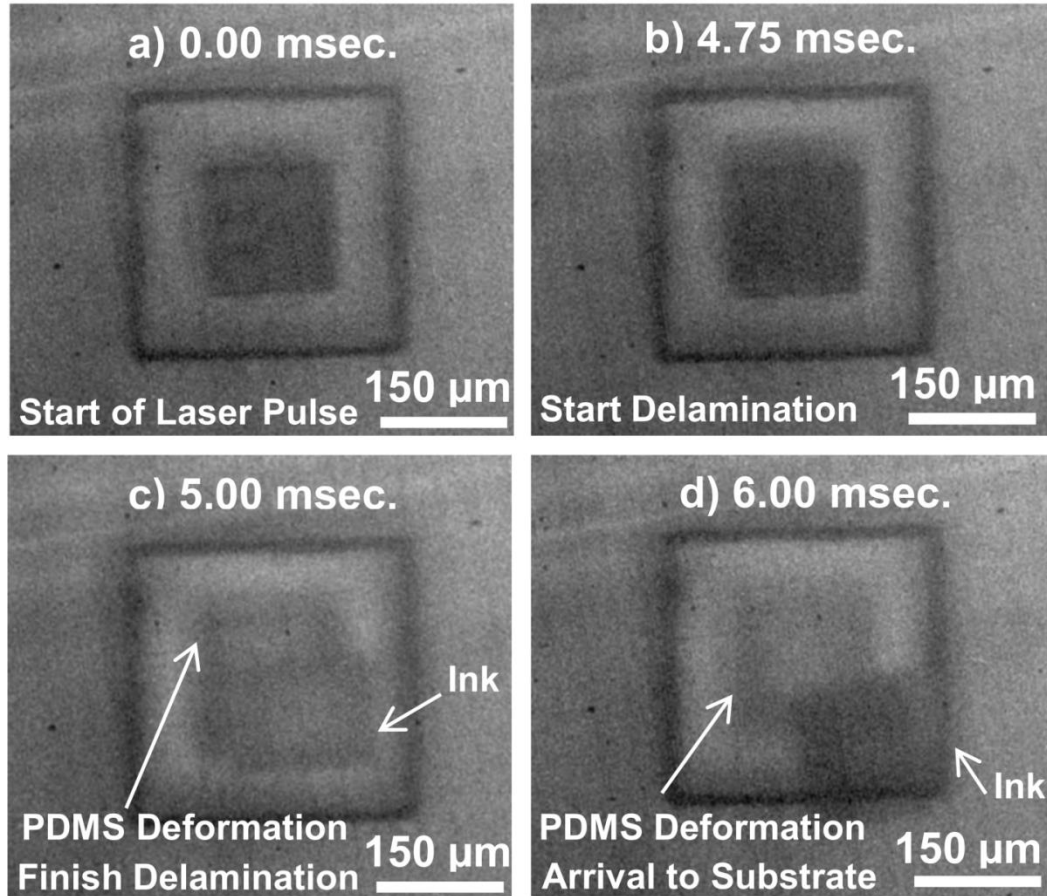
Figure 3.8. Example of frames from a high-speed camera recording of the delamination process used to measure delamination time (here 4.75 msec); images are post-processed to improve contrast.

time experiments are highly repeatable, with 85.86% of the total variation in the delamination time accounted for by variations in the selected process parameters. Including the interaction between the process parameters as factors, one observes (see Fig. 3.9-b) that all the two-level interactions (current level interaction with ink thickness, current level interaction with ink size, and ink size interaction with ink thickness) are statistically significant (P-value is less than 0.01). Therefore, the experimental trends for the delamination time based on any factor generally require the specification of the levels of other factors, resulting in an accounting of 98.58% of the delamination time variations observed in the experiments. Figures 3.10-a, 3.10-b, and 3.10-c show the

delamination time response at 20, 15, and 10 A current levels for different ink sizes and thicknesses, respectively. The error bars around the delamination time average show that, in general, printing of thin inks (3 and 10 µm ink thickness) produces the highest relative repeatability, while lower repeatability is reported in printing 50 µm ink thickness. Moreover, there is no difference in the repeatability for the 10 A and the 15 A current levels at the 3 µm and the 10 µm ink thickness for all ink sizes.

a-
Analysis of Variance for Del. Time, using Adjusted SS for Tests

Source	DF	Seq SS	Adj SS	Adj MS	F	P
Size (um)	2	70.72	70.72	35.36	8.59	0.000
Thickness (um)	2	1241.56	1241.56	620.78	150.73	0.000
Current (A)	2	488.28	488.28	244.14	59.28	0.000
Trial No.	2	0.03	0.03	0.02	0.00	0.996
Error	72	296.53	296.53	4.12		
Total	80	2097.13				

S = 2.02939   R-Sq = 85.86%   R-Sq(adj) = 84.29%

b-
Analysis of Variance for Del. Time, using Adjusted SS for Tests

Source	DF	Seq SS	Adj SS	Adj MS	F	P
Size (um)	2	70.72	70.72	35.36	73.81	0.000
Thickness (um)	2	1241.56	1241.56	620.78	1295.74	0.000
Current (A)	2	488.28	488.28	244.14	509.59	0.000
Size (um)*Thickness (um)	4	51.20	51.20	12.80	26.72	0.000
Size (um)*Current (A)	4	12.30	12.30	3.08	6.42	0.000
Thickness (um)*Current (A)	4	203.35	203.35	50.84	106.11	0.000
Error	62	29.70	29.70	0.48		
Total	80	2097.13				

S = 0.692165   R-Sq = 98.58%   R-Sq(adj) = 98.17%

Figure 3.9. Statistical analysis of process parameters affecting delamination time, (a) ANOVA table for main effect of process parameters and trial number, and (b) ANOVA table for main effect and two way interactions of process parameters.

In general, higher laser diode currents lead to shorter delamination times for all ink sets. This is because increased laser beam intensity leads to higher heating rates. Also, increases in ink

thickness lead to higher delamination times for all sizes and thicknesses. The thermal capacity of the ink increases faster than the increased absorption, leading to slower temperature rise. If the temperature for delamination depends only on the ink and stamp materials, then reaching the same temperature for thicker inks requires longer time intervals (see Fig. 3.10-a, 3.10-b, and 3.10-c.), also contributing to increases in the total heat loss to the PDMS post. For 10 A current level, the delamination time for 50 μm ink thicknesses is much greater than for 3 μm and the 10 μm ink thicknesses. This difference decreases for 15 and 20 A current levels. The delamination times for 3 μm and the 10 μm ink thicknesses at 10 A current levels is essentially the same, though, differences emerge for the 15 A current level and clearly increase for the 20 A laser beam current level.

For all laser current levels, the delamination times for the 3 μm and the 10 μm ink thicknesses increase with an increase of the ink size. However, for the 50 μm thickness, the delamination time depends on ink size level. For example, the delamination time for 50 μm thick ink increases significantly when ink sizes increase from 100 μm to 150 μm at all current levels. However, for an increase in the ink size from 150 μm to 200 μm, the results show a very small increase at the 15 A laser beam current level while decreasing for both the 10 A and 20 A laser beam current levels. Further, the experiments show that for all ink thicknesses, the delamination process is stable, where the crack propagation progress can be terminated and reversed [4] by having the laser pulse duration slightly less than or equal to the delamination time. Such behavior occurs because the available strain energy at the edge of the ink is sufficient to initially drive the delamination crack. However, a continuous supply of thermal energy by the laser beam is required to maintain the ERR at the interface at the work of adhesion to drive the delamination to completion.
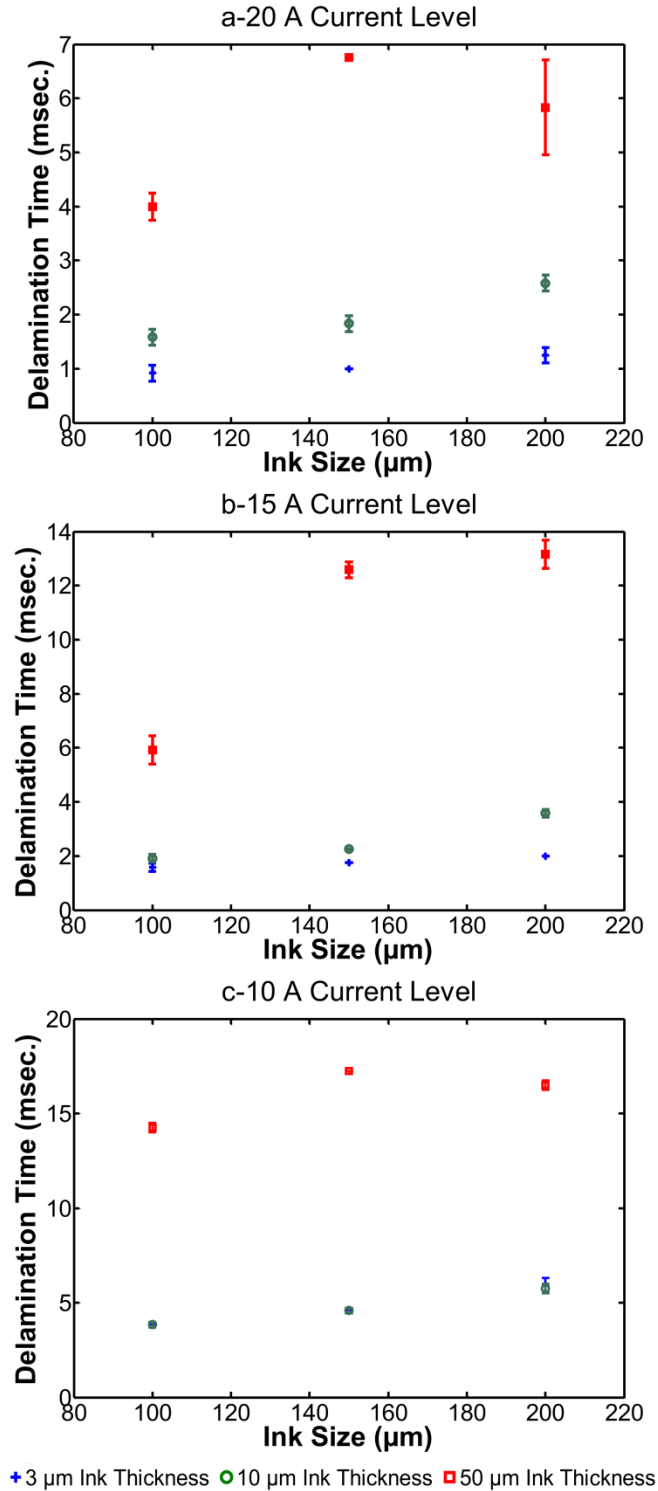
Figure 3.10. Delamination time experimentally observed using the high-speed camera, (a) 20 A laser beam current level, (b) 15 A laser beam current level, and (c) 10 A laser beam current level (the delamination times for 3 and 10 μm thick inks at 10 A current overlap).

45

3.5 Ink Power Absorption

To determine the amount of laser power absorbed by the silicon ink, a series of experiments are conducted to relate the laser beam power absorbed by the silicon ink with the different ink thicknesses and sizes. To do so, the laser diode source was set to operate at 10 A (roughly around 3.126 W at the print zone as per calibration of Fig. 3.3) with pulse widths of 9.725 msec. The beam power was measured by the power meter (Fig. 3.11), and its measurements are acquired using a 14-bit data acquisition system (NI USB-6009; National Instruments Corporation; USA) at a sampling frequency of 40 KHz. These measurements are performed with and without each size and thickness of the silicon inks. To protect the power meter from delaminated silicon inks, a 100 µm thick glass cover slip was used between the stamp and the power meter. The net loss in power due to this glass cover was measured to be 7.06%. Figure 3.11 shows schematics of the measurement setup with and without ink while Fig. 3.12 shows an example of how the laser beam power arriving at the power meter drops when a 200×200×50 µm silicon chip is attached to the stamp relative to the same stamp that does not have the ink attached.
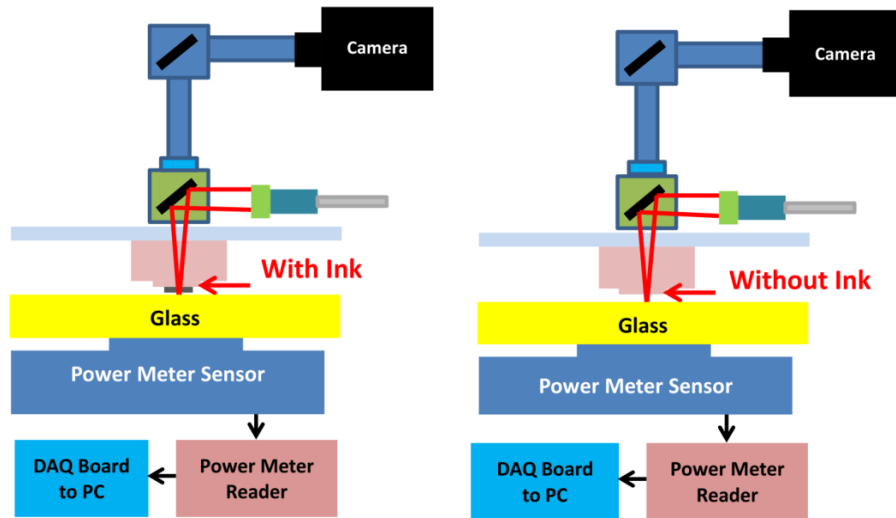
Figure 3.11. Experimental setup for measuring the laser beam power absorbed by the silicon ink.

To verify these measurements, the power absorbed by ink for each size and thickness is predicted using an optical absorption model (more details are shown in Section 4.3) by assuming the number of internal reflections of $n = 50$, absorption coefficient of silicon at 805 nm $\alpha = 10^5$ m^{-1}, and uniform beam intensity (on the ink at 10 A current) $I_a = 6.4986 \times 10^6$ W/m^2 (estimated from the beam profile at f_0 focus plane at 10 A laser diode current level). The experimental power absorption values are calculated for each given ink set and compared with the optical absorption model prediction in Fig. 3.13-a. The results indicate the amount of laser power absorbed by the silicon ink is higher for larger ink sizes and thicker inks. The measured power absorbed by ink follows the trends and values predicted by the model. Normalizing the amount of laser power absorbed by the ink's thickness, as shown in Fig. 3.13-b, results in a clear parabolic relationship between the amount of laser power absorbed and the ink size. The amount of power absorbed for a given ink size per unit thickness is higher for the 3 μm thick inks, followed by the 10 μm inks, and is the lowest for the 50 μm inks. Conversely, normalizing the amount of energy absorbed by the ink area, as shown in Fig. 3.13-c, indicates that thicker ink sets have higher power absorption per unit area compared to thinner inks. A combination of both trends is shown in Fig. 3.13-d where the amount of power absorbed is normalized by the ink volume to show that thinner inks have higher power absorption density compared to thicker inks. The model shows that 99.44%, 67.34%, and 29.35% of the power entering a square ink is absorbed by the 50, 10, and 3 μm thick inks, respectively. However, the heating of inks depends on the heat capacity that, for the same materials, depends on the total ink volume. For a given ink size, the relative volume for 50 μm and 10 μm thick ink sets compared to 3 μm thick ink is 16.667 and 3.333, respectively. For the same size, the thinner inks have a higher power absorption density than thicker inks, even though the total power absorbed by thicker inks is higher.
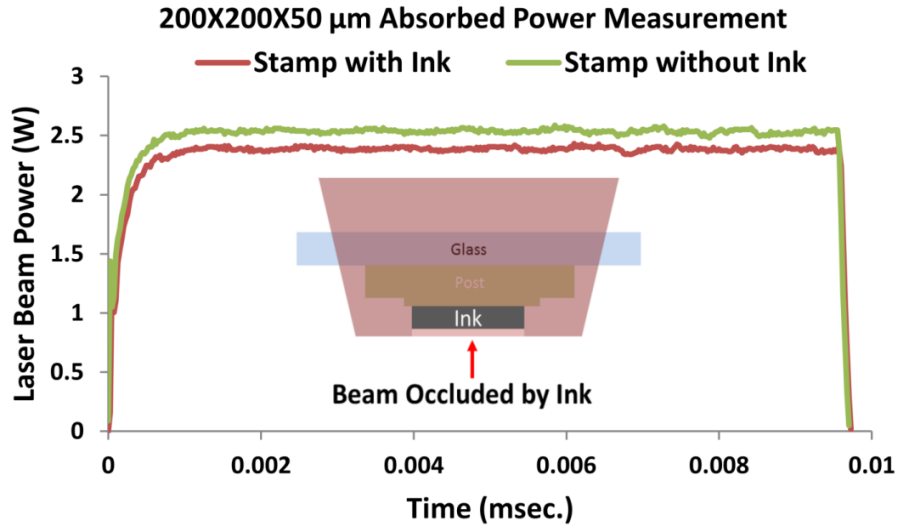
Figure 3.12. Example signals recorded by the power meter.
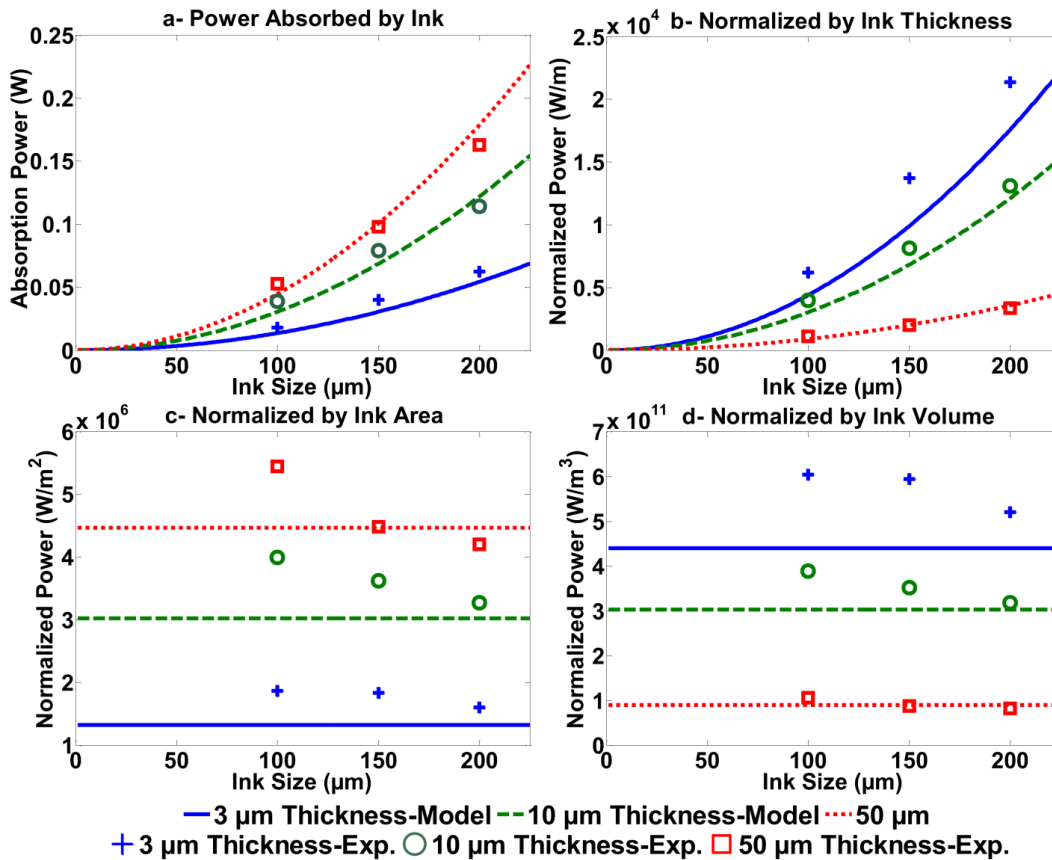
Figure 3.13. Power absorbed by silicon inks, (a) power absorbed by silicon ink, (b) normalized power absorbed by silicon thickness, (c) normalized power absorbed by ink area, and (d) normalized power absorbed by ink volume.

3.6 Delamination Energy

The total amount of laser beam power absorbed over the delamination time period is the energy required for delamination $E_d=P_bt_d$. As shown in 3.14-a, the energy requirements increase with size and thickness of the ink. Normalizations of the amount of delamination energy against ink thickness, area, and volume are shown in Fig. 3.14-b, 3.14-c, and 3.14-d, respectively. The results show that the delamination energy normalized for ink thickness is higher for thinner inks and for larger ink sizes. This result follows from the fact the normalized power absorbed per unit thickness is higher for thinner inks and increases with the size of the ink. The delamination energy normalized by the ink area is almost constant for a given ink thickness and higher for thicker inks. This is consistent with the idea that the local conditions, such as temperature and induced strain, of the ink-stamp interface are what drive the delamination process. Finally, the amount of delamination energy per unit volume is higher for thinner inks, and it slightly decreases based on the ink size for 50 μm ink thicknesses and increases for 3 μm and 10 μm inks thicknesses. This again is consistent because of the power absorption profile with depth (as in Fig. 3.13).

3.7 Summary

In this chapter, a second generation LMTP printer was developed and calibrated to automate the printing cycle and improve the process accuracy and repeatability. A series of experiments were conducted to measure the delamination time for different square ink sizes and thicknesses at different laser beam power levels. The results show a high delamination process repeatability with the general tendency for an increase of delamination time, with an increase in ink size or thickness, and a decrease in laser beam diode current. The results from both the delamination time with the amount of laser beam power absorbed by the square silicon ink are used to determine the amount of energy required to start the LMTP delamination process.
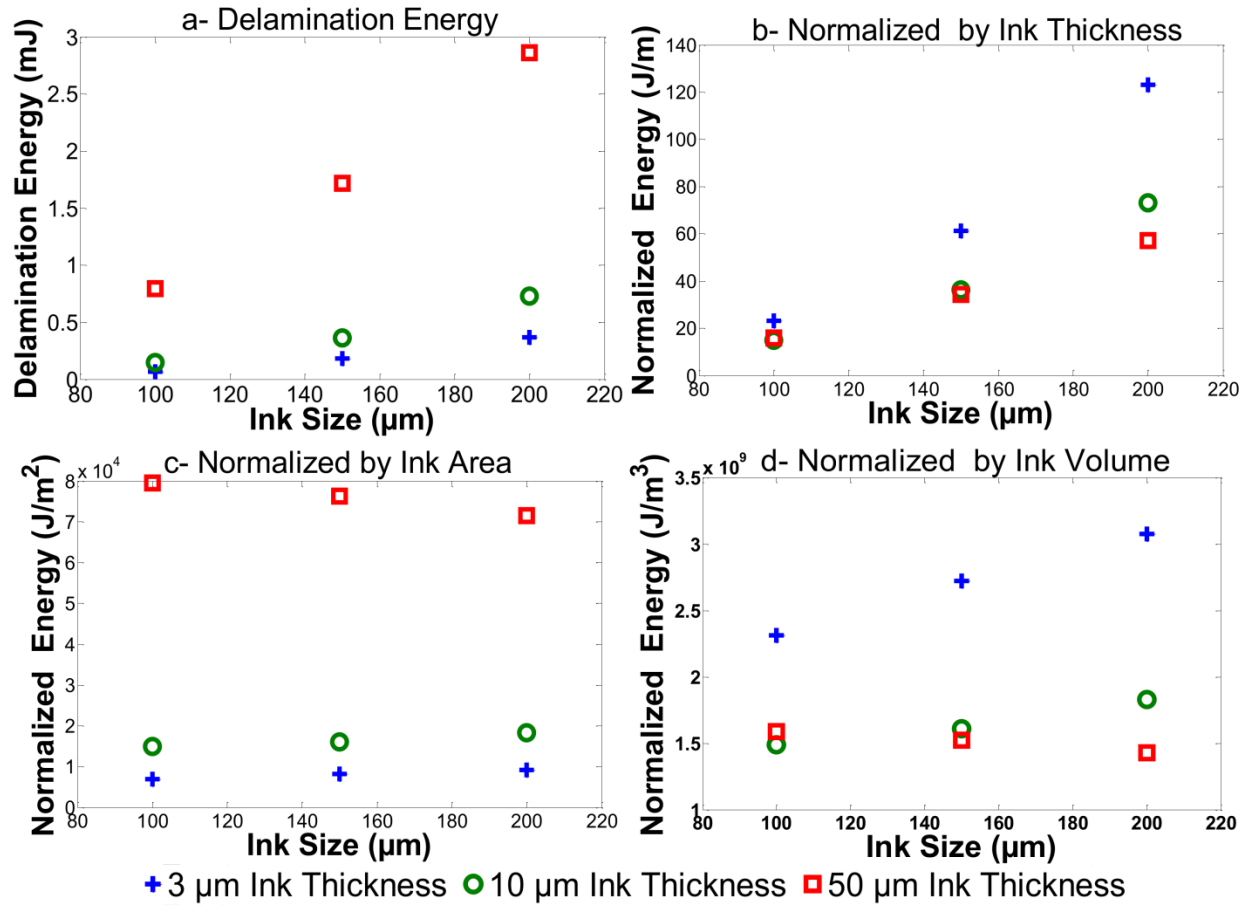
Figure 3.14. Energy required to initiate delamination, (a) energy input required to start delamination, (b) energy input required to start delamination normalized by ink thickness, (c) energy input required to start delamination normalized by ink area, and (d) energy input required to start delamination normalized by the ink volume.

CHAPTER 4: LMTP PROCESS MODELING AND MECHANISM[†]

4.1 Introduction

In this chapter, an opto-thermo-mechanical model is developed to understand how the laser beam energy, absorbed by the ink, is converted to thermally-induced mismatch strains around the ink-stamp interface to drive the ink delamination process. The opto-thermo-mechanical model is developed based on decoupling the optical absorption physics from the thermo-mechanical model physics. An optical absorption model for the laser beam energy absorbed by the ink is first developed and verified experimentally to estimate the heating rates of the ink-stamp system which, in turn, is used as an input for a coupled thermo-mechanical FEA model. Further, high-speed camera recordings for the LMTP delamination are used to calibrate the thermo-mechanical model and verify its predictions. Besides providing a fundamental understanding of the delamination mechanism and the LMTP process capabilities, the developed opto-thermo-mechanical model is useful in selecting process parameters (laser pulse duration, stand-off distance), estimating the rise in ink-stamp temperature during the LMTP process, and quantifying and decomposing the stresses at the ink-stamp interface to its main sources (CTE mismatch and thermal gradient strains).

4.2 LMTP Delamination Modeling Approach

Because the ink pickup and transfer steps in the LMTP process are similar to those in micro-transfer printing, the LMTP process is different in terms of the release mechanism that is based on generating laser-induced thermo-mechanical strains at the ink-stamp interface. The laser beam power absorbed by the ink heats up the ink, which in turn, transfers heat to the PDMS stamp,

raising the ink-stamp interface temperature. Due to the low thermal conductivity of the PDMS, a localized hot zone is developed in the PDMS in the vicinity of the ink-stamp interface. The PDMS in this zone expands because of its large CTE (310 ppm/^{o}C). Constrained by the silicon ink (CTE 2.6 ppm/^{o}C) and the surrounding unheated PDMS, this expansion is accommodated by the development of a curvature or bulge at the contact interface due to CTE mismatch and thermal gradient strains, respectively. The curvature gives rise to a bending moment that stresses the ink-stamp interface normal to the interface direction (opening mode) and along the interface (shear mode). Further, the sharp thermal gradient at the ink-stamp interface's edges loads the ink-stamp interface in both fracture directions (opening and shear modes). Once the stored strain energy, measured by the ERR, at the interface reaches the work of adhesion of the ink-stamp interface, the delamination crack, at the perimeter of the ink, propagates inward to release the ink from the PDMS stamp.

Understanding the mechanism of delamination during the LMTP process requires integrating the effects of multiple physical phenomena involved in the process. Therefore, the modeling approach (see Fig. 4.1) is based on first developing an optical absorption model under the assumption that absorption during the LMTP process is decoupled from the thermo-mechanical physics. The optical absorption model is used to estimate the heating rate of the ink during the LMTP process, which in turn, is used as an input to the coupled thermo-mechanical model. A transient coupled FEA thermo-mechanical model is then developed to estimate the stresses, strains, temperature gradient, and temperature fields during the LMTP process using ABAQUS® (ABAQUS Inc.). To extend this to the onset of delamination in order to understand, control, and predict the delamination process behavior, the fracture mechanics quantities such as the ERR and the SIFs are essential. Therefore, a small crack is introduced at the model ink-stamp interface edge

to collect the ERR and the SIFs during the LMTP process. The goal of such a model is to understand how different thermal strain components (CTE mismatch and thermal gradient within the stamp) affect the printing process at different laser beam powers (10, 15, and 20 A which are equivalent to laser beam power of 3.268, 6.587, and 9.956 W, respectively) and different critical dimensions (in this chapter; 3, 10, 30, and 50 µm thickness) of the ink. Such predictions should help in planning the laser pulse duration required to print different inks, planning the stand-off distance to avoid crack closure due to ink-receiving substrate collision, estimating the temperatures reached by the ink during the printing process, quantifying and decomposing the thermally-induced strains at the ink-stamp interface, as well as understanding the process capabilities and limitations.
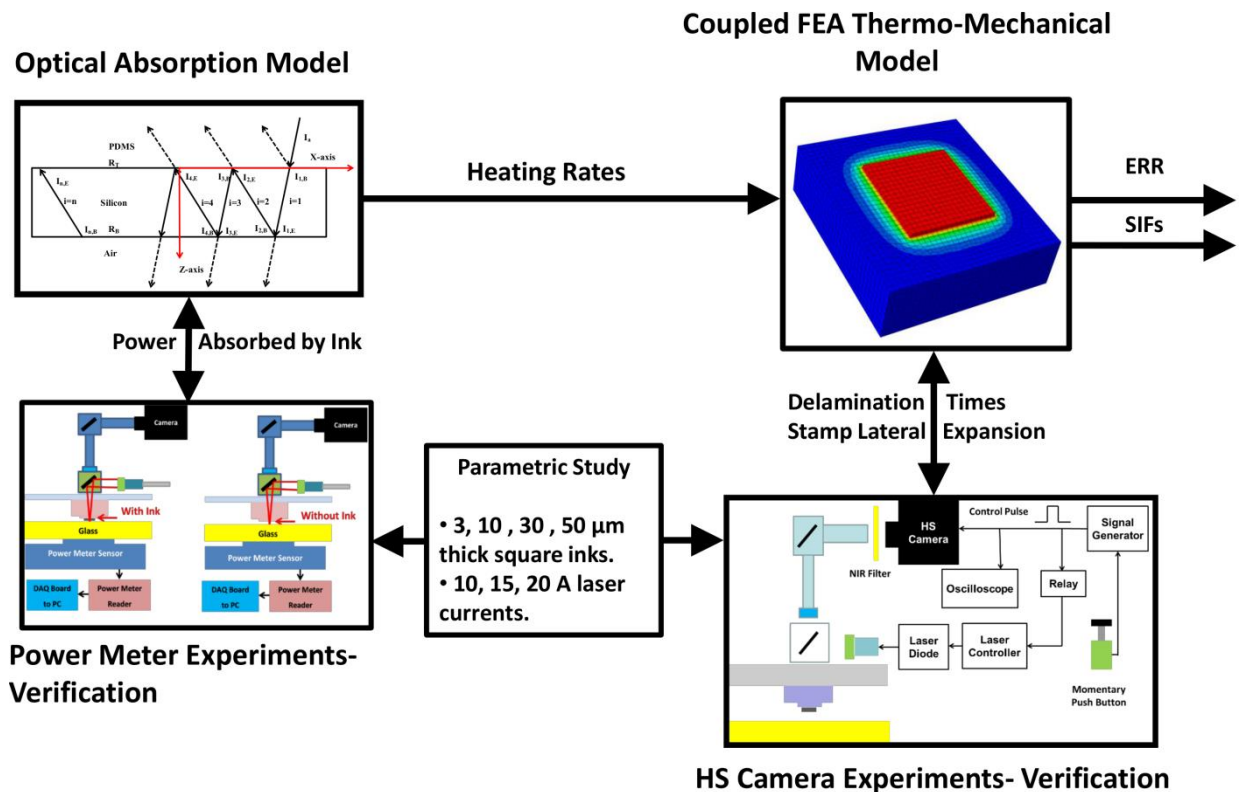
Figure 4.1. LMTP opto-thermo-mechanical delamination modeling approach.

4.3 Optical Absorption Modeling

In LMTP the ink absorbs the laser radiation and becomes a heat source for the ink-stamp composite. In this setup and experiment, because the largest ink is a square with sides of 200 µm, the beam power distribution is flat for about 400 µm (see Fig. 3.5) and the centers of the beam and ink are aligned during setup, it is reasonable to assume a constant intensity I_a for the radiation that produces heating. If A_a is the area of the ink, then the power of the uniform beam portion that is incident on the ink (and is available for heating) is given by $P_a = I_a A_a$ (see appendix A for Gaussian beam intensity heating). A part of this incident energy will be reflected by the surface of the ink and some portion of it that enters the silicon (see Fig. 4.2). Due to absorption, the intensity of the beam being transmitted through the silicon drops exponentially, following the Beer-Lambert law. At the bottom surface of the ink, a fraction of the beam power is radiated out from the ink while the remaining is reflected back into the ink. This process continues for consecutive reflections at the top and bottom surfaces until the intensity diminishes to zero. If P_b is the total beam power absorbed by the ink, then it is the summation of the absorption in each passage of the beam from the top surface of the ink to the bottom, and vice versa. Thus,

$$P_b = \sum_{i=1}^{n} P_i \tag{4.1}$$

where n is the number of times the beam passes through the ink before its power diminishes to zero. Let R_T be the reflectivity at the top interface and R_B be that at the bottom interface of the ink. If absorption coefficient for the ink material at the wavelength of the laser radiation is α, the power absorbed density in the first pass through the ink as a function of distance traveled (z) is given by:

$$Q_1(z) = (1 - R_T)\alpha I_a e^{-\alpha z} \tag{4.2}$$
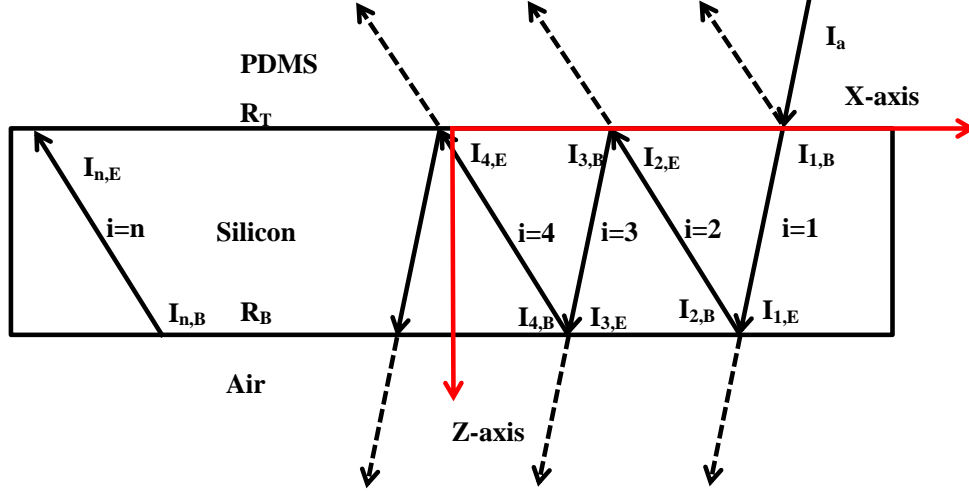
Figure 4.2. Multi-ray absorption in the LMTP process (the solid rays are the ones contributing to the optical absorption while dashed lines are the lost rays due to reflection or transmission). The rays are included for demonstration purposes only.

This yields, P_1, the power absorbed in the first pass through the ink:

$$P_1 = (1 - R_T)P_a[1 - e^{-\alpha h_s}] \tag{4.3}$$

A portion of the power arriving at the bottom surface of the ink is reflected back into the ink. This

yields power absorption, P_2 during the second pass:

$$P_2 = R_B(1 - R_T)P_a e^{-\alpha h_s}[1 - e^{-\alpha h_s}] \tag{4.4}$$

For any pass $i = 1, 2, 3, \ldots n$, P_i is given by:

$$Q_i(z) = \begin{cases} \alpha I_{i,B} e^{-\alpha z} & ; \quad i \; odd \\ \alpha I_{i,B} e^{-\alpha(h-z)}; & \quad i \; Even \end{cases} \tag{4.5}$$

$$P_i = R_i(1 - R_T)P_a e^{-(i-1)\alpha h_s}[1 - e^{-\alpha h_s}] \tag{4.6}$$

where

$$R_i = \begin{cases} R_T^{(\frac{i-1}{2})} R_B^{(\frac{i-1}{2})}; & i \; odd \\ R_T^{(\frac{i}{2}-1)} R_B^{(\frac{i}{2})}; & i \; Even \end{cases}$$

Given that $P_a=I_aA_a$ for uniform intensity heating, Eq. (4.6) suggests that the laser power absorbed by the ink for each pass increases linearly with the ink area and exponentially with the ink thickness. Considering the beam to be perpendicular to the ink surface, the reflectivity at the top and bottom surfaces of the ink, can be calculated from the refractive indices of the two media (n_1 and n_2) at the interface using:

$$R_S = \left(\frac{n_1-n_2}{n_1+n_2}\right)^2 \tag{4.7}$$
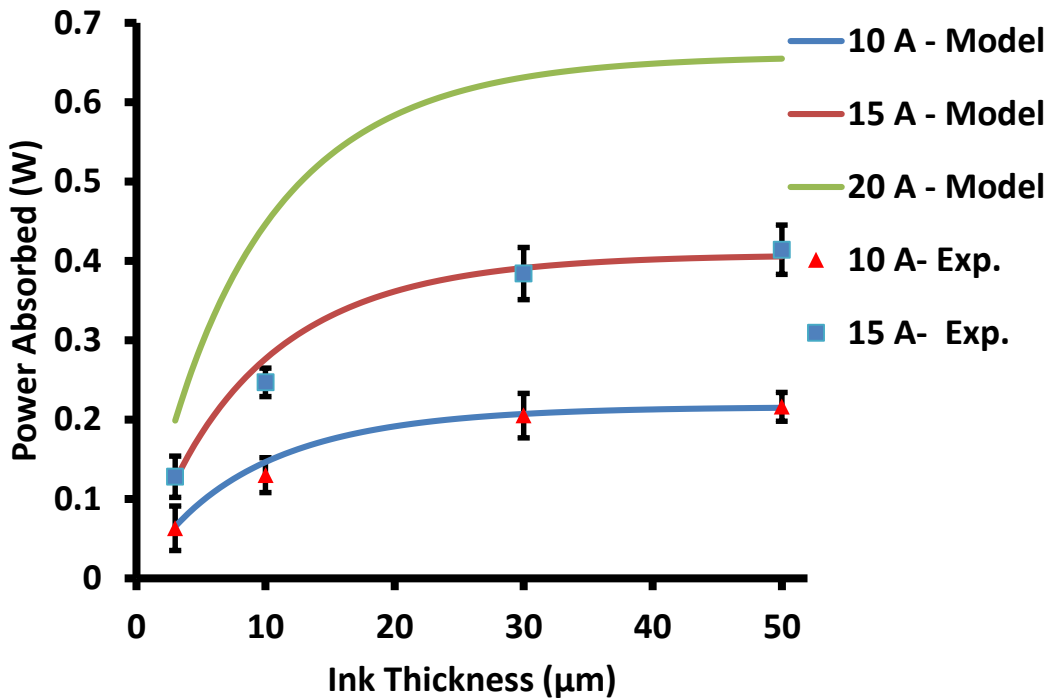
Figure 4.3. Model estimations and experimental results for different silicon ink thicknesses at different power levels.

With refractive indices at 805 nm for silicon $n_s = 3.5$, air $n_a = 1$, and PDMS $n_p = 1.42$, the reflectivity values for the top (silicon-PDMS) interface and the bottom (silicon-air) interface are determined to be $R_T = 17.63\%$ and $R_B = 30.86\%$, respectively. The model is then used to estimate

the laser beam power absorbed by 200×200 µm square silicon inks (with thicknesses of 3, 10, 30, 50 µm) at three different laser diode current (10, 15, and 20 A). The measurements of the power absorbed by the inks are performed using a 5.2 W maximum multi-wavelength power meter (PM100D; Thorlabs Inc.) by taking the average of the difference in power arriving at the meter with and without the ink in its path and accounting for reflective losses, as described in Section 3.5. A number of experiments were conducted to measure the laser beam power absorbed by 200×200 µm square silicon inks with four different thicknesses (3, 10, 30, 50 µm) at current settings of 10 and 15 A (20 A produces a power level above the measurement range of the meter). As shown in Fig. 4.3, the measured powers agree strongly with the model's predicted trends and values. The effect of accounting for the multi-internal reflections within the ink is shown in Fig. 4.4, where the model estimates for the power absorbed are improved by ~13%, 7%, 0.5%, and 0.5 % for 3, 10, 30, and 50 µm ink thicknesses, respectively. If one assumes uniform heating of the ink (justified by previous results from FEA simulations that show that there is no temperature gradient within the ink due to the high thermal conductivity of silicon), the estimated and measured heating rates are shown in Fig. 4.5. Larger ink thicknesses usually exhibit lower heating rates due to the large ink thermal mass even though the amount of power absorbed by thicker inks is higher. The uncertainty in the measurements of the heating rates are larger for thinner inks because the difference between the energy of the two laser pulses (with and without the ink) is low compared to the measured pulses energy (low S/N ratio).
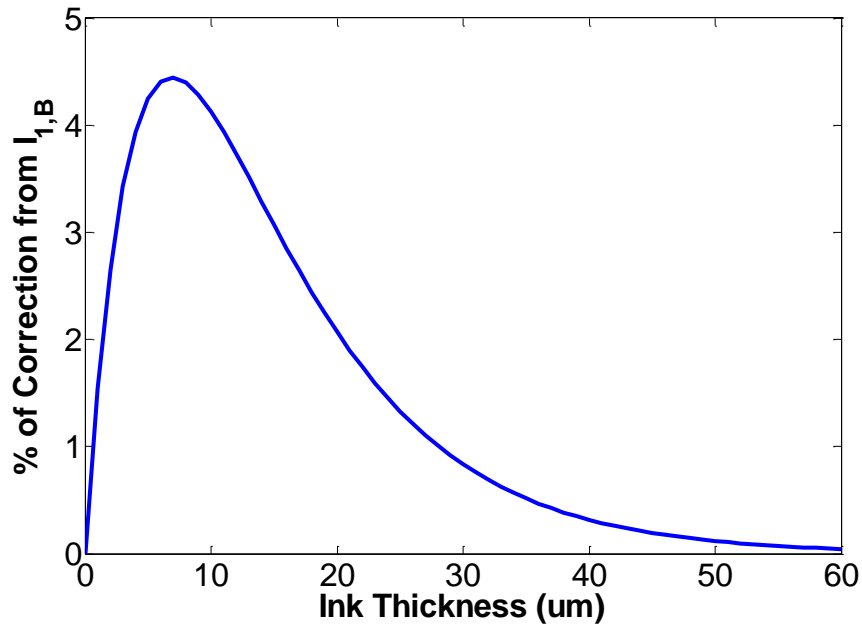
Figure 4.4. Model estimations for the percentages of correction from $I_{1,B}$ intensity due to multi-internal reflection passes for different silicon ink thicknesses.
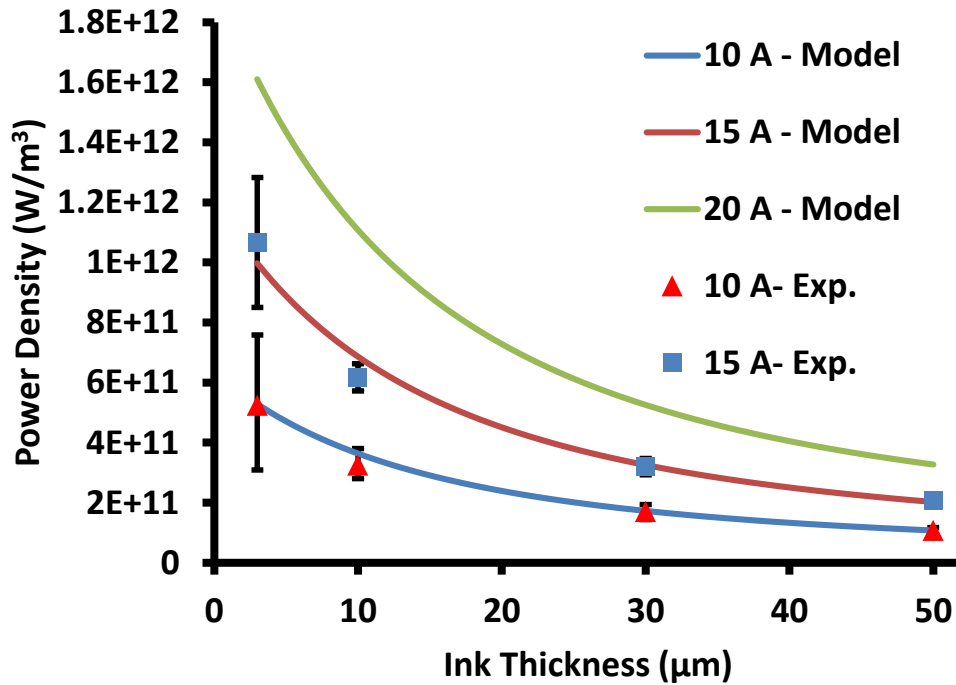
Figure 4.5. Comparison of the model estimation and the experimental values of the heating rates for different silicon ink thicknesses at different laser power levels.

4.4 Thermo-Mechanical FEA Modeling

4.4.1 Delamination Time Experiments

Using the experimental approach in Section 3.4, the effect of varying 200×200 μm square silicon ink thicknesses (3, 10, 30, 50 μm) and laser beam power levels (10, 15, 20 A) has experimentally been investigated to estimate the pulse duration of the laser required to start the delamination process. Figure 3.6 shows the trends for the delamination time, trends that were obtained from the experiments using a high-speed camera at frame rates of 8000 frame/sec. with a PDMS stamp having a 400×400×50 μm post (R = 2; h_p = 50 μm). The results show that the thinner the ink (from 3 to 50 μm thickness) or the higher the power level (from 10 to 20 A power levels), the shorter the delamination time. The results also show insignificant differences in printing ink with 3 and 10 μm thicknesses. For most of the printing conditions, except at 30 and 50 μm thickness at 10 A current level of the laser, the delamination, once started, is completed within one frame (< 0.125 msec.) of the high-speed camera. Because the ink heating rates for these two cases (30 and 50 μm thicknesses at 10 A power level) are slow, the delamination process can be observed to take 0.625-0.75 msec. (equivalent to 0.133-0.16 m/sec. delamination propagation speed) and 0.75-0.875 msec. (equivalent to 0.114-0.133 m/sec. delamination propagation speed), respectively. These experimental values of the delamination times are used as inputs for the FEA thermo-mechanical model, in which the model is evaluated up to the delamination times measured experimentally.
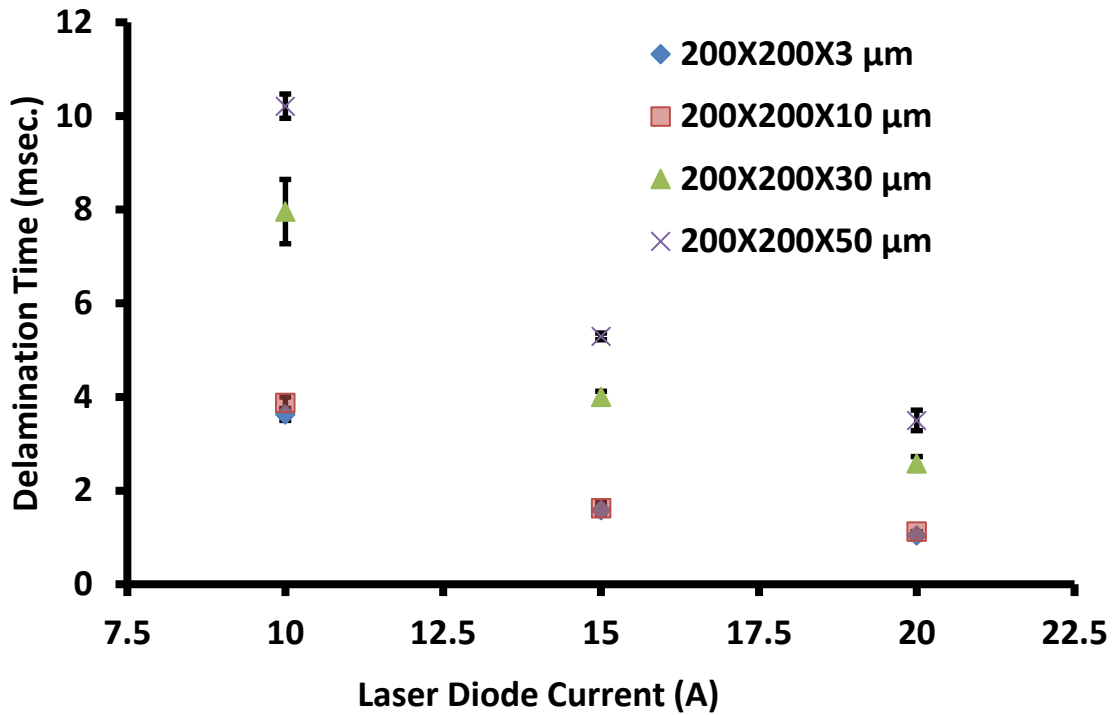
Figure 4.6. Experimental values of the LMTP delamination times for different power levels and ink thicknesses (3 and 10 μm series overlap at all current levels).

4.4.2 Thermo-Mechanical FEA Model Development

A coupled 3D transient thermo-mechanical model is developed in ABAQUS using reduced integration quadratic coupled temperature-displacement elements accounting for the large material deformation. The model input is the uniform heating rate estimated from the optical absorption model in Section 4.3 as a body heat source in the silicon ink. The model assumes linear elastic material behavior where the material properties are listed in Table 4.1. Because modeling the backing layer of the PDMS stamp thickness does not affect the output results if the post height is sufficiently large, a large PDMS post height of 100 μm is used for these simulations. A displacement boundary condition is enforced at the end of the PDMS post to restrict the translational and the rotational movement of the elements' nodes at the post end. The conduction

heat transfer model assumes heat losses of the surrounding environment at 20°C based on a heat transfer coefficient of 25 W/ (m^2 .°C). At the edge of ink-stamp interface, a 2 µm crack is introduced to collect the ERR and the SIFs based on the J-integral method and interaction integral method, respectively. To calibrate the model, a 3D model with 10 µm global element size was used to simulate the printing of 200×200×50 µm ink up to the delamination start time (9.75 msec.) at 10 A current level. Using the same ink, the maximum lateral deformation of the post was experimentally measured by imaging the ink-stamp system from the top, using a high-speed camera, as shown in Fig. 4.7-a and 4.7-b. The experimental results show that the lateral dimension of the post at delamination point increases by 1.76% (equivalent to L_f - L_o = 7.05 µm with 0.56 µm pixel resolution) compared to 6.01 µm estimated from the 3D model output (Figure 4.7-c). Therefore, one can conclude with reasonable confidence that the modeling approach (the power absorption and the FEA thermo-mechanical) is able to predict the LMTP optical-thermo-mechanical interaction and the process behavior up to the start of delamination with acceptable accuracy (i.e. see Fig. 4.8-a, 4.8-b, and 4.8-c for 3D model thermo-mechanical field results at the delamination point).

To ensure independence of the mesh size, it would be necessary to evaluate finer meshes than the 10 µm equally sized cubical elements for the 3D FEA model. However, the computational power and time grow exponentially with reducing mesh size. Therefore, the use of an equivalent area Axisymmetric (AS) model and a 3D cylindrical model with the same mesh size (10 µm mesh size; ink radius r_s = 225 µm and post radius r_p = 450 µm) are first evaluated. The results for square 3D model, cylindrical 3D model, and the axisymmetric model at different global meshing size models are shown in Table 4.2. The results indicate that the cylindrical or the axisymmetric model can be used to reasonably approximate the printing of the square inks, neglecting the corner effects.

Table 4.1. List of the thermo-mechanical material properties used for the LMTP study.

Propriety	Silicon	PDMS
Young's Modulus (GPa)	179.4	0.002
Poisson's Ratio	0.28	0.49
Density (kg/m^3)	2330	970
Thermal Expansion (ppm/ºC)	2.6	310
Thermal Conductivity (W/(m.ºC))	163	0.15
Heat Capacity (J/(Kg.ºC))	703	1460
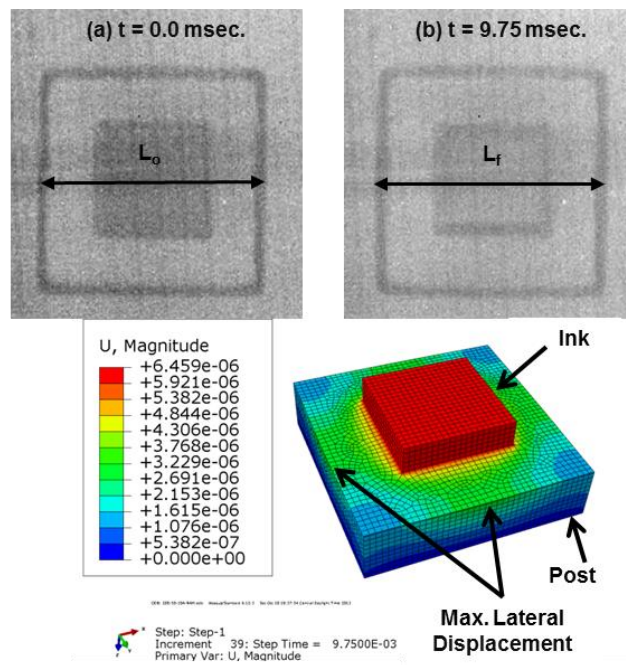
c) **FEA model displacement at t = 9.75 msec.**

Figure 4.7. 3D model calibration of LMTP based on the lateral deformation of the post during printing of 200×200×50 μm ink at 10 A laser current, (a) image of the ink-post system at t = 0 msec., (b) image of the ink-post system at delamination start time t = 9.75 msec., and (c) 3D model max. lateral deformation (m) at t= 9.75 msec.

Further, from the axisymmetric model results show that the stresses, strains, and strain energy density fields are mesh-dependent due to the geometrical singularity at the interface edges. On the other hand, the primary element variables (displacements and temperature) and the fracture mechanics quantities (ERR, SIFs) are mesh-independent. Figure 4.8-d shows the ERRs as a function of the laser pulse time for the different models in printing $200\times200\times3$ µm ink at the 10 A current level. The ERRs for the 3D square model are higher at the corners compared to the other locations at the interface edge. Moreover, the 3D cylindrical model and the axisymmetric model have ERRs in between the two values of ERRs at the corner and the edge from the 3D square model, being closer to the ERR at the edge. Because the ERR has to equal the work of the adhesion at each individual location at the crack perimeter for crack propagation, the axisymmetric model is expected to overestimate the ERR values at the edge of the square ink. In experiments involving printing equivalent area square and round inks, round inks require less time to print (4-10 %; see Section 5.5) compared to square inks. This agrees with the axisymmetric model's estimate of a higher ERR at the interface edge. In summary, the axisymmetric model with 1 µm meshing element size can be used to estimate the printing of square inks using the LMTP process.
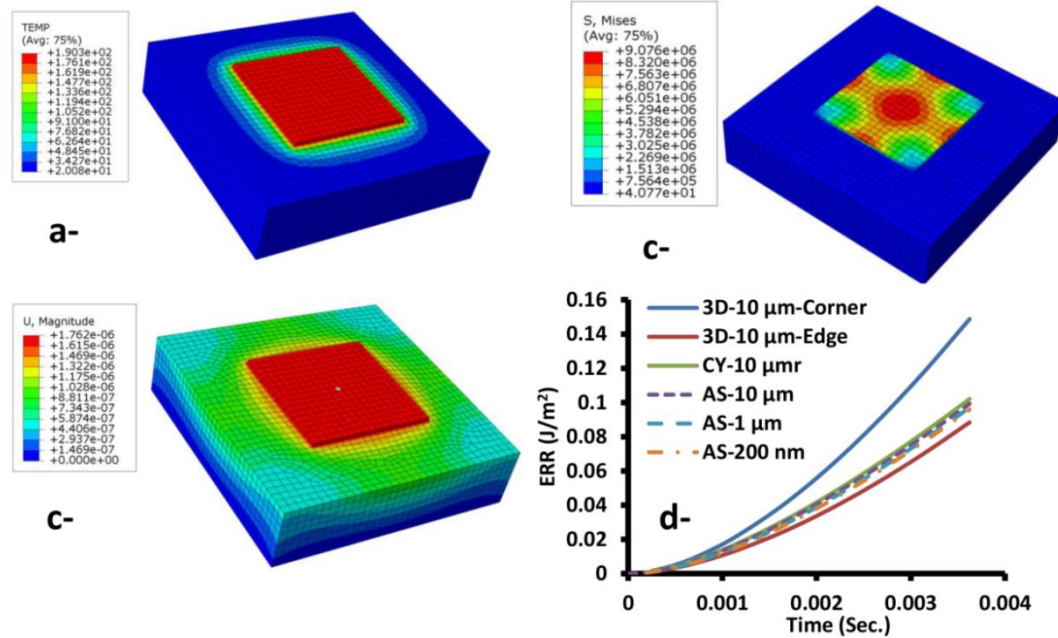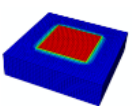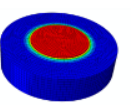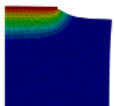
Figure 4.8. Thermo-mechanical model results for printing 200×200×3 μm ink at 10 A laser current, (a) tempertaure field (ºC), (b) stress field (MPa), (c) total displacment field (m), (d) comparison of different thermo-mechanical FEA models ERR values at the ink-stamp interface edge.

Table 4.2. Comparison of the different thermo-mechanical FEA models and meshing sizes for printing 200×200×3 μm ink at 10 A laser current.

Model Type (i.e. Deformed Temperature Field)					
Global Mesh Size (μm)	10.0	10.0	10.0	1.0	0.2
Interface Temperature (ºC)	171	188	198	201	202
Max. Strain Energy Density at Ink Edge (J/m³)	Corner-2.91 E4	1.31 E4	2.54 E4	1.35 E5	6.92 E5
Max. Stress Mises at Ink Edge (Mpa)	Corner-13.98	12.01	11.76	12.66	15.47
Max. Post Axial Displacement (μm)	2.10	2.21	1.98	1.99	2.11
Max. Post Lateral Displacement (μm)	1.02	0.89	0.96	0.96	0.94
ERR at Ink Edge (J/m²)	Corner-0.149 Edge- 0.088	0.102	0.099	0.097	0.096

4.4.3 Axisymmetric FEA Model Results

Using the axisymmetric model, the fields for the thermo-mechanical variables at the delamination point are shown in Fig. 4.9. The temperature field (Fig. 4.9-a) shows no thermal gradient within the silicon ink and a large thermal gradient within the PDMS post due to low thermal conductivity of PDMS. After 50 μm from the ink-stamp interface, the thermal field within the PDMS becomes uniform (room temperature). The results also show that the axial heat flux (see Fig. 4.9-b) from the silicon ink to the PDMS post is almost uniform at the interface except around the crack edge. Because the silicon ink has a comparatively low CTE and is subjected to a uniform temperature field, it undergoes a little thermal expansion or deformation and, instead, undergoes a predominantly translational displacement that is generated by the thermal expansion of the PDMS post in the vicinity of the contact interface (Fig. 4.9-c and 4.9-d show the total displacement and the axial displacement fields, respectively). In addition, the uneven temperature in the PDMS leads to large strain gradients and hence the deformation of the PDMS post in the vicinity of the silicon ink. Figure 4.9-e and 4.9-f show the mode I (opening mode normal to interface direction) strain and stress fields, respectively, while Fig. 4.9-g and 4.9-h show the mode II (shearing mode along the interface direction) strain and stress fields, respectively. Because the traction at the interface is equal, the stress fields in mode I and mode II direction are continuous and smooth, while the strain fields in both directions are discontinuous, especially at the interface edge, due to the large mismatch in Young's modulus at the interface. Therefore, the locations of maximum stress, strain, and strain energy density points are always at the interface edge in the axisymmetric model (at the corners for 3D square model). Thus, the temperature of the Si-PDMS interface and the thermal gradient around the edges of the silicon ink are responsible for initiation and propagation of the crack.
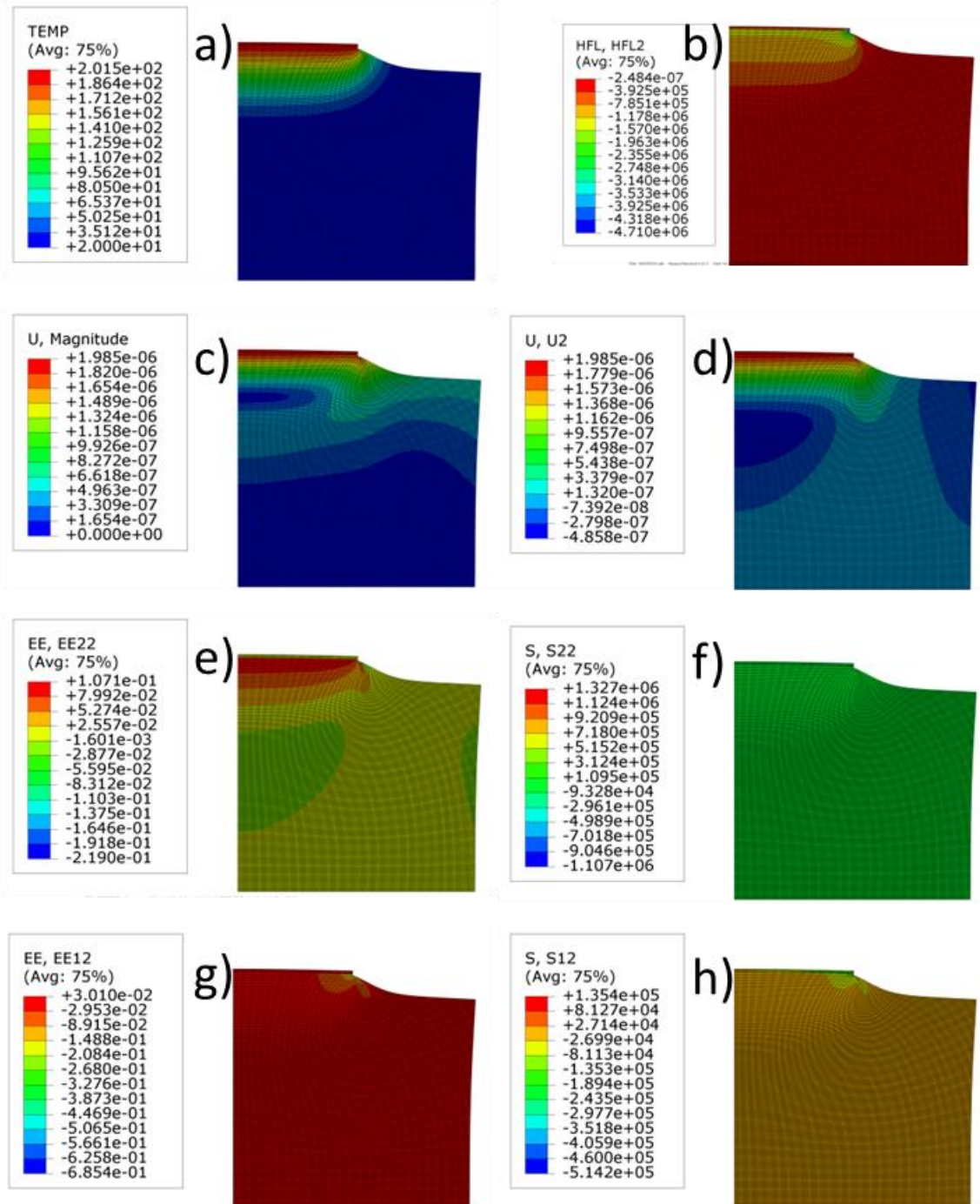
Figure 4.9. Coupled thermo-mechanical FEA field outputs for printing 200×200×3 µm ink at 10 A laser current, (a) temperature (°C), (b) heat flux in axial direction (W/m²), (c) displacement (m), (d) axial displacement (m), (e) mode I strain, (f) mode I stress (Pa), (g) mode II strain, and (h) mode II stress (Pa).

Figure 4.10. Interface temperatures estimated from AS model for different ink thicknesses at different power levels, (a) 10 A current, (b) 15 A current, and (c) 20 A current.

Figure 4.10-a, 4.10-b, and 4.10-c show the model estimations for the interface temperature as a function of time, essentially similar to the curves for silicon ink temperature, for different ink thicknesses up to the delamination time (measured in Section 4.4.1) at 10, 15, and 20 A laser current, respectively. The curves show that regardless of the current levels, thin inks (3 and 10 µm) print roughly at the same delamination time and at a lower temperature compared to thick inks (30 and 50 µm). Further, thick inks print almost roughly at the same interface temperature. The interface temperature rise rate increases with the laser current. Finally, under all conditions, the rate of temperature change is highest for 10 µm inks, suggesting that at these power levels, the 10 µm ink thickness gives the best balance between the thermal energy stored in the ink and the energy transferred to the PDMS stamp.

During printing, when inks with different thicknesses are printed using the same stamp dimensions, the heat flux from the silicon ink to the PDMS can be considered as a measure for both: the rate at which thermal energy is converted into strain energy, and its localization around the ink-stamp interface. Therefore, heat flux output from the FEA model (see Fig. 4.11-a, 4.11-b, and 4.11-c for 10 , 15 , and 20 A, respectively) suggests that the time constant for heat flux depends on the ink thickness (longer time constant for thicker inks, which agrees with the analytical mode developed in [97]).Therefore, thin inks (3 and 10 µm) almost reach a steady state heat flux within the delamination time, while the heat fluxes for thick inks (30 and 50 µm) are still increasing when delamination occurs at all laser beam power levels. The heat flux graphs in Figure 4.11 show that the initial heat flux is highest for thin inks, due to the low heat capacities of the thin inks. The lowest and the highest total thermal energy flux to the PDMS (Fig. 12-a, 12-b, and 12-c for 10, 15, and 20A) are observed for 50 and 10 µm for all power levels, respectively. This indicates that temperature rise rates for the interface temperatures depend not only on the ink heating rate (higher

Figure 4.11. Heat fluxes to PDMS post from silicon ink estimated from AS model for different ink thicknesses at different power levels, (a) 10 A current, (b) 15 A current, and (c) 20 A current.

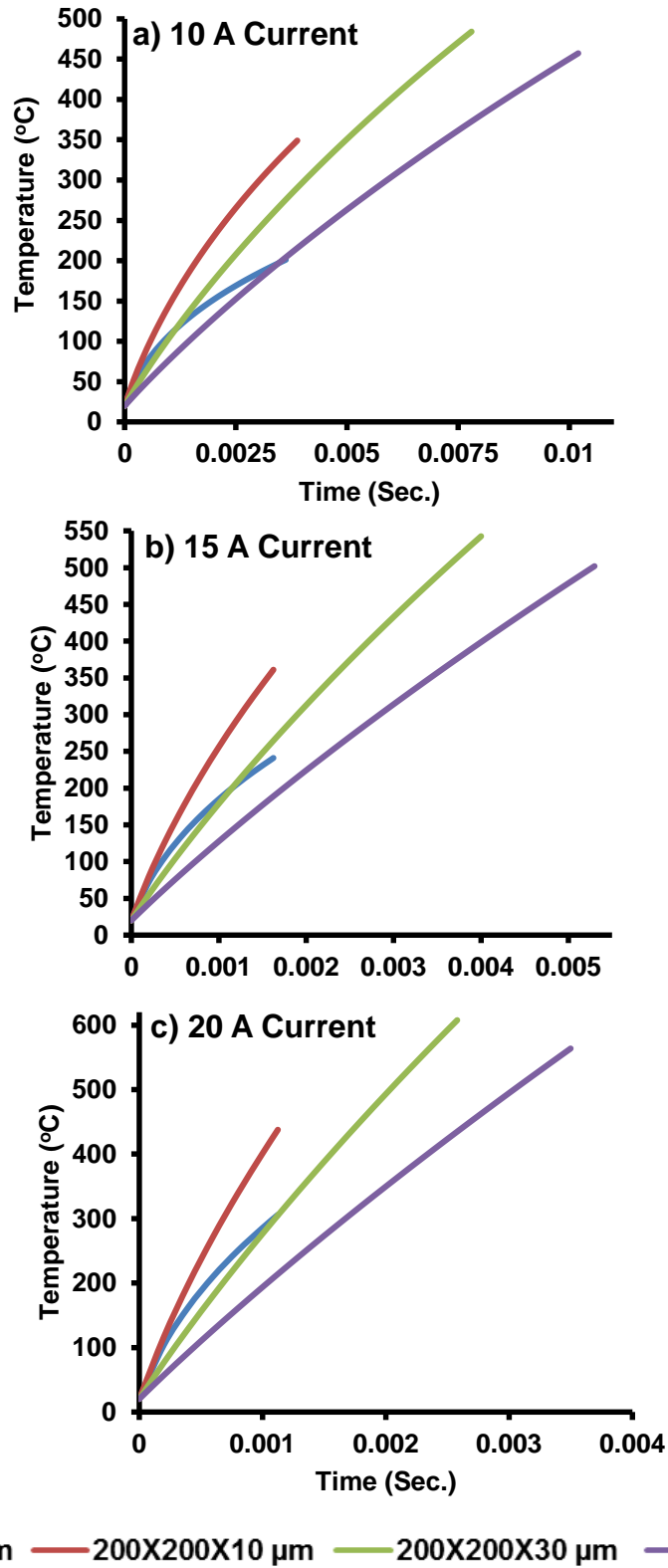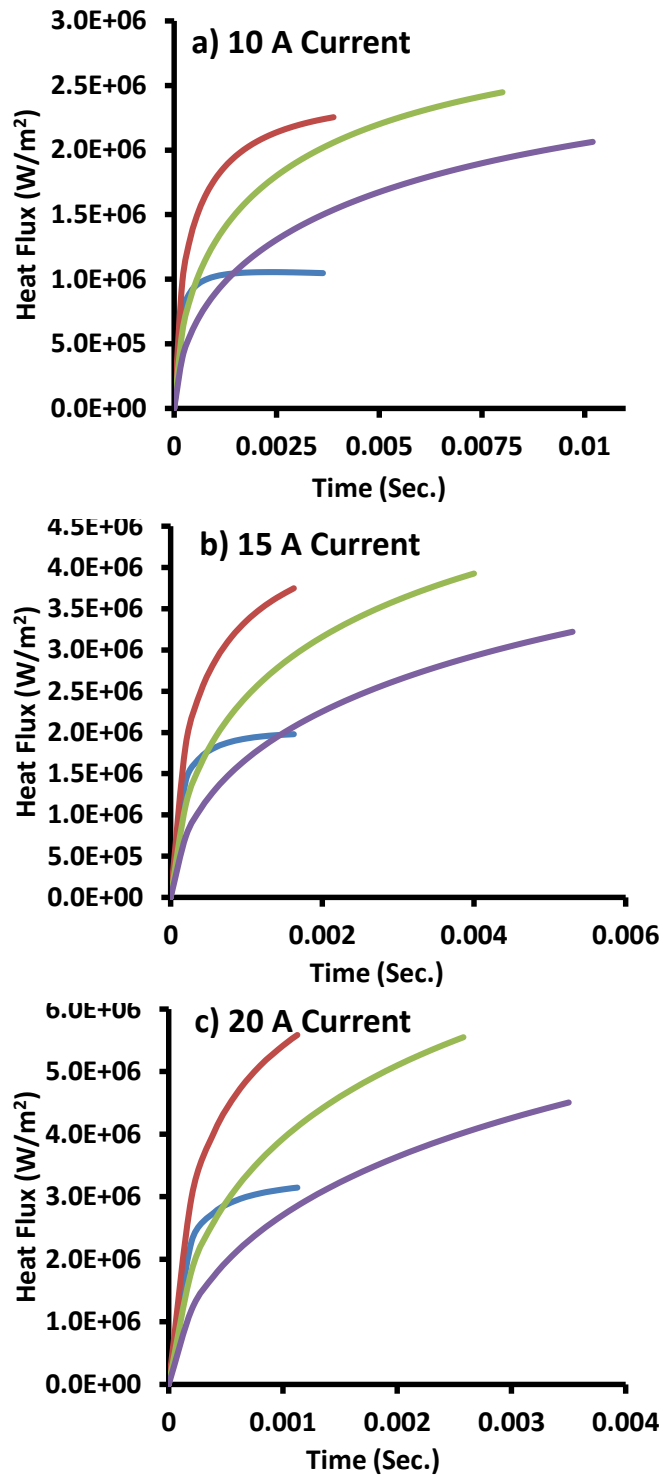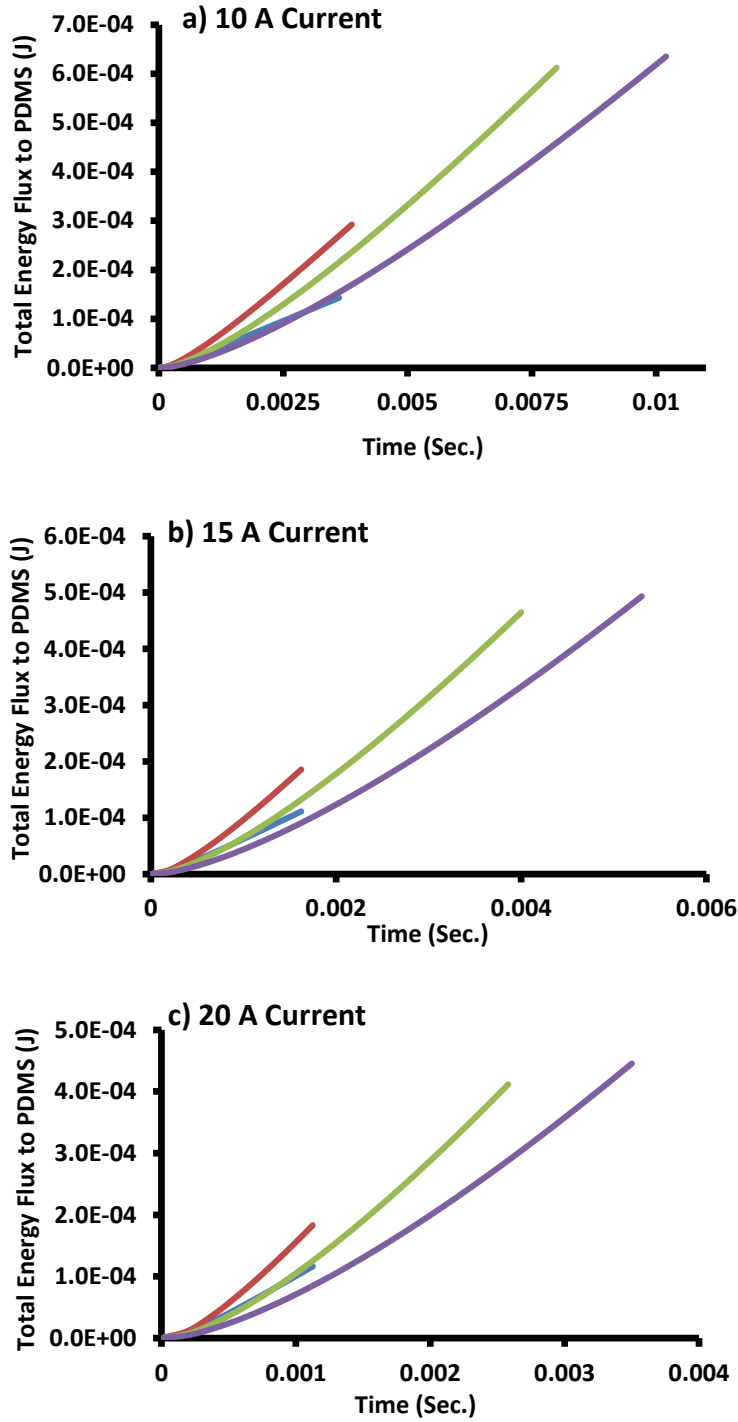**Figure 4.12. Total thermal energy fluxes to the PDMS post from the silicon ink estimated from AS model for different ink thicknesses at different power levels, (a) 10 A current, (b) 15 A current, and (c) 20 A current.**

for thinner inks), but also the thermal capacity (higher for thicker inks) of the ink, which explains why the best thermal energy balance is around 10 μm. Table 4.3 summarizes percentages of the total energy flux to the PDMS stamp compared with the total energy absorbed by the ink at the delamination point. The results show that the percentages of energy flux to PDMS are higher for thinner inks, while the total energy flux to PDMS is lower for thinner inks (delamination energy is lower for thinner inks as described in Section 3.6). Further, percentages of total thermal energy fluxes to the PDMS stamp are higher for lower laser beam currents since they are associated with a longer delamination time and larger heat affected zone. This indicates that thinner inks have higher efficacy in transferring the thermal energy to the PDMS; however, the total energy absorbed by the ink, as described on the optical model in Section 4.3, is lower. Therefore, for printing active devices that can potentially suffer thermal damage, the LMTP process is probably better suited to printing thin devices (lower power absorbed, interface temperature, and higher heat flux to PDMS).

To avoid contact with the receiving substrate, the maximum axial displacement due the PDMS expansion should be less than the stand-off height of LMTP process. Such a contact produces a compressive stress across the ink-stamp interface that impedes the crack formation and propagation necessary for delamination. The maximum axial displacements of the silicon ink at the delamination time for the different thicknesses are obtained from the model and shown in Fig. 4.13-a. The results show that the higher the ink thickness from 3 to 30 μm, the higher the maximum axial displacement, while it is the same for thick inks (30 and 50 μm). Further, the maximum axial displacement for printing at 10 A laser current is higher than 15 and 20 A current levels because it is associated with a larger heat affected zone. This is consistent with observations of higher temperatures at the delamination time for thicker inks. Therefore, printing of thicker inks require

larger stand-off distances from the receiving substrate. This is an important consideration in assessing the overlay accuracy the process is capable of as large stand-off heights reduce the overlay accuracy of print as described in [4] while small stand-off heights (less than maximum axial deformation) can prevent delamination. All the results for the interface temperatures and maximum axial displacement assume a large printing gap (> 100 µm) between the ink and the receiving substrate to minimize thermal interactions. The effect of the print gap on the temperature of the interface for printing 3 µm inks at 10 A laser current is shown in Fig 4.13-b. The results show that a difference in the interface temperatures is less than 10 ^{o}C if the print gap is larger than 5 µm. For a smaller gap (i.e. 2 µm), the interface temperature is way less (~ 26 ^{o}C) because more heat fluxes to the receiving substrate through the thin air layer.

Table 4.3. Thermal energy fluxes to PDMS from the silicon ink at the delamination points.

Ink Thickness	3 µm	10 µm	30 µm	50 µm
10 A Current				
Delamination Time (Sec.)	0.0036	0.0039	0.0081	0.0102
Total Energy Flux (J)	0.000143	0.000293	0.000612	0.000635
Energy Absorbed (J)	0.000237	0.000569	0.001658	0.002192
% Energy transfer to PDMS	60.51%	51.44%	36.93%	28.96%
15 A Current				
Delamination Time (Sec.)	0.0016	0.0016	0.0041	0.0053
Total Energy Flux (J)	0.000111	0.000186	0.000465	0.000493
Energy Absorbed (J)	0.000201	0.000449	0.001564	0.002150
% Energy Transfer to PDMS	55.60%	41.33%	29.72%	22.94%
20 A Current				
Delamination Time (Sec.)	0.0011	0.0011	0.0026	0.0035
Total Energy Flux (J)	0.000116	0.000183	0.000411	0.000445
Energy Absorbed (J)	0.000224	0.000502	0.001629	0.002292
% Energy Transfer to PDMS	52.01%	36.51%	25.25%	19.43%
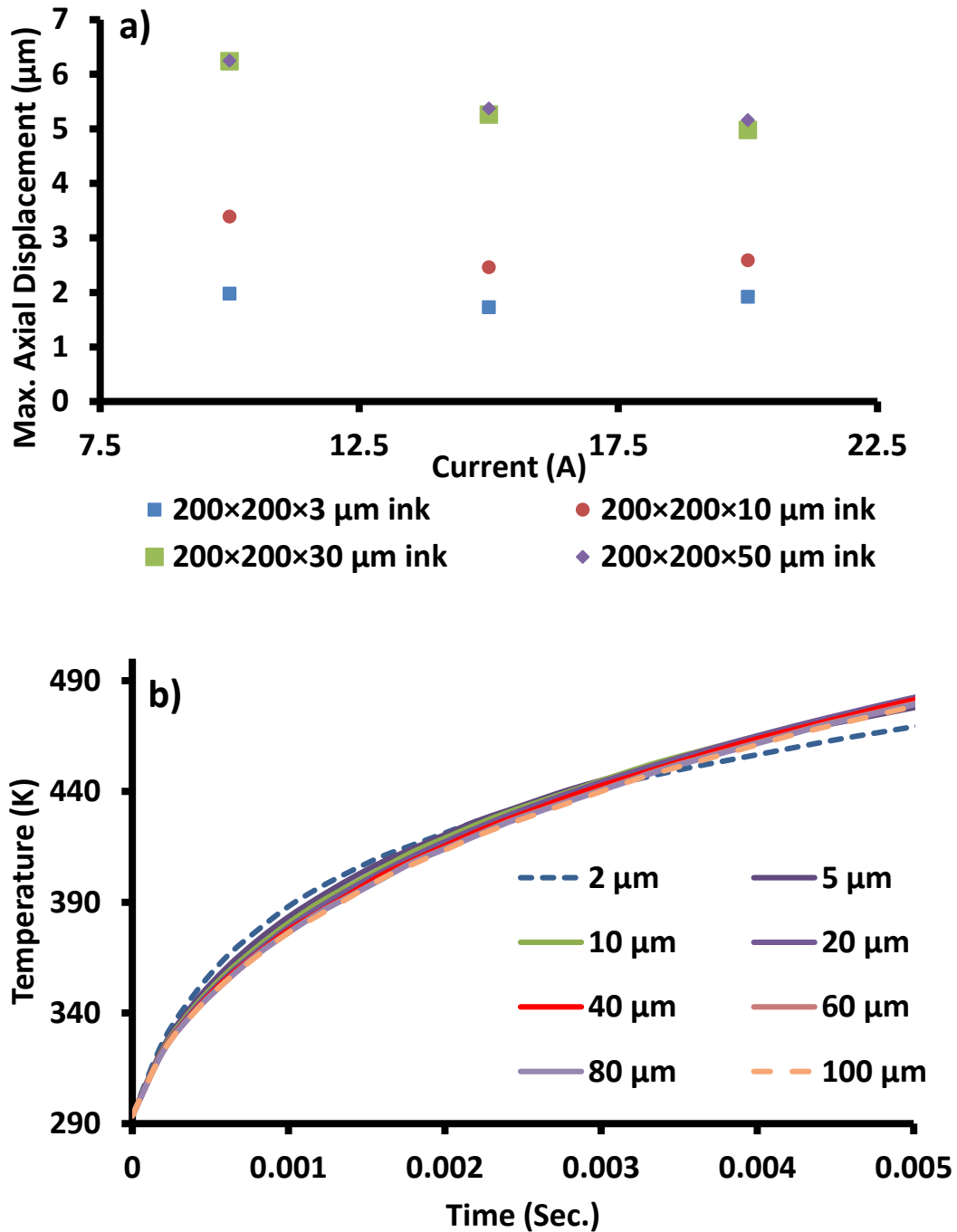
Figure 4.13. (a) Maximum axial displacement estimated from AS model for different ink thicknesses at different power levels, and (b) the effect of the printing gap on the interface temperature in printing 200×200×3 μm ink at 10 A laser current.

The ERRs at the crack tip are estimated using the J-integral method for the printing of different ink thicknesses and different laser current levels (see Fig. 4.14- a, 4.14- b, and 4.14-c for 10, 15, and 20 A, respectively). The results show that regardless of the laser current level, the ERR at delamination point for each ink thickness is almost constant, even though different inks require different delamination times at different laser current levels. Based on Griffith's criterion, the critical ERR values (G_c) at the delamination point should equal the work of adhesion for Si-PDMS interface (interface property reported to be 0.05-0.151 J/m^2 at room temperature [2] [102]). However, the results clearly indicate that the critical ERR G_c depends on the ink thickness, which is not expected. For 3 µm ink thickness, the critical ERR value (G_c ~0.1 J/m^2) approaches the average work of adhesion of the interface, which indicates that the model estimates for the delamination times are accurate (< 10% error) for all current levels. However, the G_c values are higher than the work of adhesion for the thicker inks (10, 30, and 50 µm). This indicates a discrepancy between the model estimates and the experimental values of the delamination times (model estimate about two-to-three times higher) at all current levels. Therefore, to understand the LMTP process mechanism, a further step should be taken to decompose the ERR buildup at the interface edge to its basic strain energy components (CTE mismatch and thermal gradients) in both fracture mode directions.
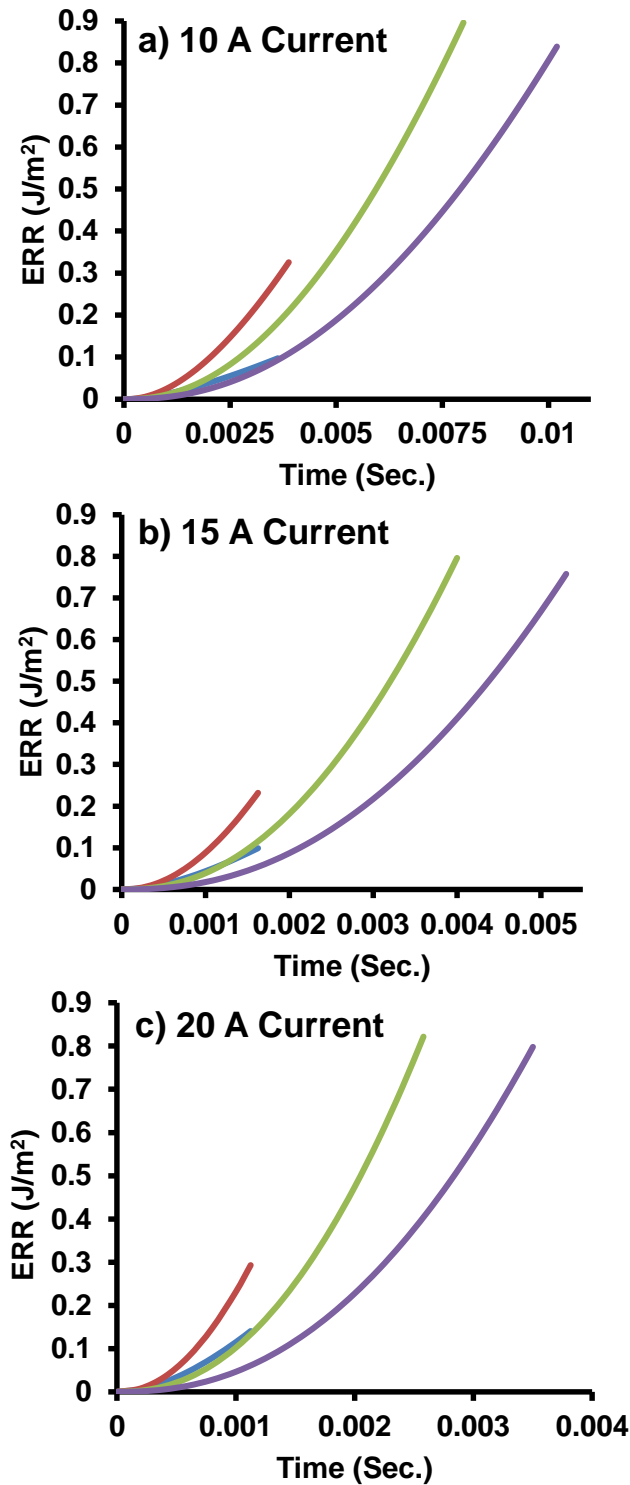
Figure 4.14. ERRs estimated from AS model for different ink thicknesses at different power levels, (a) 10 A current, (b) 15 A current, and (c) 20 A current.

4.5 Thermal Strain Energy Components

From linear fracture mechanics theory, the ERR value $G = \frac{1}{E^*}(K_I^2 + K_{II}^2)$ is a composition of the SIFs squares at the crack tip. Figure 4.15-a and 4.15-b show the model estimates for the opening mode SIF (K_I) and shear mode SIF (K_{II}) for printing different ink thicknesses at 10 A current level. The results show that the LMTP delamination process is a mixed-mode fracture problem where K_I has a positive value (tensile load in mode I trying to open the interface) and K_{II} has negative value (negative shear load in mode II trying to squeeze the interface toward interface center). The SIFs' trends are similar to the ERR where thin inks print at lower SIFs, in mode I and mode II, compared to thick inks. The mode II contribution on building up the ERR at the interface edge is almost two times higher than that for mode I for all ink thicknesses and laser currents (see Fig. 4.16-a, 4.16-b, and 4.16-c for 10, 15, and 20 A currents, respectively). Further, SIFs rise rates as a function of laser beam pulsing time are higher for the inks that have higher interface temperature rise rates. Therefore, evaluating the SIFs in both fracture modes for different ink thicknesses as a function of the interface temperature (see Fig. 4.17-a, and 4.17-b for mode I and mode II, respectively) shows that all ink thicknesses build up the same SIF at a given interface temperature in both fracture mode directions. This indicates that SIF values, in both fracture modes, are dependent on interface temperature and independent of the ink's geometry (difference in SIFs as a function of laser pulsing time are due to different heating rates).
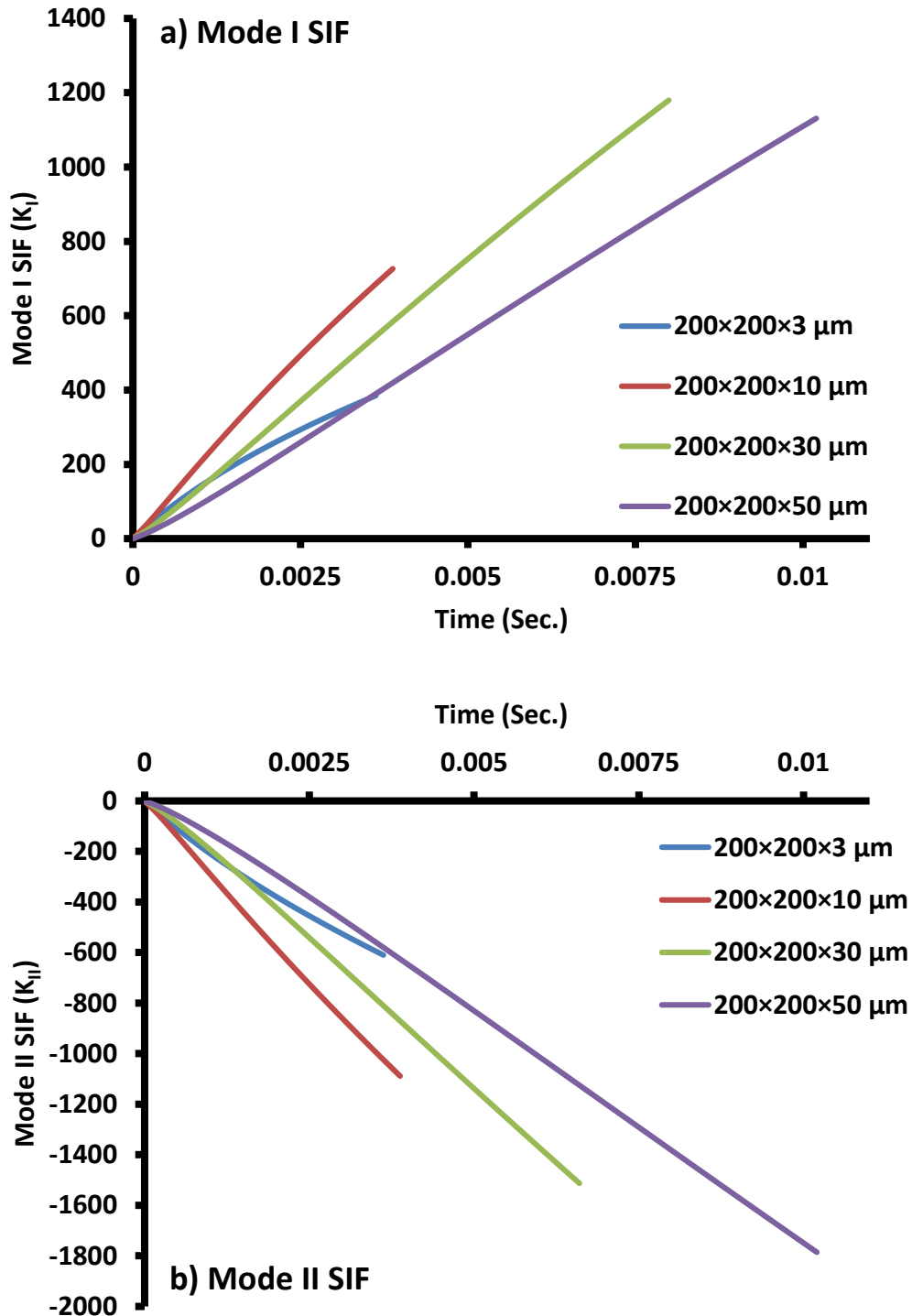
Figure 4.15. SIFs at crack tip at the ink-stamp interface estimated from AS model as a function of laser pulse time for different ink thicknesses at 10A laser current, (a) mode I SIF, and (b) mode II SIF.
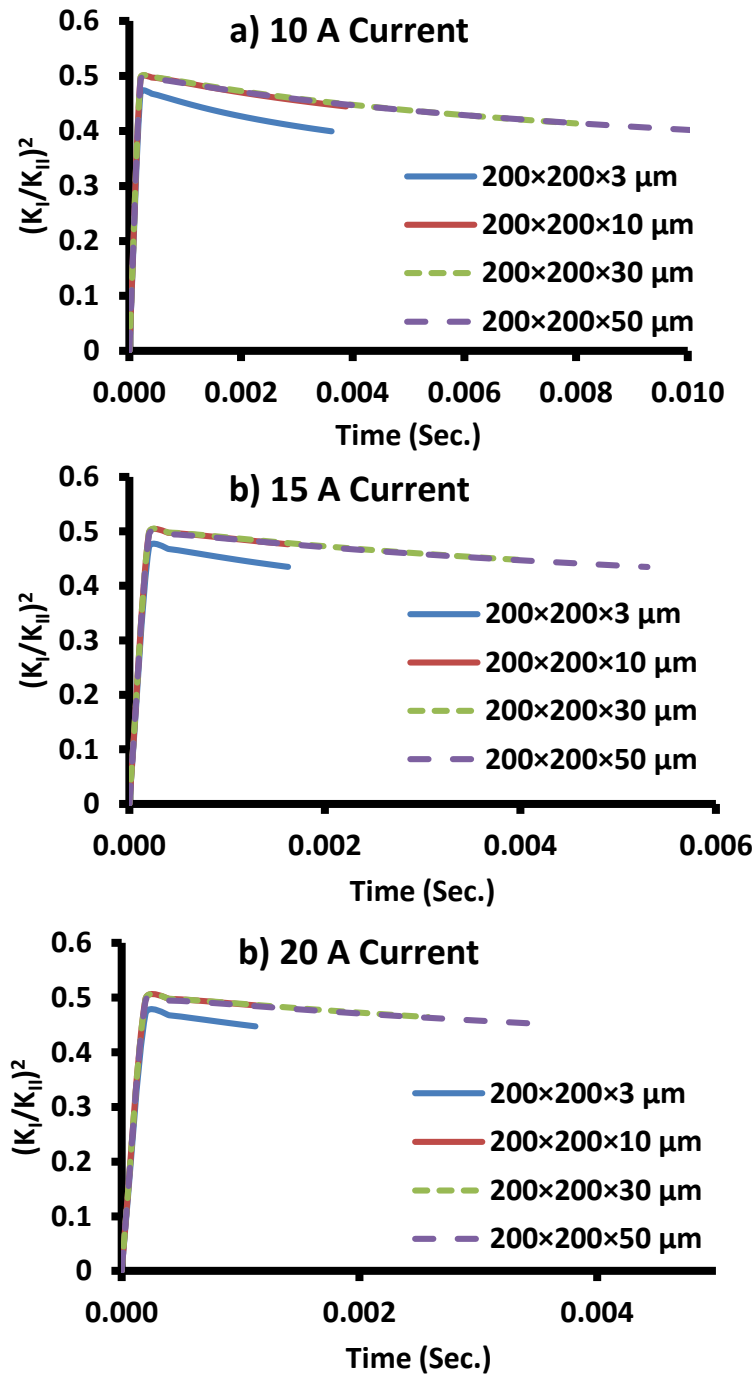
Figure 4.16. Dominant SIFs at crack tip at the ink-stamp interface estimated from AS model as a function of laser pulse time for different ink thicknesses, (a) 10 A, (b) 15 A, and (c) 20 A.

Using the developed model, one can decompose the SIFs into two components based on the sources of thermal strains: CTE mismatch between the ink and the stamp, and thermal gradient within the PDMS. To obtain the effect of the thermal gradient, the model can be evaluated with both the materials having the same CTE (i.e. 310 ppm/^{o}C). On the other hand, uniform heating for the ink-stamp stack will eliminate the effects of the thermal gradient within the PDMS post. However, this will introduce thermal strains arising from the boundary condition, restricting the movement of the uniformly deformed PDMS stamp post. This boundary effect is an artifact, because in actual printing, the heat-affected zone is confined to a few microns (< 50 μm) from the interface because of the low thermal conductivity of the PDMS. To eliminate this boundary effect, a third model is constructed with matched CTEs and uniform heating. The SIFs along both modes from the three simulations are combined (the SIF for each mode from the matching CTE model is added to that from the uniform heating model and that from the model with matching CTE and uniform heating is subtracted from the result). The linear combination of the three virtual simulations is compared to the original model output to produce an exact match (see Fig. 4.18-a and 4.18-b for 200×200×3 μm ink at 10 A current level), suggesting that the assumption of linearity is valid and that the relative contributions of CTE mismatch and thermal gradients can be studied in this manner.
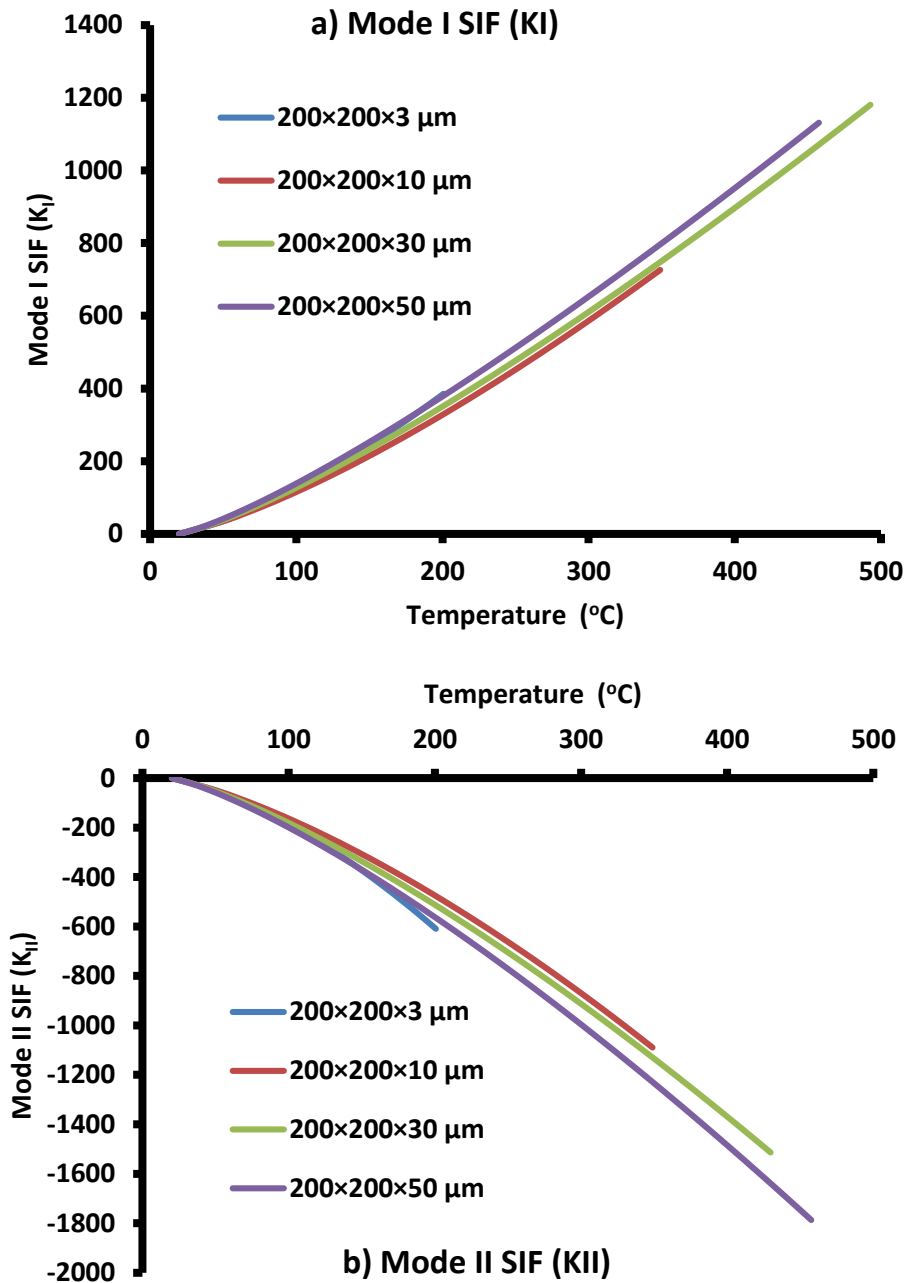
Figure 4.17. SIFs at crack tip at the ink-stamp interface estimated from AS model as a function of interface temperature for different ink thicknesses at 10 A laser current, (a) mode I SIF, and (b) mode II SIF.

Figure 4.18. SIFs thermal strain decomposition at crack tip at the ink-stamp interface estimated from AS model for 200×200×3 μm ink at 10 A laser current, (a) mode I SIF (K_I), and (b) mode II SIF (K_{II}).

This approach is then used to study printing of inks with different thicknesses at 10 A current (the same results hold for 15 and 20 A current level) as shown in Figure 4.19 (4.19-a for mode I SIFs K_I and 4.19-b for mode II SIFs K_{II}). The results show that for the mode I SIF, the CTE mismatch and thermal gradient mechanical strains both act in the same direction generating tensile strains trying to open the crack tip at the interface edge. In the mode II direction, however, the CTE mismatch introduces a negative shear load at the interface edges, squeezing the interface while thermal gradient strains generate a positive shear load that stretches the interface. Further, in both directions, the CTE mismatch strains have a linear relationship with the interface temperature while thermal gradient strains have a nonlinear relationship with the interface temperature. Furthermore, in mode I, because of non-linear growth, at higher temperatures (> 100 °C), the contribution of the thermal gradient in the PDMS to the accumulation of strain energy at the crack tip dominates that of the CTE mismatch for different ink thicknesses, indicating that the bending moment from the CTE mismatch load, in mode I direction, is less effective compared to the PDMS bulging due to thermal gradients within the stamp. The thermal gradient effect is also slightly lower for thin inks (3 and 10 µm) in mode I direction. In mode II, the contribution of the CTE mismatch is always higher than that of the thermal gradient strains generated at all temperatures for all ink thicknesses. The results from this decomposition approach imply that the thermal gradient within the PDMS plays an important and significant role during the LMTP process. Therefore, its high CTE coupled with its low thermal conductivity make PDMS a good stamp material for the LMTP process. Furthermore, this decomposing approach shows that the axial stamp deformation and the bulging of the stamp, both effects of the thermal gradient strains, have disappeared by uniformly heating the ink-stamp in the simulations.

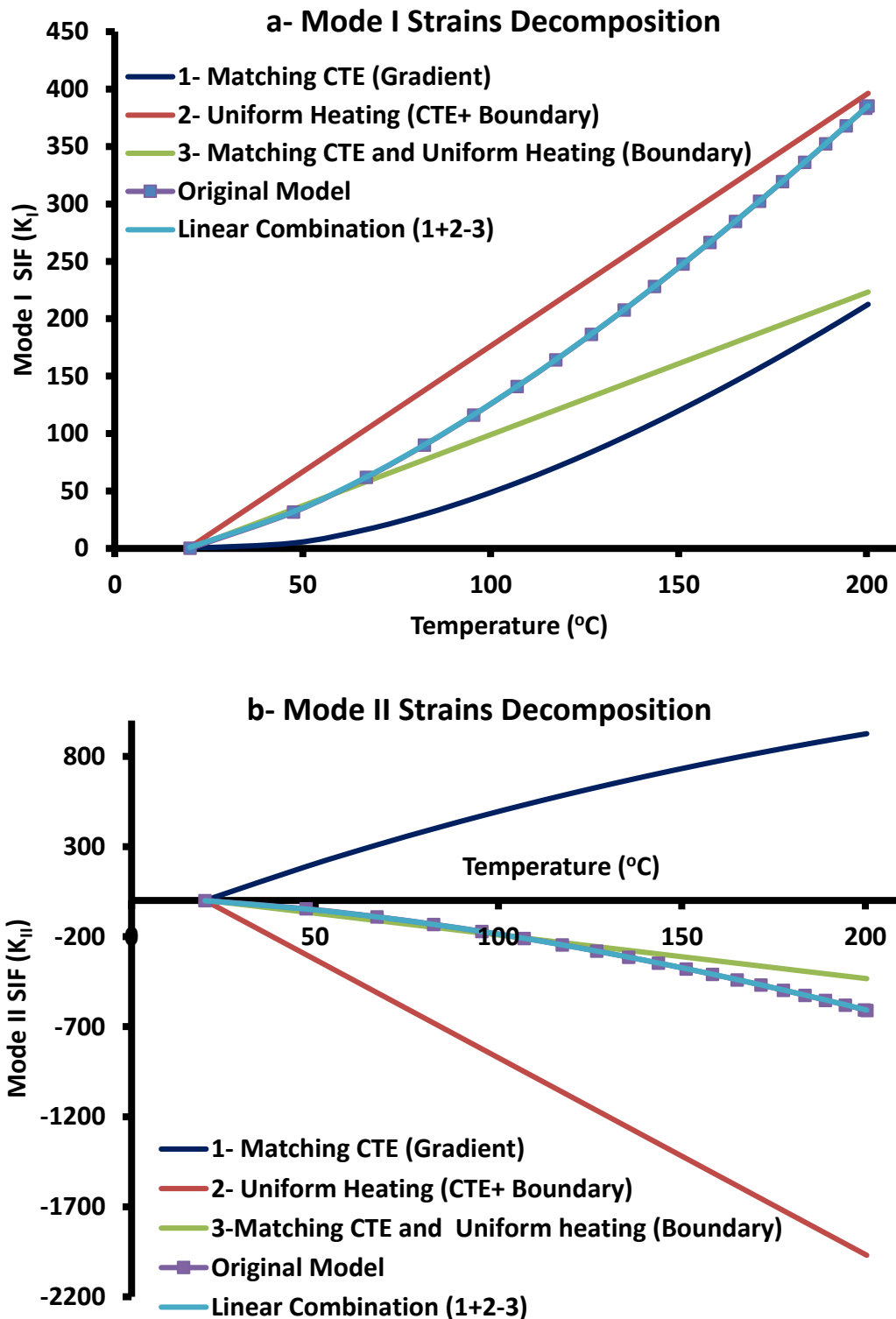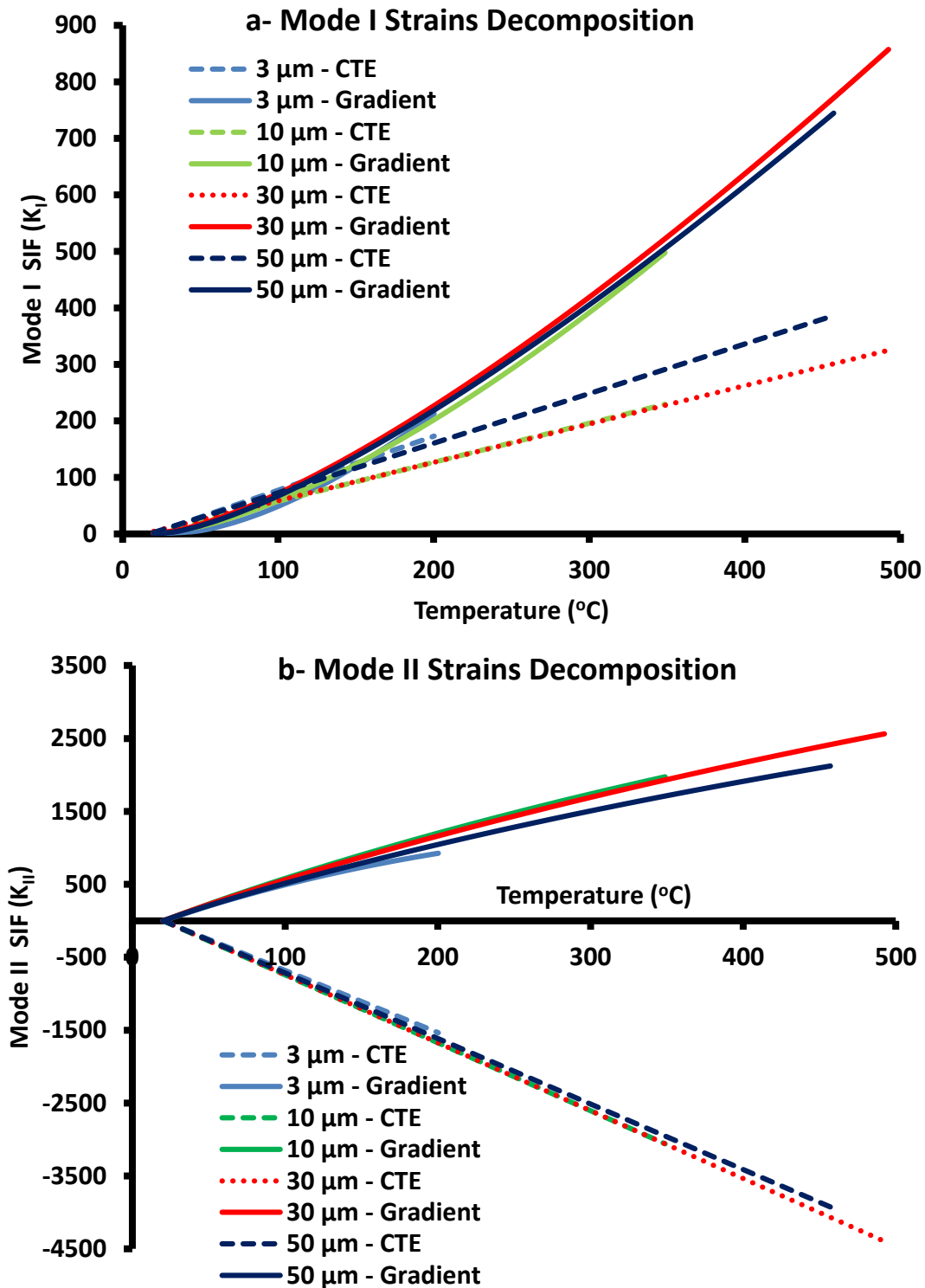**Figure 4.19. SIFs thermal strains decomposition at crack tip at the ink-stamp interface estimated from AS model for different ink thicknesses at 10 A laser current, (a) mode I SIF (K_I), and (b) mode II SIF (K_{II}).**

4.6 Cohesive Zone Modeling

The thermo-mechanical fracture model developed in Section 4.4 can be used to understand how the strain energy builds at the interface edge from the start of the laser beam pulsing until the start of the crack propagation. A CZM approach is then adopted because it has the capability to model the progressive nature of the thermo-mechanical delamination, showing the crack nucleation and the ink-stamp separation. The model is developed by defining a cohesive interface between the ink and the stamp based on the bi-linear traction-separation curve (which includes information about the work of adhesion of interface and maximum stress required to initiates the crack). The developed mechanical loads, due to laser heating, at the interface should separate any cohesive contact node at the interface if the developed strain energies and stresses are higher than the ones from the traction-separation curve. Two traction-separation curves are defined in both fracture directions (mode I and mode II), while the fracture criterion is based on a linear power-law. A stamp with height $h_p = 200$ µm is assumed based on previous results from Section 4.4 that show that the changes in the thermo-mechanical fields are localized around the interface (< 50 µm). Further, 1 µm element's mesh size is enforced at the ink-stamp interface to obtain an accurate numerical solution. For example, Fig. 4.20 and 4.21 show the CZM model results for the strain energy density field at different times starting from the laser pulsing moment for printing 3 and 50 µm inks at 10 A current, respectively. The results show how the crack is initiated (~ 3 msec. and ~ 4 msec. for 3 and 50 µm, respectively) and start propagated (~ 5 msec. and ~ 6 msec. for 3 and 50 µm, respectively). This indicates that the difference in the crack propagation start times (~ 5 msec. and ~ 6 msec. for 3 and 50 µm, respectively) are not significant compared to the experimentally measured delamination times (3.6 msec. and 10.2 msec. for 3 and 50 µm,

84

respectively). Further, the maximum strain energy density for both cases always follow the crack

tip during propagation.
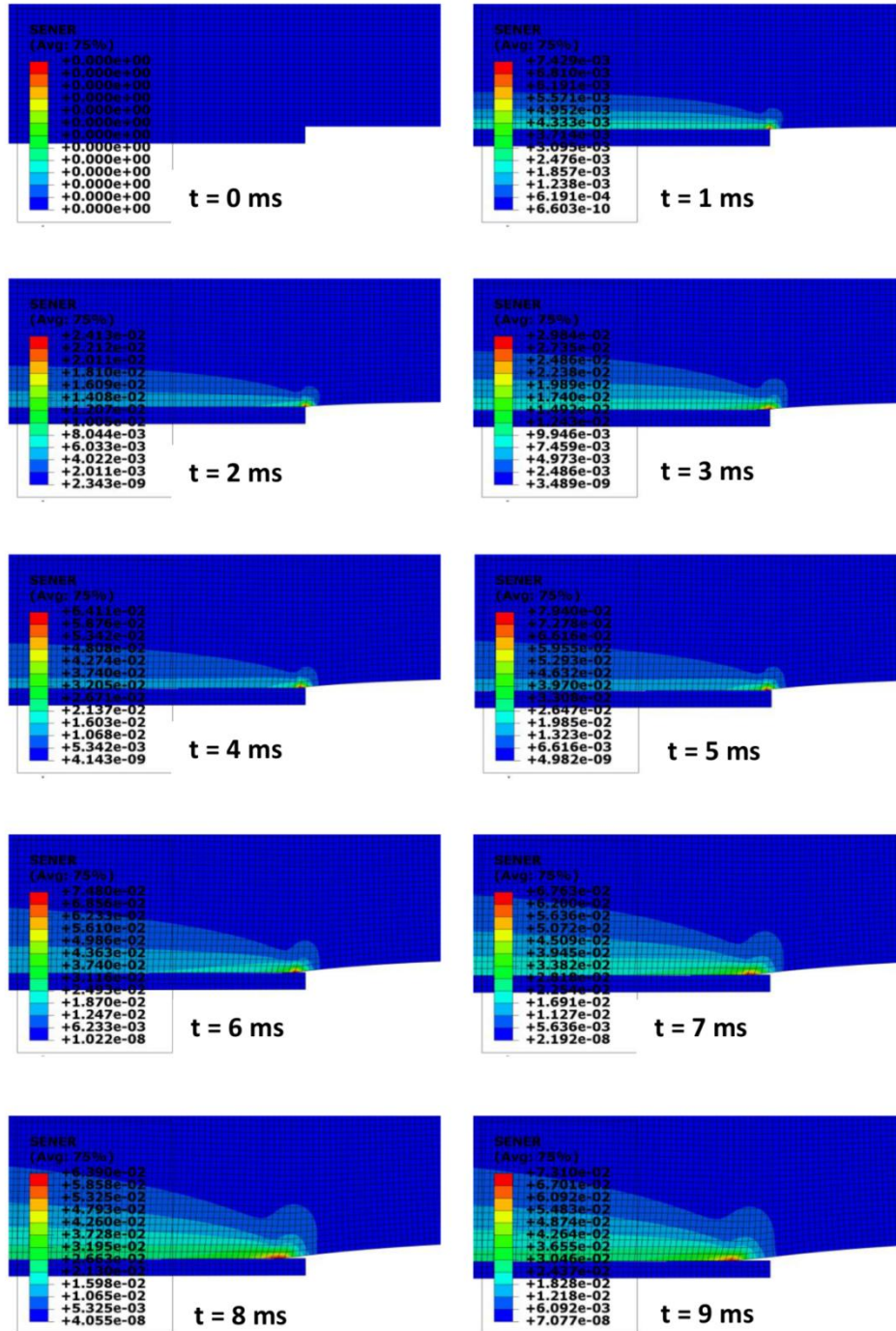
Figure 4.20. CZM model estimates of the strain energy density (mJ/mm³) for the delamination process of 200×200×3 μm ink at 10 A laser current.
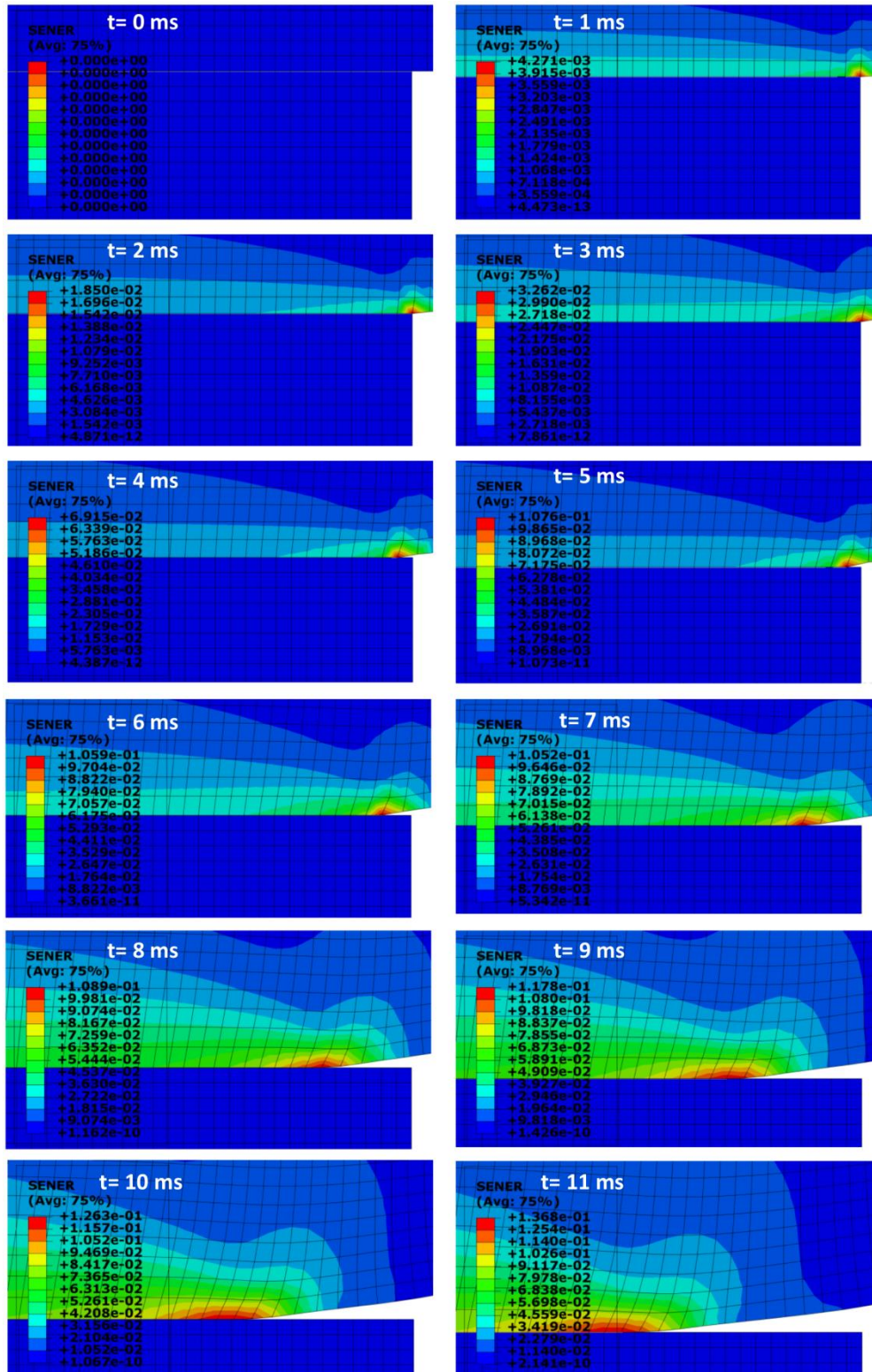
Figure 4.21. CZM model estimates of the strain energy density (mJ/mm³) for the delamination process of 200×200×50 μm ink at 10 A laser current.
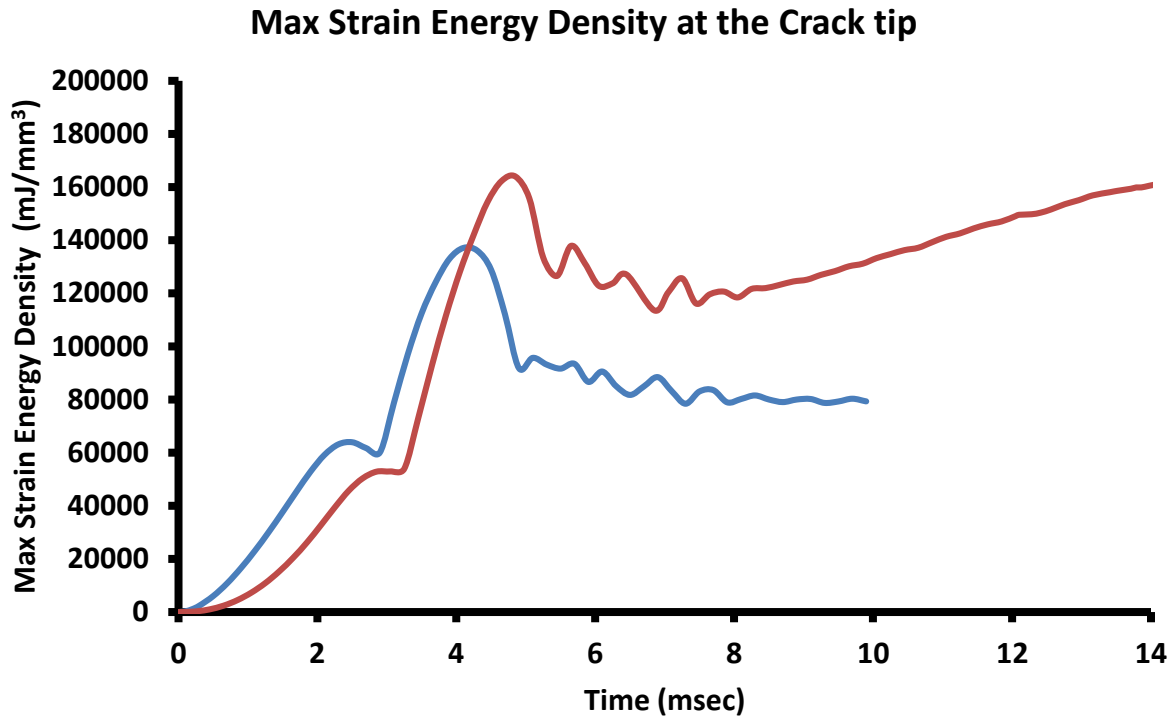
Figure 4.22. CZM model estimates of the strain energy density (mJ/mm³) for the delamination process at 10 A laser current (blue: 200×200×3 μm ink, red: 200×200×50 μm ink).

   The maximum strain energy density for 3 and 50 μm ink thicknesses are shown in Fig. 4.22, where these values peak up to the point where the crack initiated and then drops down once the crack begins to propagate. Further, the CZM shows that the required strain energy to maintain the crack propagation increases after the crack starts propagating for 50 μm ink only. This indicates that the higher the ink thickness, the higher the possibility that the crack propagation stops or reverses direction after it starts propagating (similar to incomplete delamination reported in Section 3.4), if the available strain energy at the crack tip drops below the work of adhesion.

4.7 LMTP Delamination Process Mechanism

Both the linear elastic fracture mechanics and CZM approaches can be used to understand why the delamination process performance is highly dependent on the ink thickness (G_c value is thickness dependent). The results from the decomposition of the strain energy show that thick inks (30 and 50 µm) can develop higher thermal gradient SIFs (see Fig. 4.19) compared with that of thin inks (3 and 10 µm). Therefore, the lower heat rates for thick inks (30 and 50 µm) do not reduce the thermal gradient strain effects. However, the lower heating rates associated with thicker inks might provide lower strain energy rates compared to the ERR required for the delamination propagation because thicker inks require more energy to maintain the crack population compared with thin inks (as shown in Fig. 4.22 for CZM results and justified by the slow crack propagation speeds for thick inks as observed experimentally in Section 4.4.1). Because the fracture mechanics model developed in Section 4.4.2 only simulates the delamination process up to the delamination start point, the model does not account for these effects. Further, comparing the ERRs, SIFs, strains, interface temperatures, and temperature gradients (see Fig. 4.10, 4.11, 4.12, 4.14, and 4.19) at 3.6 msec. time (where the 3 µm start and finish delamination) for 3 µm and 50 µm ink thicknesses, one finds that the there is no difference in the developed strain energy at 10 A current level. However, the high-speed camera shows that only 3 µm ink delaminates, while the 50 µm ink does not show full delamination at this time (3.6 msec.). A possible reason for the delamination of the 3 µm ink thickness is that the ink bends during the LMTP process storing a non-uniform strain energy within in the ink due to its low bending rigidity. This strain energy is released once the delamination process starts helping in the completion of the delamination process. On the other hand, the 50 µm ink does not bend due to its high bending rigidity (4630 times more than that for 3 µm ink). This indicates that the stored strain energy within thin inks helps in building up higher

ERR at the crack tip during the crack propagation to complete the interface delamination, while thick ink's strain energy at the crack tip is mainly supplied through the laser heating (CZM shows higher SED during crack propagation).

Another possible reason that the critical ERR G_c depends on the ink thickness, as reported in Section 4.5; this follows from the fact that heating of the ink-stamp stack system for the same ink thickness at different power levels generates almost the same interface temperature rise that leads to approximately the same ERR at the delamination point. Therefore, the delamination process is dominated by the temperature of the interface. For thick inks (30 and 50 μm), which print at higher temperatures, the work of adhesion between silicon and PDMS may be higher and constant, causing the ERR at the delamination point to be almost the same. For thinner inks, where the delamination temperatures are in the 200 degree C range, the work of adhesion of the interface is still changing and hence, one sees that the ERR at delamination is different for thin inks (ERR at delamination for 3 μm inks is about half of that for 10 μm inks). It is also possible that the higher temperatures encountered for thicker inks result in temperature-dependent changes in the PDMS viscoelastic properties (as described in appendix B). Even though PDMS can withstand such a high temperature rise especially in absence of oxygen with high heating rates, the thermo-mechanical properties of PDMS become temperature-dependent if the temperature rises above 300°C [116] [117], reducing the energy conversion efficiency. Our models, being primarily elastic in nature, do not account for these effects and therefore overestimate the ERR at delamination.

These results from the FEA model, along with huge plastic deformation (see Fig. 4.23) in the PDMS post at the interface edges after printing thick inks, imply that the critical ERR at delamination varies as a function of the PDMS temperature. Further, videos captured using the high-speed camera while printing thick inks, especially 30 μm thickness, show that PDMS stamp

undergoes cyclic deformation around the interface edges during the laser heating. Such cyclic deformation suggests a periodic release (two-to-three times within the delamination time) of the stored energy in the PDMS at a high temperature due to plastic flow before eventually overcoming the interface's work of adhesion, which is also temperature-dependent. Because the model does not account for such plastic flow and temperature-dependent properties of the stamp-ink interface, a higher value for ERR at the delamination point is computed. However, the model should be adequate for estimating the LMTP process behavior for thin inks (i.e. $200 \times 200 \times 3$ μm ink) where the maximum temperature rise is less than 200°C.
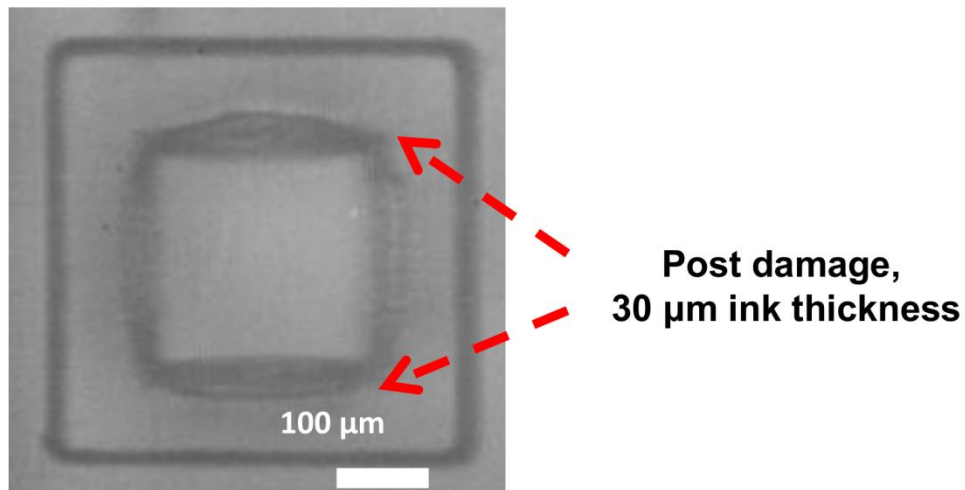
Figure 4.23. PDMS stamp's post damage at the ink-stamp interface after printing $200 \times 200 \times 30$ μm ink at 10 A current.

90

4.8 Summary

In this chapter, a multi-physics model was developed to understand and predict the effects of the multi-physics involved in the LMTP delamination. The modeling is based on decoupling the laser optical absorbance physics from the laser-driven coupled thermo-mechanical physics. Both of the inks' heating rates from the optical absorption model and the delamination times from the high-speed camera are then used as inputs to a coupled thermo-mechanical FEA model. The FEA model was calibrated based on the PDMS post-lateral dimension deformation, which was experimentally measured using a high-speed camera. The model allows for the estimation of the temperatures reached in the ink during the LMTP process. It also identified that the thermal gradient features in the strain field that, in addition to CTE mismatch strain, assist in initiating and driving the delamination process.

The results have shown that the LMTP process is a mixed-mode process in which the critical ERR and SIFs (in both modes) were of equal magnitude for printing the same ink thickness at different laser current levels. However, for printing different inks thicknesses, the critical ERR and SIFs (in both modes) were dependent on the ink thickness (higher for thicker inks). This implies that the LMTP process is more efficient and well understood in the case of printing thin inks ($h_s <$ 10 µm) where the model predictions for delamination time agree with the experimental values. Furthermore, the ERR or SIFs at the edge of the interface where the delamination crack originates, decomposed into two components: one due to CTE mismatch and the other due to the thermal gradients within the PDMS, especially around the edge of the ink.

CHAPTER 5: LMTP PROCESS PERFORMANCE

5.1 Introduction

The work in Chapter 3 and Chapter 4 on the LMTP process focused on experimentally and computationally characterizing the effects of transferred ink sizes and thicknesses, and laser beam powers on the laser-driven delamination process mechanism. The conducted research shows that printing thick silicon inks using LMTP involves high energy and interfacial temperature requirements suggesting the process is more suitable and well-understood in printing thin inks ($0.8 \leq h_s \leq 10$ μm). Furthermore, the axisymmetric thermo-mechanical model predictions for the delamination times based on Griffith's criterion in printing inks with $h_s = 3$ μm thicknesses at different powers was found to match the measured delamination times (estimation error $\leq 10\%$). In this chapter, several studies are conducted to understand the effects of other process parameters such as stamp post dimensions (size and height), ink-stamp alignment, PDMS formulation for the stamp, and the shape of the transferred silicon inks on the LMTP performance and mechanism at ink thicknesses $h_s = 3$ μm. The effects of these parameters on the delamination process performance are measured by the delamination times from the high-speed camera experiments and/or the model's predictions of delamination times based on the ERRs. Further, the model predictions for the SIFs and the interface temperatures are evaluated. This chapter, along with previous studies, should help LMTP users to understand the effects of the process parameters on the process performance in order to select optimal operation conditions.

5.2 Stamp Post Dimension Effect

In this section, the effect of changing the stamp post dimensions (h_p and L_p shown in Fig. 5.1) are investigated using the previously discussed FEA model and high-speed camera experiments.

Because the selection of the post size depends on the size of the ink, a dimensionless number $R = L_p/L_s$ is defined to indicate the size of the post relative to the ink size (where post size equals the ink size at $R = 1$, the post is larger than the ink if $R > 1$, the post is smaller than the ink if $R < 1$). Figure 5.2-a shows the ERRs estimated from the model for different R values when printing 200×200×3 µm square ink at 10 A current level. The results show that when $R = 1$, the ERR builds up at the ink-stamp interface edges for the same laser pulse power is lower than the ERRs when $R \neq 1$ cases as a function of the laser pulsing time. This indicates that the delamination times should be higher at $R = 1$ (estimated to be 5.7 msec. from the model based on 0.1 J/m² work of adhesion of Si-PDMS interface). Further, the ERRs when $R > 1$ cases (post larger case) are, in general, independent of the values of R. The results also show that for $R < 1$ cases, the ERRs are higher for smaller R values, indicating that the delamination time should be lower at smaller R, when $R < 1$. Figure 5.2-b indicates that the interface temperature rise is higher for smaller R when $R \leq 1$, but when $R > 1$, the temperature rise becomes independent of the R value. This follows from the fact that the ink heating rates of the same ink dimensions at different R values are the same when $R > 1$. However, when $R < 1$, the contact area at the interface is reduced leading to higher thermal energy storage in the silicon inks at lower R values. The difference in the temperature rise between $R > 1$ and $R = 1$ cases follows from the fact that at $R = 1$, there is no lateral heat transfers (the same
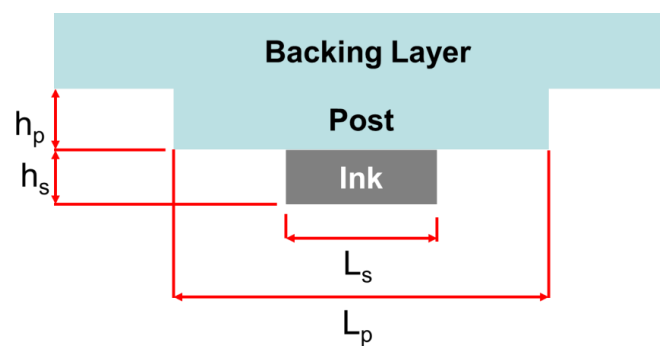
Figure 5.1. Ink-stamp system's dimensions.

post and ink sizes) that leads to greater thermal energy storage in the ink; hence, it increases the temperature rise rate. Therefore, when $R \leq 1$, the thermal stresses are only generated by the CTE mismatch strains (the temperature gradients occur only in the axial direction, where the PDMS expansion is not constrained). The SIF values for opening and shear modes as a function of pulse time at different R values are shown in Fig. 5.2-c and 5.2-d. The results show that the SIFs, in both fracture modes, flip directions when the R value changes from $R \leq 1$ to $R > 1$. The direction change in the SIF suggests that the generated strains close the interface (in opening mode) when $R \leq 1$, while they open the interface when $R > 1$. Furthermore, it indicates that the strains (in shear mode) at the crack tip stretch the interface away from the interface center when $R \leq 1$, but they squeeze the interface at the crack tip toward the interface center when $R > 1$. For values of $R > 1$, the SIFs in both directions are independent of R value. For $R < 1$, the absolute value of the SIFs decrease with the increase of R and is lowest at $R = 1$.

Figure 5.3 shows estimates of the delamination times using the ERRs from the model, compared with the delamination times obtained from high-speed camera experiments (three experimental trials at each R value). The results show good agreement between the model estimates and the experimental results for $R > 1$; however, at $R < 1$, the model overestimates the delamination times (delamination time experimentally are 2.1 msec. and 1.4 msec. for $R = 0.75$ and $R = 0.5$, respectively). Although, for $R < 1$ values the delamination occurs at lower delamination times compared to $R > 1$, the interface temperatures at the delamination point are higher at $R < 1$ (285 ºC and 245 ºC for $R = 0.75$ and $R = 0.5$, respectively) compared to the interface temperatures at $R > 1$ (198 ºC at any R value). Therefore, model estimations at $R < 1$ are more temperature-dependent due to the thermo-mechanical and the interface temperature-dependent work of adhesion and properties as suggested in Section 4.7. Printing at $R < 1$ values reduces the delamination time and

the energy required for the delamination, but it increases the interface temperature (not preferable). Further, experiments show that printing without stamp post ($R \rightarrow \infty$) shows no significant difference compared to printing with stamp post at $R = 2$ value. The discrepancy between the model estimation and the experimental delamination time at the $R = 1$ value can be justified by the misalignment effect, as will be described in Section 5.3.
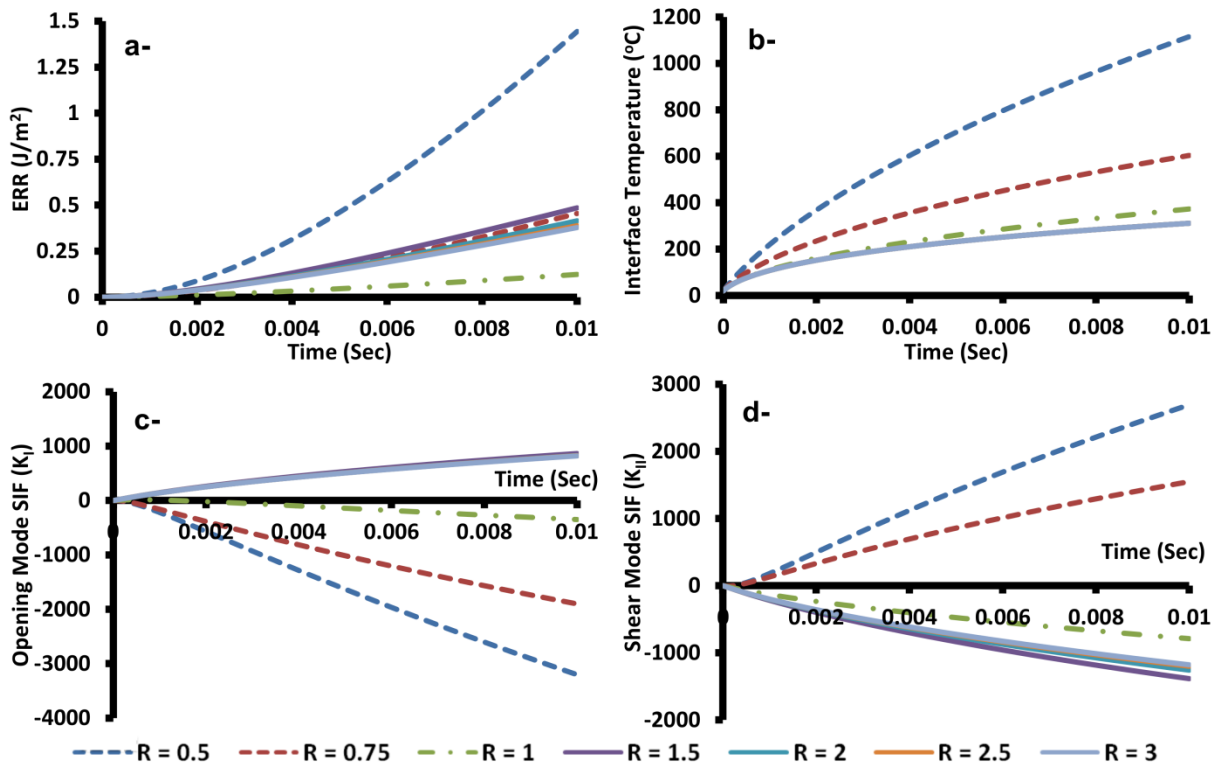
Figure 5.2. FEA model predictions for printing 200×200×3 μm inks at different R values at 10 A current level, (a) ERRs, (b) Interface temperatures, (c) SIFs in opening mode (K_I), and (d) SIFs in shear mode (K_{II}). (In general, curves overlap when $R > 1$).
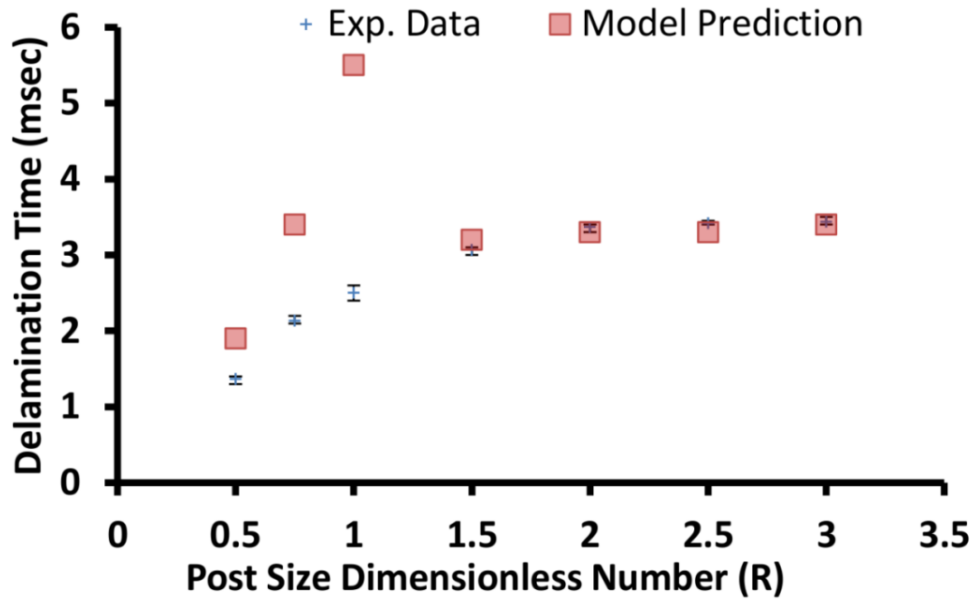
Figure 5.3. Model estimations for the delamination time at different *R* values based on 0.1 J/m² work of adhesion compared with the experimental values (three trials).

R = 0.5
Max. 285 °C

R = 1
Max. 212 °C

R = 2
Max. 198 °C

Supportive Elements
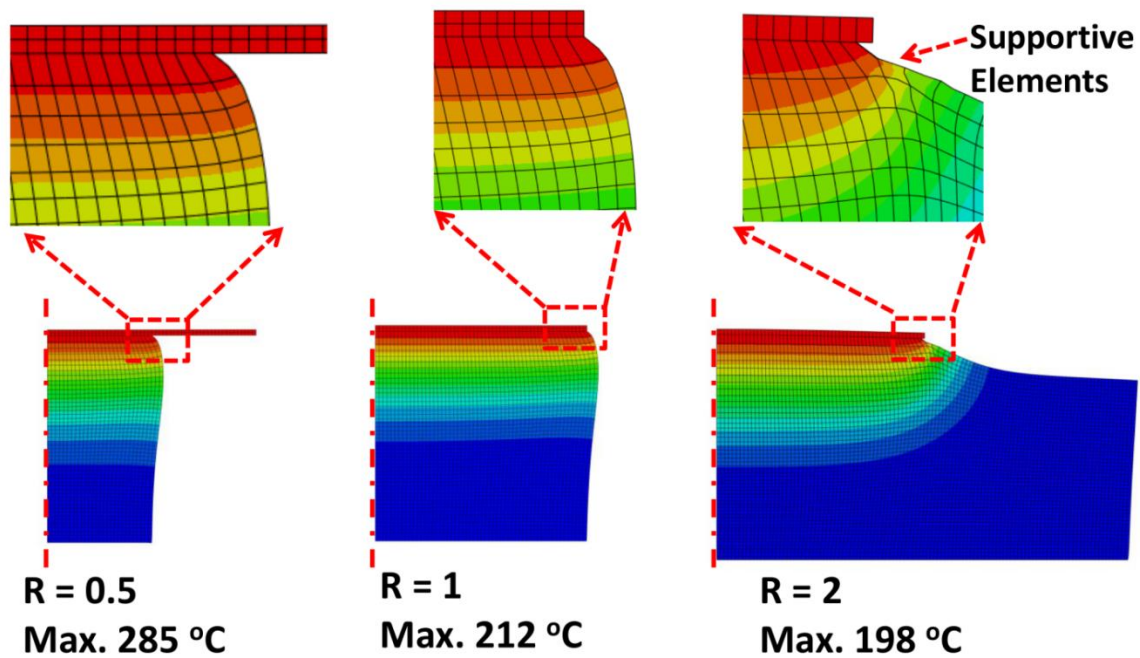
Figure 5.4. Axisymmetric model estimation for the temperature field of the deformed ink-stamp stack at the delamination points measured experimentally for different *R*.
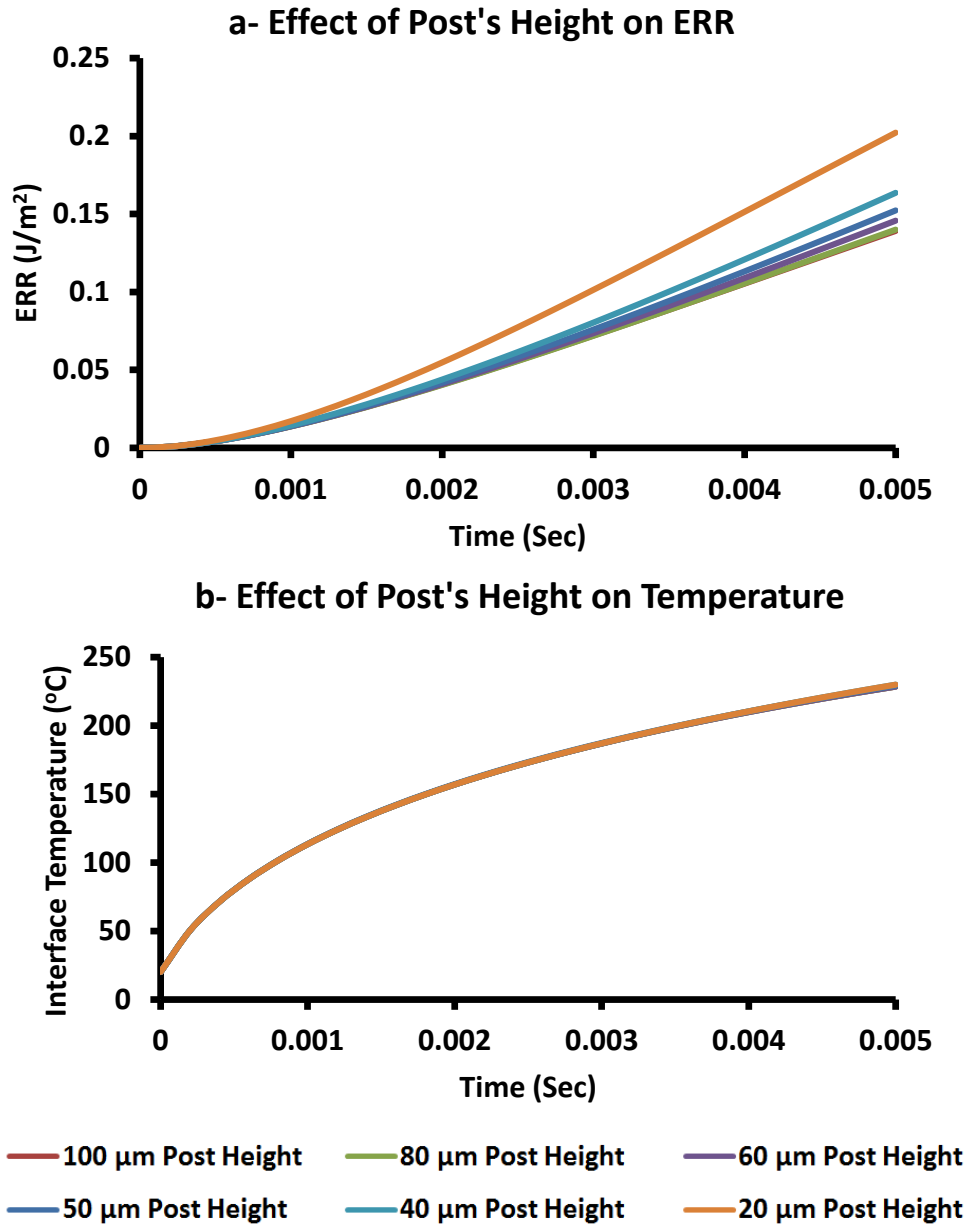
Figure 5.5. Model estimations for the thermo-mechanical delamination process performance at different post heights, (a) effect on the ERR (80 μm and 100 μm curves overlap), and (b) effect on the interface temperature (all curves overlap).

Figure 5.4 shows the deformed stack shape from the axisymmetric model at the delamination point. The figure shows that for $R \leq 1$, where there is no supportive PDMS side at crack tip, the PDMS elements at the crack tip tend to rotate and change the direction of the thermal load

generated by the thermal strains, which explains the changes in the SIF's direction based on the R value. However, if $R > 1$, the supportive PDMS side's elements prevent this rotation reducing the effect of the CTE mismatch strains and adding additional thermal strains due to the thermal gradients within the PDMS post. Both the experiments and the FEA model results show that the stamp post height has no effect on the LMTP printing. However, the model does not account for modeling the PDMS backing layer (~1 mm thickness). Therefore, the effect of the post height (h_p) (equivalent to print with a post without the backing layer) is investigated as shown in Fig. 5.5. The results show that the post height has no effect on the LMTP process, evaluated by the ERR in Fig. 5.5-a, in printing 200×200×3 μm inks if $h_p > 50$ μm, while h_p has no effect on the temperature rise during the LMTP process (see Fig. 5.5-b).

5.3 Ink-Stamp Misalignment Effect

The large discrepancy between the model estimations and experimental values of the delamination time at $R = 1$ values, motivated the study of the ink-stamp misalignment effect on the LMTP process performance. Figure 5.6-a shows the ERRs collected at the two misaligned interface sides. The side where the post is slightly larger than the ink, and is referred to as "post larger," and the other side where the post is slightly smaller than the ink, is referred to as "post smaller." The results show that the ERRs at any misalignment on both sides (post larger or post smaller) are always higher than the ERR with no misalignment at $R = 1$ value. Further, for a given misalignment value within ± 5 μm, the ERR at the post larger side is always higher and more sensitive to a misalignment value than the one at the post smaller side due to the absence of thermal gradient strains. Furthermore, the ERR build up at the crack tip is higher for larger misalignment values at a given time on both sides. The huge difference in the rates at which the ERR builds up at the crack tip due to smallest value of misalignment (± 1 μm) shows that the misalignment effect,

which always occurs, due to the fabrication and positioning inaccuracies, could be the main reason why the model overestimates the delamination time at $R = 1$. Based on the model estimations for the ERRs, a small amount of misalignment ($\pm$ 5 µm) is found to be insignificant if $R \neq 1$ (i.e. Fig. 5.7 where misalignment of $\pm$ 50 µm has no effect of the ERR at $R = 2$). Figure 5.6-b shows the interface temperature for the larger and smaller post sides at different misalignment values. The results show that the larger side of the post always has lower interfacial temperature rise rates compared to the smaller side of the post due to the lateral heat transfer. This generates thermal gradients at the larger side of the post only. Figures 5.6-c and 5.6-d show the SIFs buildup at the crack tip in the opening and the shear modes, respectively, at different misalignment values. In opening mode at any given time, the K_I values at the post larger side are constant for different misalignment values. Further, they are lower, in value, at the post smaller side, where the K_I rates are more sensitive to misalignment values. In the shear mode, the K_{II} rates at the post smaller side are constant for different misalignment values and lower, in value, at the post larger side, where the K_{II} rates are more sensitive to misalignment values. The differences in SIFs, in both fracture mode values at the post's larger and smaller sides for a given misalignment suggest unbalanced energy release at different sides, which causes ink rotation observed during printing on a receiving substrate that is 500 µm away from the post. These results (ERRs, interface temperatures, and SIFs at $R = 1$) are difficult to verify experimentally because it is difficult to fabricate a SU8 mold with $\pm$ 1 µm resolution for molding the PDMS stamp or achieving position accuracy less than $\pm$ 2 µm (limited by the CCD camera resolution). However, the uncertaninty band in the expermintally observed delmination times for $R =1$ is twice that when $R \neq 1$ (see Fig. 5.3). Further, this indicates that besides the misalignment effects in printing at $R =1$, the singularity at the interface edges makes the model ERR estimations inaccurate.
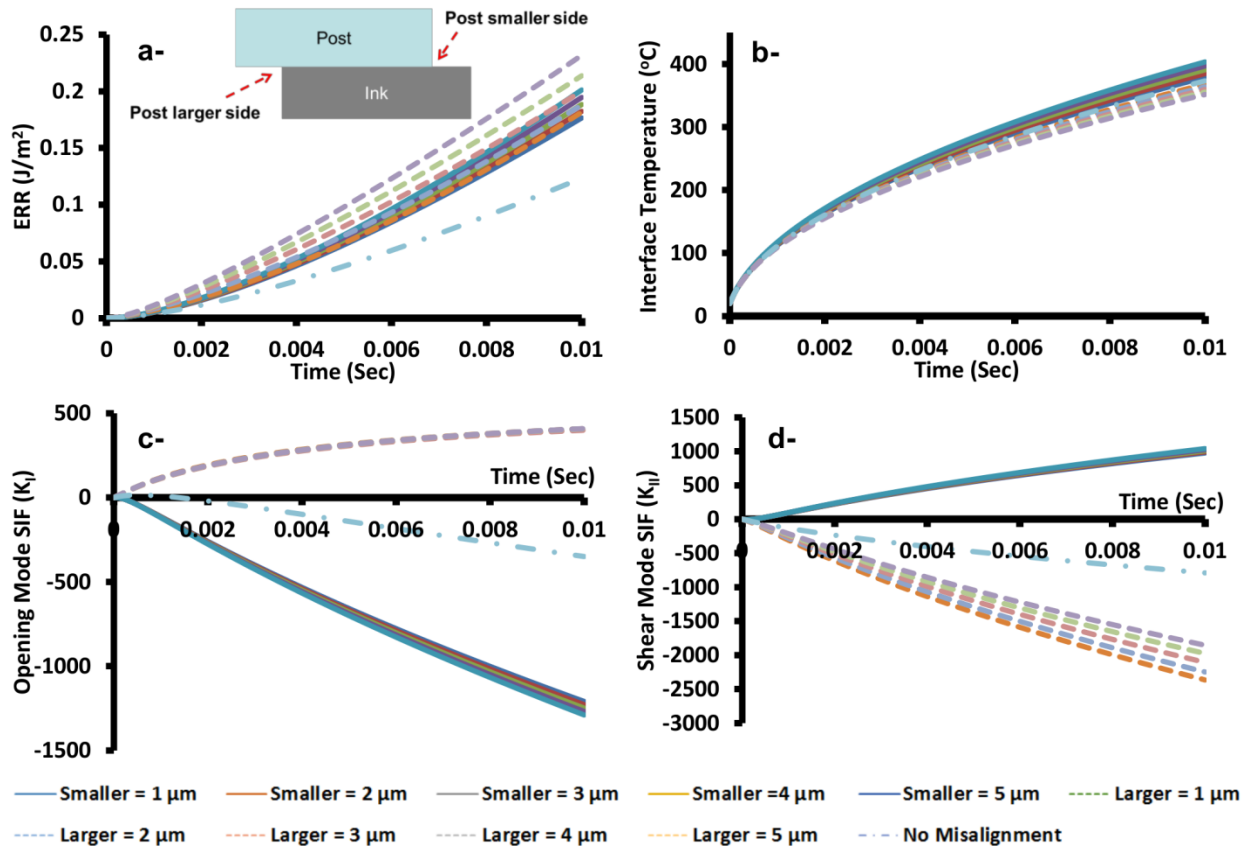
Figure 5.6. Model predictions for printing at $R = 1$ with ± 5 μm misalignment values at 10 A current level, (a) ERRs, (b) Interface temperatures, (c) SIFs in opening mode (K_I), and (d) SIFs in shear mode (K_{II}).
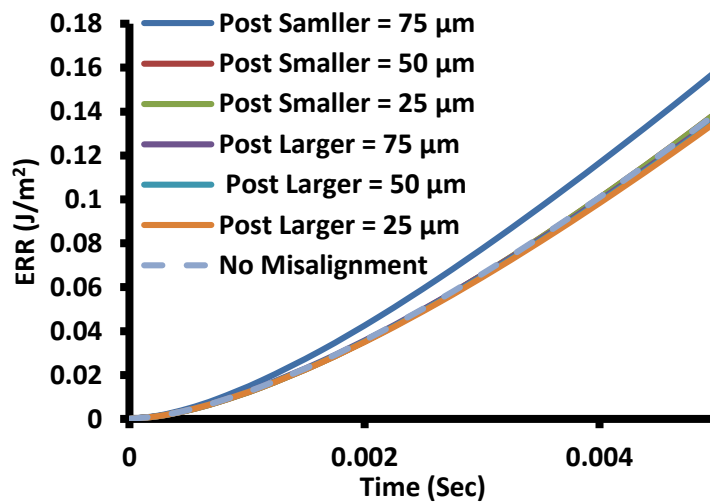
Figure 5.7. Model predictions for printing at $R = 2$ with ± 75 μm misalignment values at 10 A current level (all curves overlap except post smaller side at 75 μm misalignment).

5.4 Stamp PDMS Material Effect

Due to its fabrication simplicity, transparency, viscoelasticity, and dry adhesion capability, PDMS is a suitable stamp material choice in transfer printing technology. In the LMTP process, the large CTE and the low thermal conductivity make the PDMS a suitable candidate for inducing thermal stress at the ink-stamp interface as described in Section 4.5. Therefore, in this section, different PDMS formulations with varying mechanical properties (mainly Young's modulus) are used to print $200 \times 200 \times 3$ µm square silicon inks. Assuming that, except for Young's modulus, the thermo-mechanical properties of PDMS are independent of its formulation, one can estimate the ERRs from the FEA model for printing with stamps with different Young's modulus values as
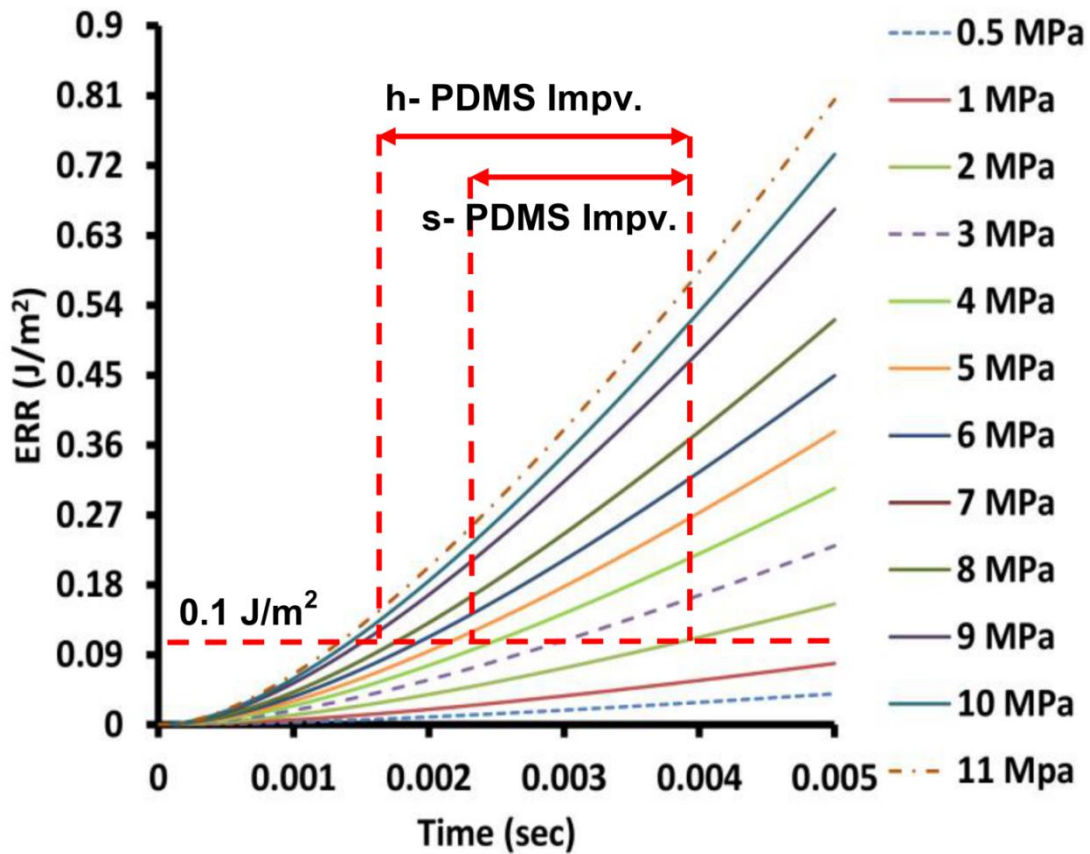
Figure 5.8. Model predictions for the effect of PDMS stamp stiffness on the ERR.

101

shown in Fig. 5.8. The model results show that the higher the Young's modulus of the PDMS, the higher the ERR buildup at the crack tip at any given time. Therefore, increasing the Young's modulus of the PDMS should increase the thermo-mechanical energy conversion efficiency to print at lower delamination times and energies. Because 1:10 PDMS mixing ratio by weight is the standard mixing ratio for soft-PDMS (s-PDMS, Sylgard 184 by Dow Corning), which was used in all previous LMTP experiments, 1:3 and 1:5 PDMS mixing ratios should improve the delamination time by ~1.6 msec. and ~1 msec., respectively, when printing with 10 A laser diode current and assuming 0.1 J/m^2 work of adhesion for Si-PDMS interface [2] [102]. Figure 5.9-a shows the experimental results for printing with different s-PDMS mixing ratios (1:3, 1:5, and 1:10 by weight, equivalent to Young's modulus of ~5, 3.5, 2 MPa, respectively). The results show that printing using different PDMS mixing ratios does not improve the LMTP process performance as estimated from the model. A possible reason for this is the PDMS thermo-mechanical properties are temperature-dependent. Further, the other thermo-mechanical properties (mainly the CTE) are dependent on the mixing ratio, decreasing the actual ERR buildup at the crack tip during printing. Hard-PDMS stamps (h-PDMS; (3.4g of poly(7-8% vinylmethylsiloxane)-(dimethylsiloxane), 100mg of (1,3,5,7-tetravinyl-1,3,5,7-tetramethylcyclotetrasiloxane), 50mg of platinum catalyst, and 1g poly(25-30% methylhydrosiloxane)-(dimethylsiloxane)); reported in [118] to have 9 MPa Young's modulus) with patterned post ($R = 2$) is also used to print 200×200×3 µm silicon inks at 10 A laser current. The results show (Fig. 5.9-b) a slight improvement (less by 0.9 msce.) over printing with s-PDMS (1:10) stamp at 10 A current. However, it is far less than the estimated improvement from the model (2.6 msec. assuming 0.1 J/m^2 work of adhesion of Si-PDMS interface [2] [102]) possibly because of the same reasons given before in printing PDMS at different mixing ratios.
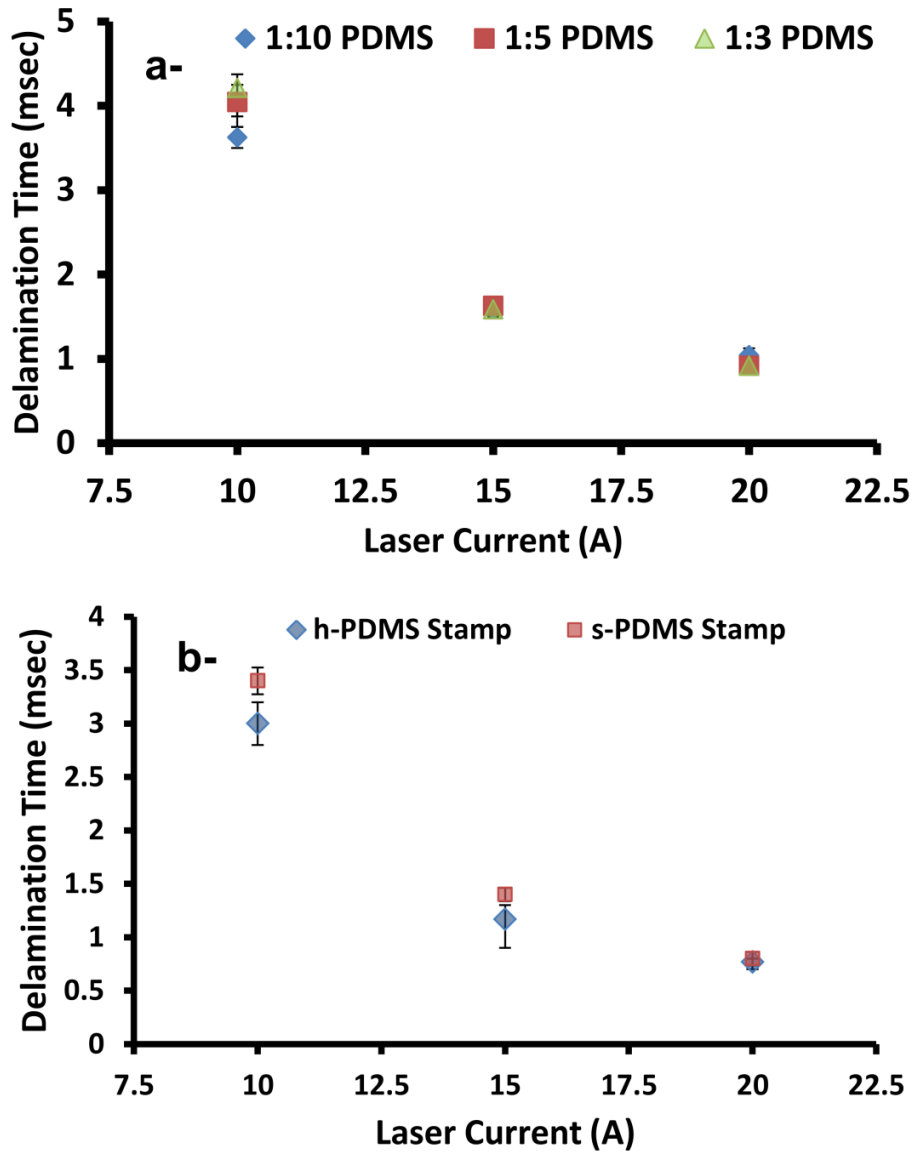
Figure 5.9. Effect of PDMS formulation on the experimental delamination time (three trials), (a) different s-PDMS mixing ratios, and (b) h-PDMS vs. s-PDMS (1:10 ratio).

5.5 Ink Shape Effects

The previous studies extensively investigate the LMTP process for different effects while printing square silicon inks with different dimensions. Therefore, the focus in this section is on printing four different silicon ink shapes (200×200 µm square, 200×200-100×100 µm annular-square, 225 µm diameter round, and 225-112.5 µm diameter annular-round as shown in Fig. 5.10)

with 3 µm thickness using a stamp post of similar shapes (i.e. round stamp post for round inks) with $R = 2$ value. Axisymmetric FEA models are used to evaluate the LMTP process performance in printing the round inks, while the 3D models are used to evaluate square inks to account for the corner effects. For the annular inks, both round and square, both models (axisymmetric and 3D) evaluate the ERR at two cracks: one at the external interface's edge, and the other at the internal interface's edge (see in Fig. 5.10-b and 5.10-d). Figures 5.11-a, 5.11-b, and 5.11-c compare the ERRs evaluated for printing both round and annular-round inks, at the internal and the external edges, using 10, 15, and 20 A current levels, respectively. For all laser current levels, the results show that printing round inks build up higher ERR at the interface's edge compared with annular-round inks at both interfaces' edges (internal and external).
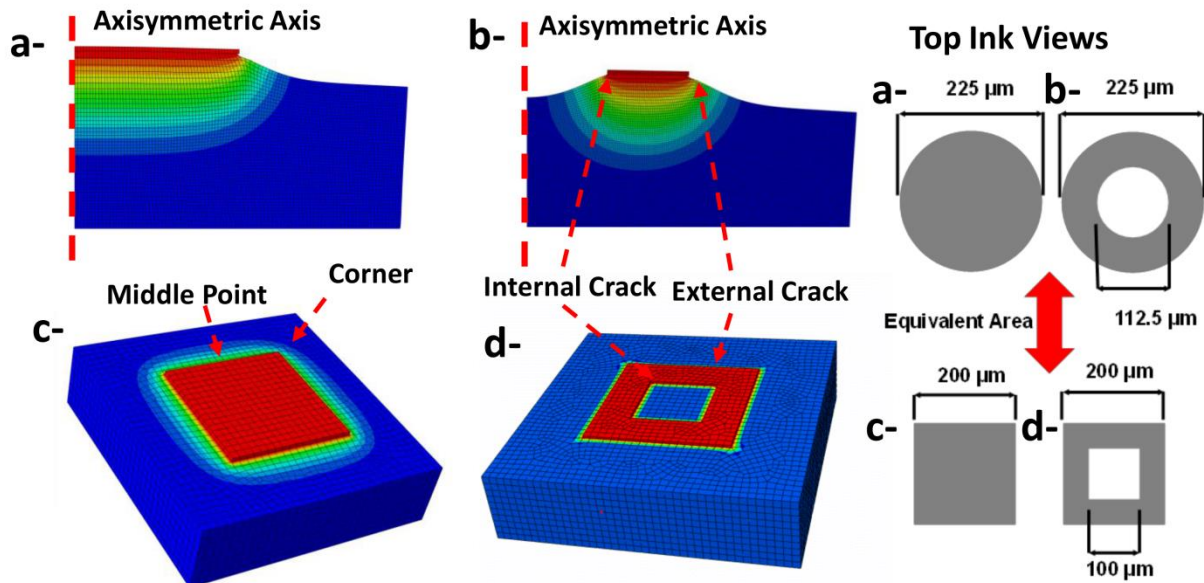
Figure 5.10. Models to print different ink shapes, (a) round ink using axisymmetric model, (b) annular-round ink using axisymmetric model, (c) square ink using 3D model, and (d) annular-square ink using 3D model.
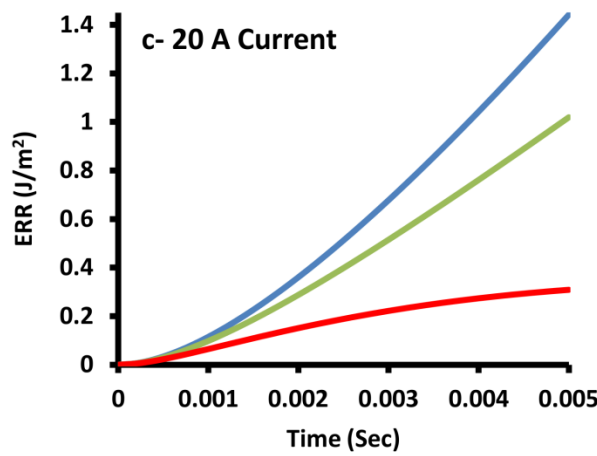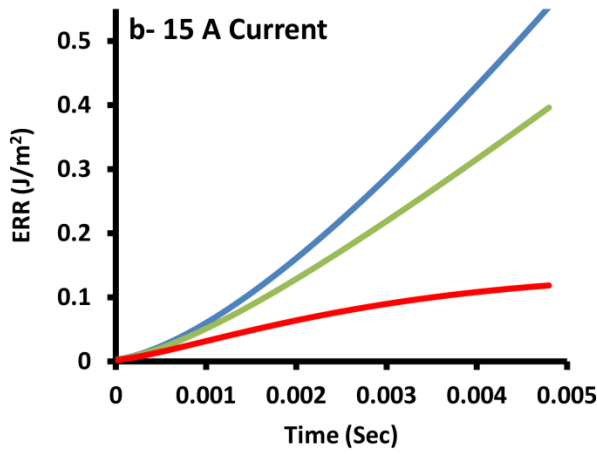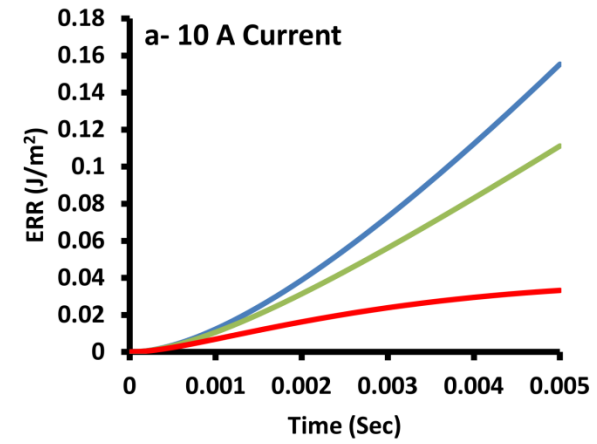
Figure 5.11. Model predictions for the ERR results for printing round inks (both solid and annular) at the external and internal (for annular only) crack tips, (a) 10 A, (b) 15 A, and (c) 20 A.

Therefore, the delamination time should be less for printing round solid inks especially at 10 A power level (the difference between the round and annular-round-external case curves assuming 0.1 J/m^2 work of adhesion [2] [102] is the largest at 10 A). For printing annular-round inks, the delamination process begins at the external interface's edge due to the higher ERR buildup at the external interface's cracks. These results have been verified using high-speed camera measurements of the delamination time where round inks print at lower times compared with annular-round inks (see Fig. 5.12) and the delamination process of annular-round inks always starts at the external edge. Further, for all laser current levels, printing round inks usually generates higher interface temperatures compared with annular-round inks (see Fig. 5.13) because heat transfer within the PDMS in the lateral direction occurs at the two interface edges (internal and external, see Fig. 5.10-b), reducing the thermal energy stored in the ink.
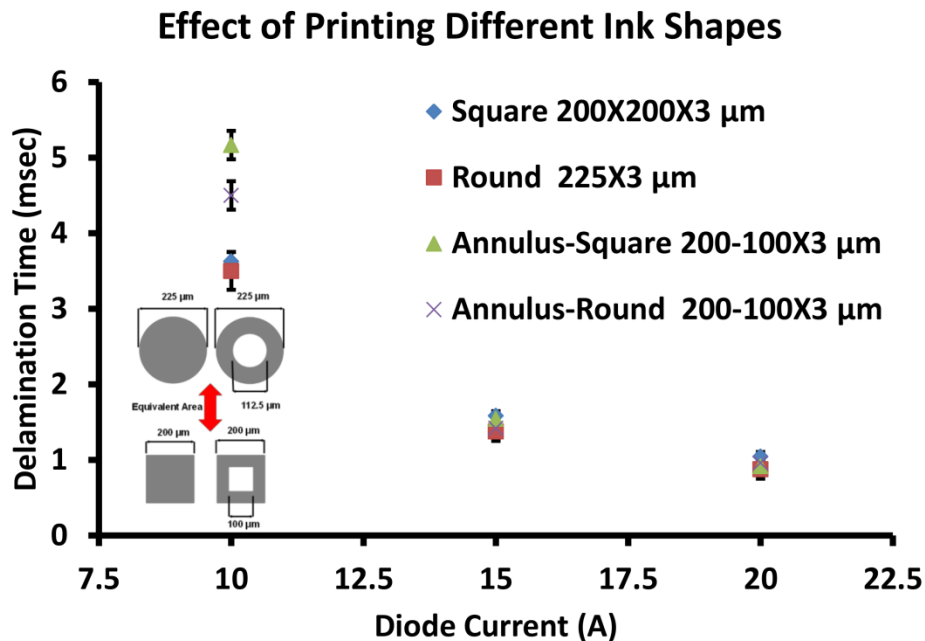
Figure 5.12. Experimental results of the delamination time in printing different ink shapes (three trials).

For printing square inks, the 3D model estimations for the ERRs at the external interface edge (energy buildup at the internal edge is not dominant in the process) are shown in Fig. 5.14-a, 5.14-b, and 5.14-c for printing at 10, 15, and 20 A currents. The results indicate that the ERR buildup at the external edge for printing solid square inks is higher than that for printing annular-square inks at all laser current levels. Therefore, printing solid square inks should take less time compared to annular-square inks especially at 10 A current level (the difference between the square and annular-square curves at the interface's edge mid-point at 0.1 J/m^2 work of adhesion is the largest at 10 A). The experimental results in Fig. 5.12 verify the model estimates where annular inks take less time to print especially for 10 A current level. Because the ERR in printing round inks is always higher than that in printing square inks at the interface edge mid-point (see Fig. 4.8-d), round inks usually print at lower delamination times.
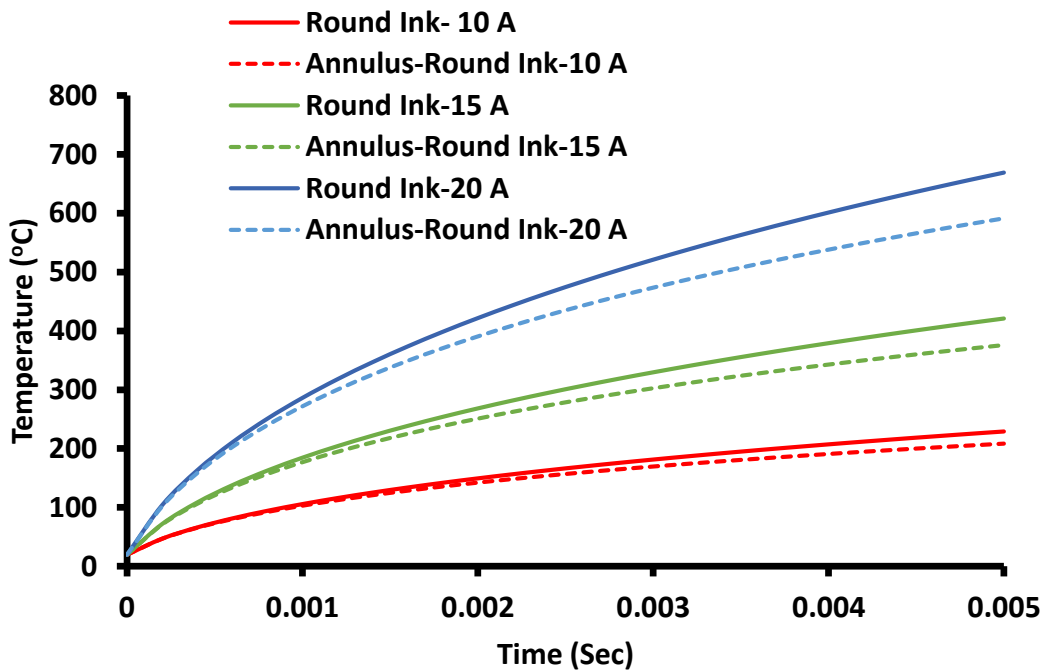
Figure 5.13. Model predictions for the interface temperature rise in printing round ink vs. annular-round inks at different laser current levels.
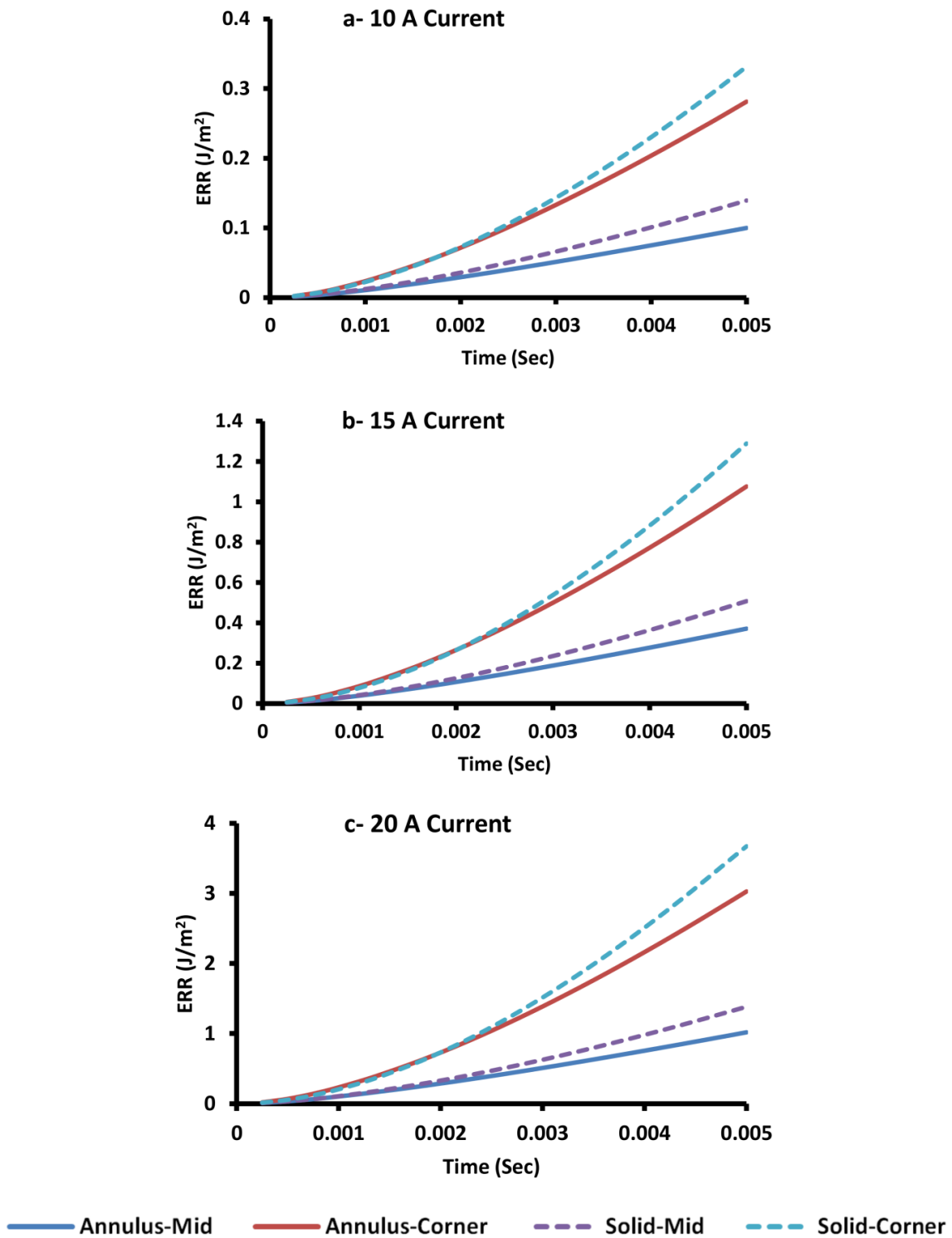
Figure 5.14. Model predictions for the ERR results for printing square inks (both solid and annular) at the crack tip on the corner and the edge mid-point, (a) 10 A, (b) 15 A, and (c) 20 A.

5.6 Summary

In this chapter, many studies have been conducted to investigate the effect of the stamp post dimensions, the effect of ink-stamp misalignment, the effect of different PDMS formulations, and the effect of the ink shape on the LMTP process performance and mechanism. The effects of modifying these parameters are explored using FEA model estimations and experimental measurements. The results indicate that printing with different post sizes affects the temperature distribution of the ink-stamp system leading to different process performance. Therefore, printing with a stamp post that has a lateral dimension ratio $R > 1.5$ value is always preferable to improve the printing accuracy and performance. Further, printing with h-PDMS stamps might reduce the LMTP delamination time over printing s-PDMS. However, s-PDMS is still preferable due to its simplicity with fabrication and its reliability during printing (h-PDMS is brittle and easily fractured or broken). In case of printing different ink shapes, even though at a given time annular inks usually have lower interface temperature compared to solid inks, the interface temperature at the delamination point is usually less for solid inks.

CHAPTER 6: PATTERNED STAMP DESIGN

6.1 Introduction

The studies in Chapter 3 and Chapter 4 focus on developing an experimental approach to characterize the delamination using high-speed camera recordings, and modeling the opto-thermo-mechanical delamination process. The results indicate that the delamination process is a mixed-mode fracture process (both shear loading mode along the interface and opening mode normal to the interface are significant). Further, the shear mode loading contribution in building up stain energy at the interface edges is two times higher than that for the opening mode (as described in Section 4.5). Given the fact that the work of adhesion in opening mode is higher than that in shear mode, enhancing the opening mode loading during printing is essential to optimize and improve the LMTP process performance. Furthermore, decomposition of the thermal strains, in both fracture modes, from CTE mismatch effects and from thermal gradients showed that these two components (CTE mismatch and thermal gradients) act in the same direction in the opening mode while they act in the opposite direction in the shear mode. This indicates that enhancing the opening mode loading, which can be achieved by engineering the stamp design, is more effective for optimizing the process performance. Therefore, to achieve that, different patterned stamp designs are proposed:

> ➤ **Cavity stamp** (see Fig. 6.1-a): A cavity, smaller than the size of the ink, is patterned at the interface to entrap a thin air-layer during the ink pickup. This air layer generates thermally-induced air pressure within the cavity pushing the ink away from the stamp, enhancing the opening mode loading.
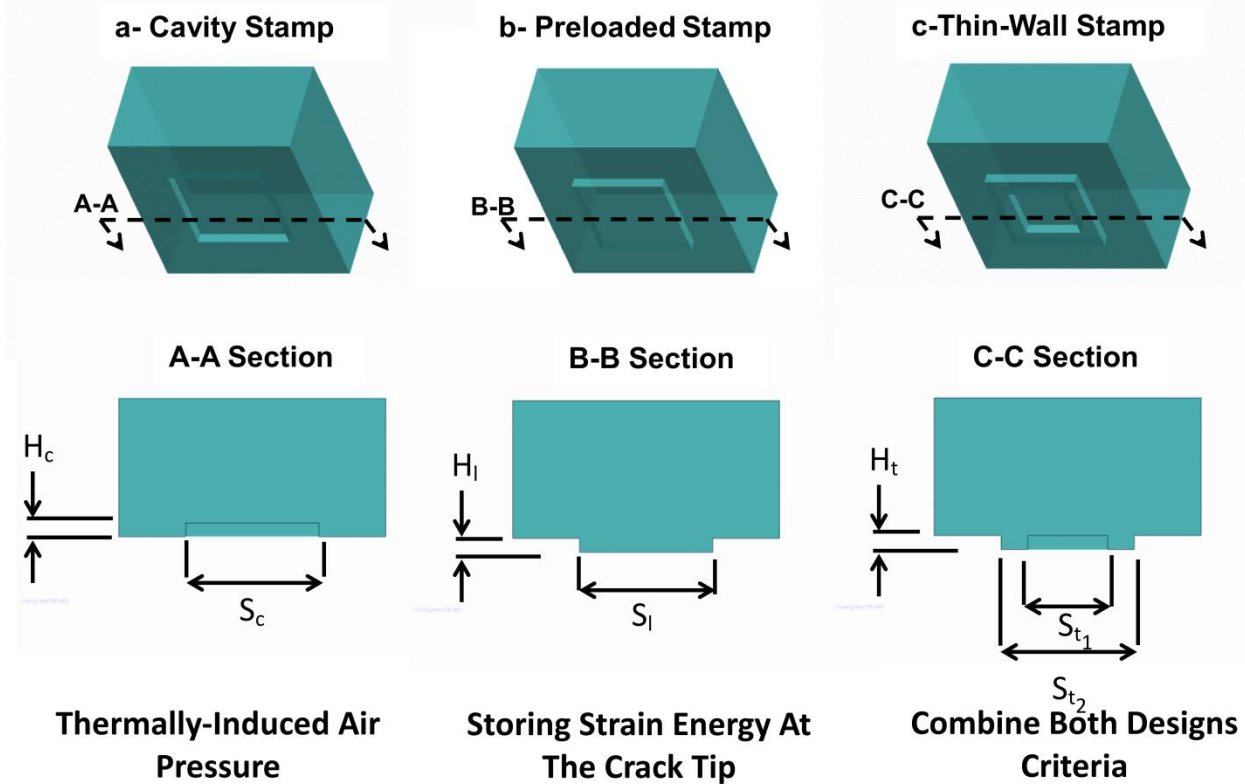
Figure 6.1. Suggested patterned stamps to enhance the process performance, (a) cavity stamps, (b) preloaded stamps, and (c) thin-wall stamps.

➤ **Preloaded stamp** (see Fig. 6.1-b): A step, smaller than the ink, is patterned at the interface to collapse during the ink pickup. The collapsed step feature stores strain energy at the interface pushing the ink away from the stamp, enhancing the opening mode loading.

➤ **Thin-wall stamp** (see Fig. 6.1-c): Both cavity and preloaded stamp designs are combined.

To achieve the design goals (printing at lower laser beam pulse duration, lower energy, and lower temperature), the dimensions of the proposed patterned stamps have to be designed to optimize the LMTP performance. The rest of the paper will discuss how a CZM approach is used to evaluate the proposed stamps performances during both the ink pickup and LMTP printing. A FEA CZM model is chosen because it has the capability to model the progressive nature of delamination showing the ink-stamp separation. Further, the model results, for pickup and printing,

111

are experimentally verified by determining the critical dimensions for the patterned stamps to collapse during ink pickup, and measuring the delamination time.

6.2 Cavity Stamps

In this section, the design procedure to optimize the cavity stamp dimensions and their effect on the LMTP process performance are discussed and verified experimentally.

6.2.1 Cavity Stamp Design for Pickup

A 2D FEA model has been developed using ABAQUS® (ABAQUS, Inc.) to predict the cavity stamp performance during ink pickup by defining a cohesive interface at the ink-stamp interface. The pickup model, similar to the real ink pick-up process, has two steps:

➢ A static preloading step (i.e. see Fig. 6.2-a and Fig. 6.2-c for no-sagging and sagging pickup, respectively) to solve for the deformed equilibrium shape of the ink-stamp during stamp engagement into the donor substrate (two fixed displacement boundary conditions are imposed at the end of the stamp and the ink); and,

➢ A CZM relaxation step (i.e. see Fig. 6.2-b and Fig. 6.2-d for no-sagging and sagging pickup, respectively) to predict the delamination driven by the stored strain energy at the ink-stamp interface due to the pattern collapse (the fixed boundary condition at the ink end is released allowing the interface to delaminate).

A stamp height of $h_p = 200$ μm is assumed, which is based on previous results from Chapter 4 that show that the changes in the thermo-mechanical fields are localized around the interface (< 50 μm). Further, 1 μm element mesh size is enforced at the ink-stamp interface to achieve higher numerical solution accuracy. The pick-up model predicts the performance of the cavity stamps at the end of the pick-up process to determine the stamp sagging (i.e. Fig. 6.2-b for no-sagging and Fig. 6.2-d for sagging). Fig. 6.2-e and 6.2-f show the generated strains in the opening and shear

modes due to ink sagging (no-sagging case has no strain energy stored at the interface). The results

indicate that in case of pickup with the sagged-cavity stamp, compressive stresses are generated at

the crack tip that could lead to suspend the tensile stresses in the opening mode that are generated
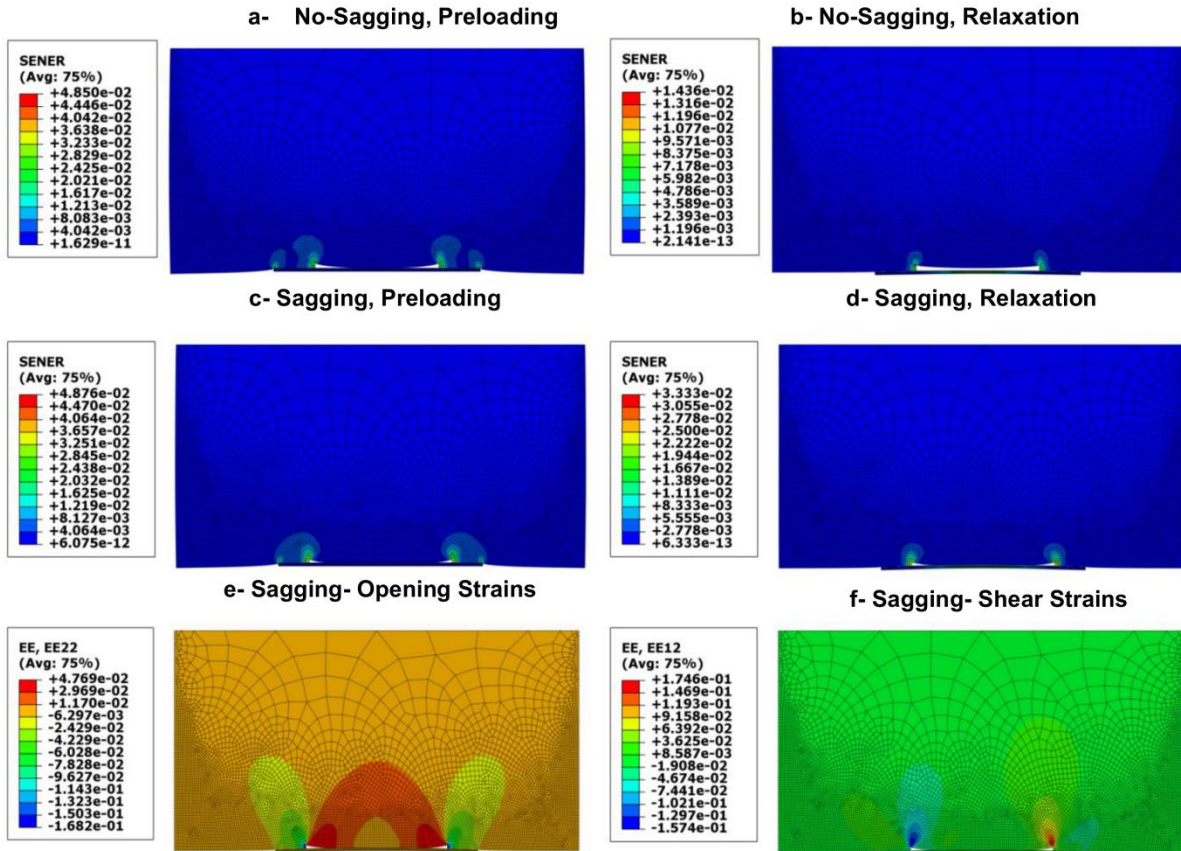
Figure 6.2. 2D CZM model results for 200×200×3 μm silicon ink pick up using cavity stamps, (a) strain energy density (mJ/mm³) at the end of preloading step for the no-sagging case where S_c = 140 μm, H_c = 5 μm, b) strain energy density (mJ/mm³) at the end of relaxation step for the no-sagging case where S_c = 140 μm, H_c = 5 μm, (c) strain energy density (mJ/mm³) at the end of preloading step for the sagging case where S_c = 160 μm, H_c = 5 μm, d) strain energy density (mJ/mm³) at the end of relaxation step for the sagging case where S_c = 160 μm, H_c = 5 μm, (e) opening mode strain field at the end of the relaxation step for the sagging case where S_c = 160 μm, H_c = 5 μm, (f) shear mode strain field at the end of the relaxation step for the sagging case where S_c = 160 μm, H_c = 5 μm.

during LMTP printing. On the other hand, the shear stresses generated in the shear mode should

enhance the shear mode loading because both are acting in the same direction. The critical value

of the cavity size S_c where the stamp switches from sagging to the no-sagging regime is determined

for different cavity stamp heights H_c using the pick-up model. Figure 6.3 shows these results where

the cavity stamp size is presented using a dimensionless number for the cavity size $S_{cd} = S_c / L_s$,

where L_s is the ink lateral size, and as a function of the dimensionless number of the cavity height

$H_{cd} = H_c / L_s$. The figure shows two curves: one assuming strong Si-PDMS interfacial work of

adhesion ($W_I = 0.15$ J/m^2 and $W_{II} = 0.1$ J/m^2 in the opening and shear modes, respectively), and

the other assuming weak Si-PDMS interfacial work of adhesion ($W_I = 0.05$ J/m^2 and $W_{II} = 0.05$

J/m^2 in the opening and shear modes, respectively) [2] [95] [102] [119].
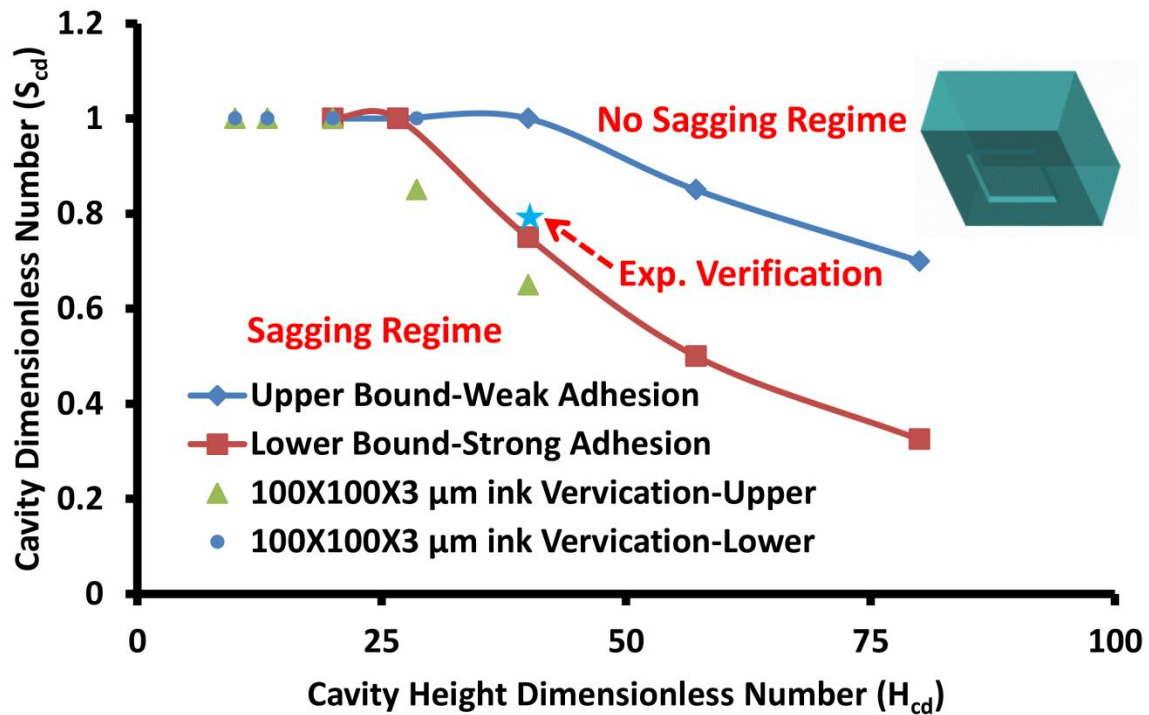
Figure 6.3. 2D CZM model results for 200×200×3 μm silicon ink pick up with different cavity sizes (S_c) at different patterned cavity heights (H_c) (the results are verified using 100×100×3 μm ink pick-up simulations).

The results are obtained for square silicon ink with size of $L_s = 200$ μm and verified using a

similar model with ink size of $L_s = 100$ μm. These results are then experimentally verified by

fabricating stamps with different cavity sizes (post height $h_p = 50$ μm; post size $L_p = 400$ μm;

114

cavity height $H_c = 5$ μm; with cavity sizes of $S_c = 80\text{-}180$ μm at 10 μm intervals). The experimental results indicate that cavity stamps sag when the cavity size $S_c \geq 160$ μm (critical size falls in the middle of the uncertainty band). Cavity height $H_c = 5$ μm has been selected to perform these experiments because it assures effective heating of the PDMS stamp while providing easy fabrication of a high resolution ($< \pm 5$ μm) SU8 mold.

6.2.2 Cavity Stamp Printing Performance

Using the pick-up model developed in Section 6.2.1, a 2D printing model is developed in ABAQUS by adding a third CZM printing step to evaluate the effect of laser beam heating on the progressive nature of the delamination process as a function of the laser beam pulse time. The CZM printing step evaluates the stored strain energy to drive the delamination as a function of mechanical loading generated at each individual node at the interface. The CZM model then compares that with the average work of adhesion of the Si-PDMS interface (defined in the traction-separation law). Based on Griffith's criterion, once the ERR reaches the work of the adhesion of the interface for any given node, the defined cohesion at the node breaks. The model uses the heating rates of the silicon ink, which are estimated by using the optical absorption model (Section 4.3). The thermally-induced air pressure within the cavity is predicted using another thermo-fluid COMSOL Multiphysics® (COMSOL, Inc.) model by heating the ink and accounting for the heat transfer within the thin air layer at the ink-stamp interface. Using the thermo-fluid model, one can estimate the thermally-included air pressure within the cavity as a function of the laser beam pulse time (see Fig. 6.4-a). The results show that the pressure field has no pressure gradients within the cavity, even though the temperature field has thermal gradients (see Fig 6.4-b. for temperature at four different points; two center-points and two corner-points). Further, model results show that the induced air pressure is independent from the cavity volume. The estimated pressure rise from

the COMSOL thermo-fluid model as a function of the laser beam pulse time (Fig. 6.4-a) is used

as an input to pressurize the internal walls of the cavity stamp in the ABAQUS print model. The

print model is then used to evaluate the delamination time by observing the time point at which

the interface separation has a smooth and continuous propagation.
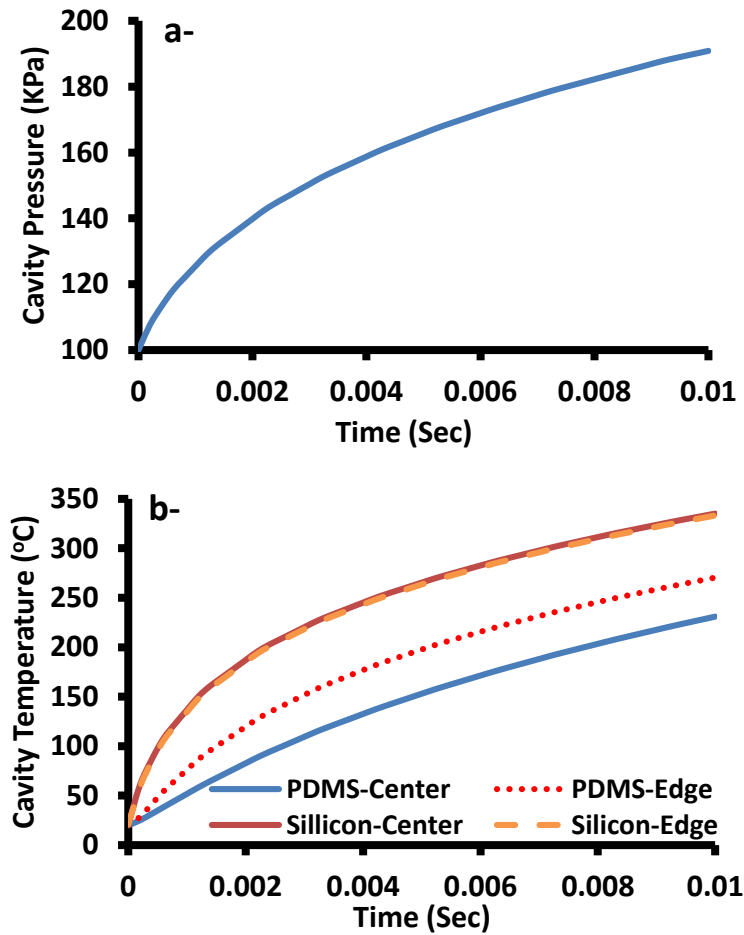
Figure 6.4. AS COMSOL model estimations for printing 200×200×3 μm ink using cavity stamp (S_c = 140 μm; H_c = 5 μm), (a) thermally induced pressure as a function of laser pulse time, and (b) cavity's corners temperature (corner at the silicon interface side is referred to as "Silicon" while the ones at the PDMS side are referred to as "PDMS"; the corner at the cavity centerline is referred to as "center" while the one at the interface internal edges are referred to as "edge").
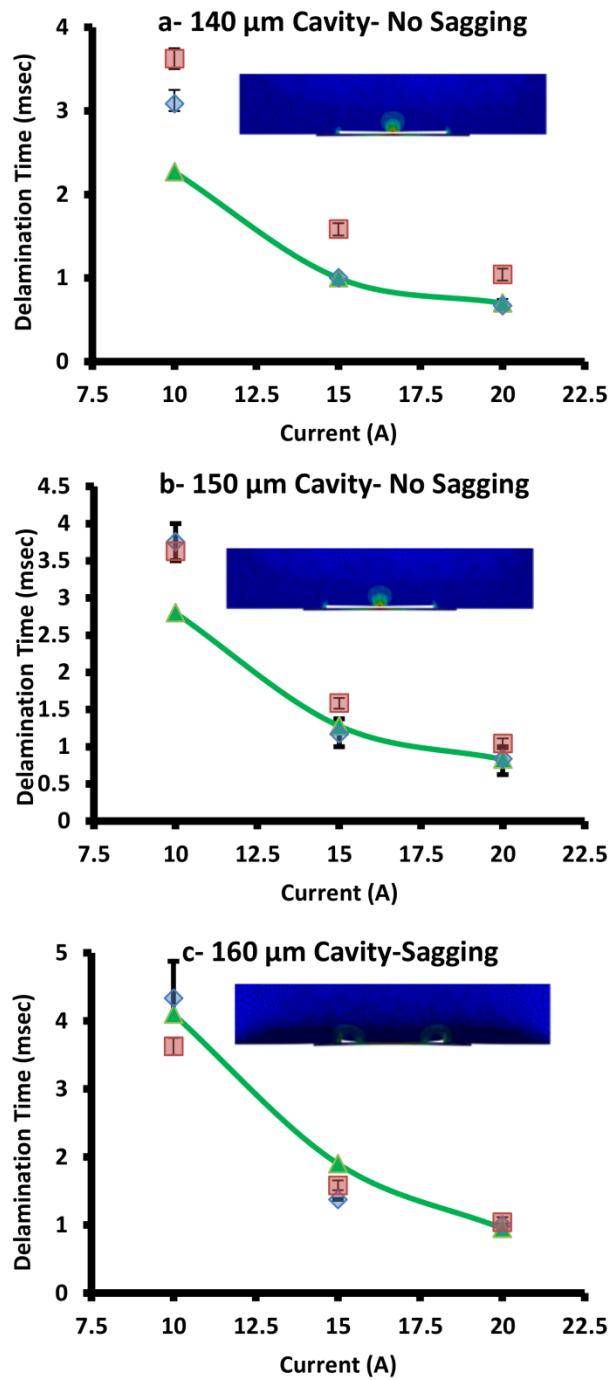
Figure 6.5. Experimental results of the delamination time compared with model estimations in printing 200×200×3 μm silicon ink with different cavity stamp sizes (S_c) with H_c = 5 μm, (a) no-sagging cavity stamp at S_c = 140 μm, (b) no-sagging cavity stamp at S_c = 150 μm, and (c) sagging cavity stamp at S_c = 160 μm (three experimental trials).

The estimated delamination times from the model for cavity stamps printing are compared with those acquired using high-speed camera recordings (three trials at each level) for the same cavity size and flat stamps. Figures 6.5-a, 6.5-b, and 6.5-c show these results for printing $200 \times 200 \times 3$ µm square silicon inks at three different laser diode currents (10, 15, and 20 A equivalent to laser beam powers of 3.268, 6.587, and 9.956 W, respectively at the ink-stamp interface plane) for cavity sizes $S_c = 140$, 150, and 160 µm, respectively. For printing using no-sagging cavity stamps ($S_c = 140$ µm and $S_c = 150$ µm), the results show that the reduction of the delamination times depend on the cavity size because the sealing at the interface is an issue (experiments show no improvement when $S_c = 150$ µm because it is difficult to achieve sealing between the stamp and the ink). However, the print model does not account for these issues by assuming prefect sealing (the model results show reduction in the delamination time especially at 10 A current level). In case of printing with no-sagging cavity stamps with good sealing ($S_c = 140$ µm), the experimental results show reductions (15%, 37%, and 36% for 10, 15, and 20 A, respectively) in the delamination times compared with that for flat stamps. These reductions in the delamination times match the model estimates for 15 and 20 A, while the model overestimates the reduction at 10 A current. A possible reason is that the heating rate of the silicon ink at 10 A current level is slowly relaxing the generated mechanical loads or leaking the thermally-induced air pressure within the cavity. As estimated from the print model, printing with sagging cavity stamps shows no reductions in delamination time over printing with flat stamps (Fig. 6.5-c for $S_c = 160$ µm). Moreover, evaluating the delamination energies shows that the delamination energies (Fig. 6.6-a) improve by the same percentages for the delamination time at any given current level (delamination energy is the product of delamination time and power absorbed by the ink). Evaluation of the ink-stamp interface temperature at the delamination point measured experimentally using the print model

shows that interface temperatures are only reduced by ~8% in the cases of printing with cavity size $S_c = 140$ μm at 15 and 20 A current levels, where higher improvements in the delamination times are observed. Cavity stamps with cavity size of $S_c = 140$ μm are also used in printing 200×200×30 μm square silicon inks (see Fig. 6.7). The results show reductions (11%, 14%, and 14% for 10, 15, and 20 A, respectively) in the delamination times Fig. 6.7-a and delamination energy Fig. 6.7-b
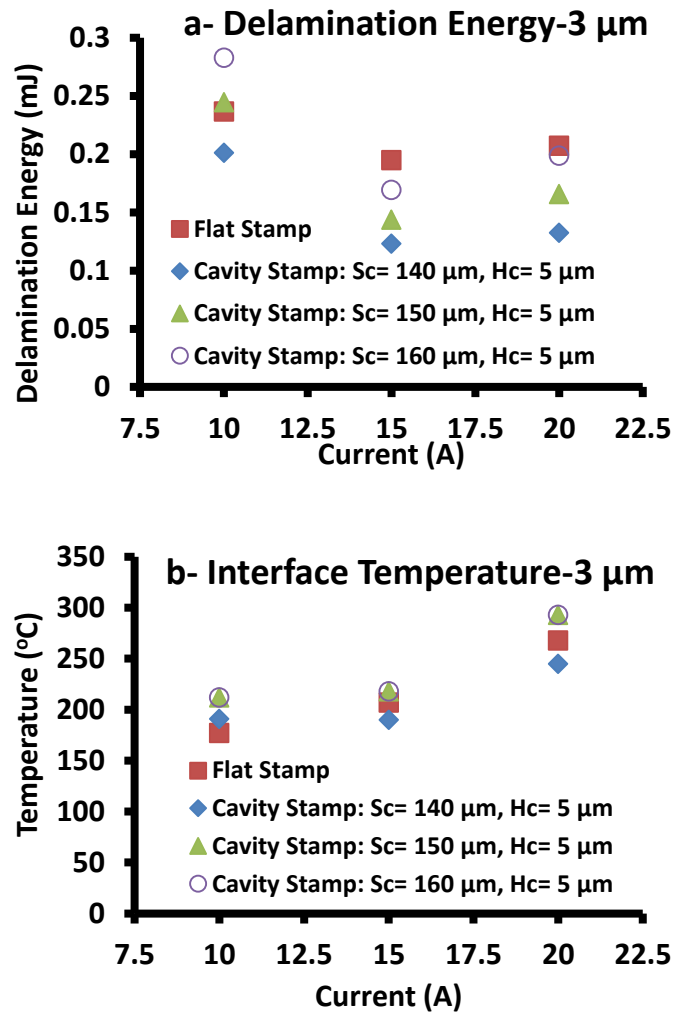
Figure 6.6. Printing 200×200×3 μm silicon ink with different cavity stamp sizes (S_c), (a) experimental results of the delamination energy, and (b) model estimations of the interface temperature at the delamination time measured experimentally using high-speed camera.
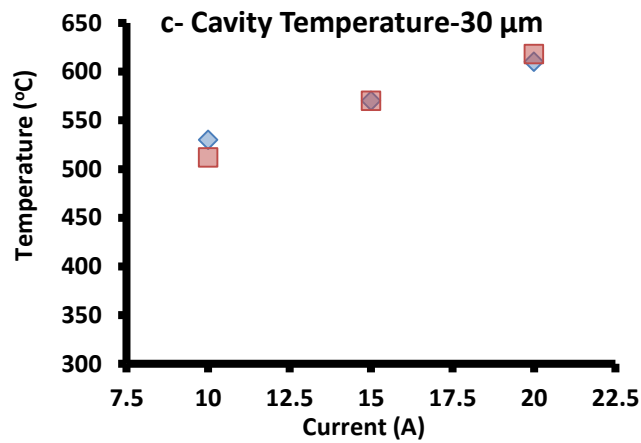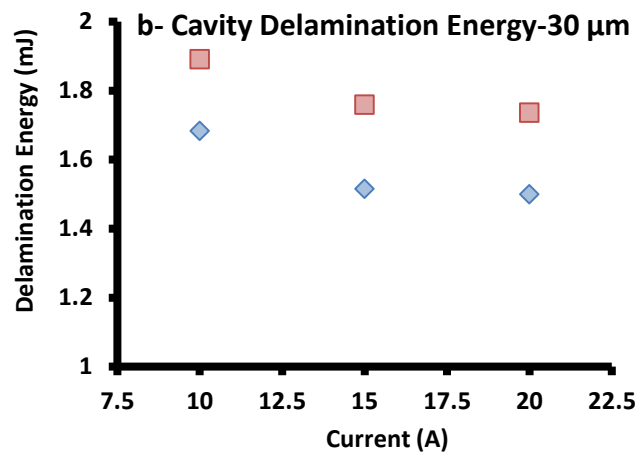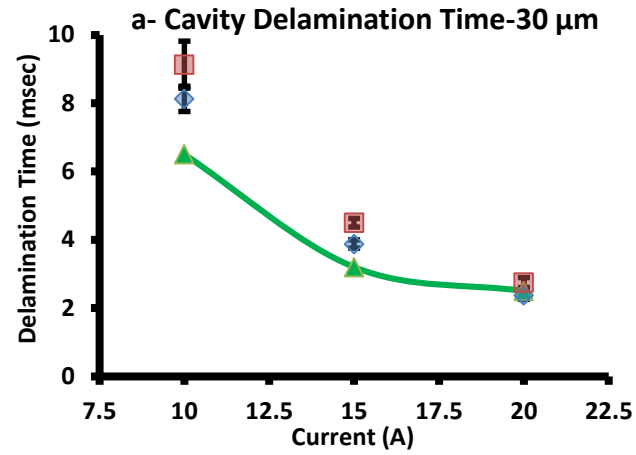
Figure 6.7. Printing 200×200×30 μm silicon inks using no-sagging cavity stamp sizes S_c = 140 μm with H_c = 5 μm, (a) delamination time, (b) delamination energy, and (c) interface temperature at the delamination point.

for printing using cavity stamps compared with that for flat stamps. Figure 6.7-a also shows that the print model estimates less improvement in the delamination time for printing 200×200×30 μm square silicon inks compared to that for printing 200×200×3 μm silicon inks for all laser current levels. However, the estimated interface temperatures from the print model (Fig. 6.7-c) at the delamination times show no reduction compared to flat stamps at all current levels. Therefore, cavity stamps improve the LMTP process performance in printing thin inks at medium to higher laser power levels (200×200×3 μm; 15 and 20 A current**).**

6.3 Preloaded Stamps

Proceeding from cavity stamps, this section will discuss how preloaded stamps are designed and used to improve the LMTP process performance.

6.3.1 Preloaded Stamp Design for Pickup

Similar to a cavity stamp, an ABAQUS pick-up model for preloaded stamps (including both the static preloading and the CZM relaxation steps) has been developed to evaluate the stamps' performance during the ink pickup. The pick-up model predicts the performance of the preloaded stamps at the end of the pick-up process to determine if the step at the interface will collapse to store strain energy at the interface (see Fig. 6.8-a and 6.8-b, for bad and good preloaded stamp designs, respectively). The developed strains during the ink pickup at the end of the relaxation step are shown in Fig. 6.8-c and 6.8-d for the opening and shear modes, respectively. The results show at the end of the ink pickup for good (collapsed) stamps, tensile strains are generated at the ink-stamp interface external edges, in the opening mode direction. However, compressive strains are developed at internal interface edges between the patterned step and the ink interface suspending the effect of the thermal gradient strains generated by laser heating. Therefore, this indicates that using preloaded stamps might not improve the LMTP process. The critical size of the preloading

step S_l where the stamp switches from a collapse to no-collapse regime is determined for different preloaded stamp step heights H_l using the pick-up model. Figure 6.9 shows these results where the preloaded stamp's step size is presented using a dimensionless number for the step size $S_{ld} = S_l / L_s$ and as a function of the dimensionless number of the step height $H_{ld} = H_l / L_s$. Similar to the cavity stamp, the figure shows two curves: one assuming strong Si-PDMS interfacial work of adhesion ($W_I = 0.15$ J/m^2 and $W_{II} = 0.1$ J/m^2 in the opening and shear modes, respectively); and the other assuming weak Si-PDMS interfacial work of adhesion ($W_I = 0.05$ J/m^2 and $W_{II} = 0.05$ J/m^2 in the opening and shear modes, respectively). The results are obtained for square silicon ink with a size of $L_s = 200$ μm and verified using a similar pick-up model with ink size of $L_s = 100$ μm. These results are verified by fabricating preloaded stamps with different step sizes (post height $h_p = 50$ μm; post size $L_p = 400$ μm; step height $H_l = 5$ μm; with step sizes of $S_l = 50$-140 μm at 10 μm
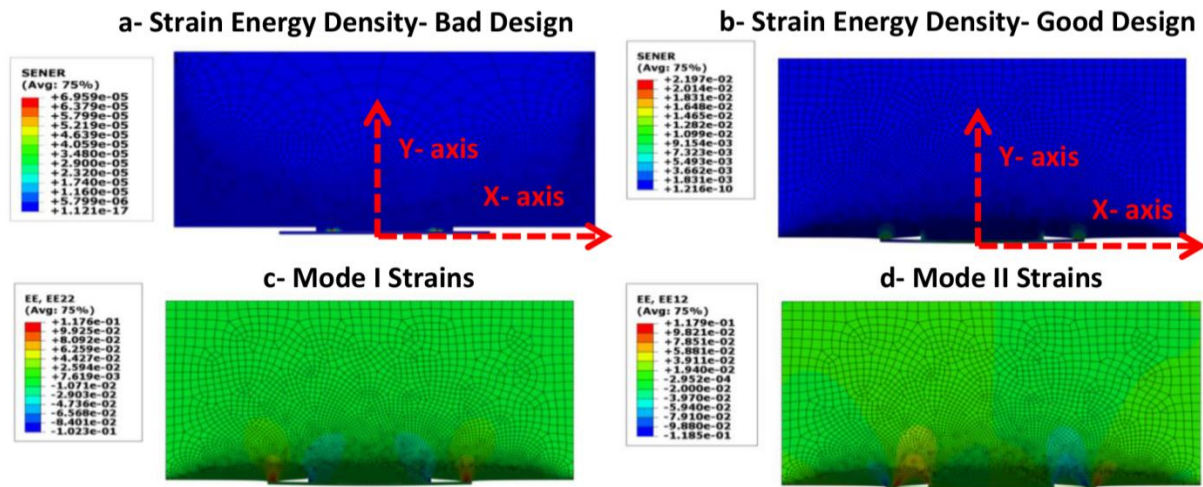
Figure 6.8. 2D CZM model results for 200×200×3 μm silicon ink pick up using preloaded stamps, (a) strain energy density (mJ/mm³) for bad preloading stamp design (no sagging case where $S_l = 110$ μm, $H_l = 5$ μm), (b) strain energy density (mJ/mm³) for good preloading stamp design (sagging case where $S_l = 100$ μm, $H_l = 5$ μm), (c) opening mode strain field at the end of the relaxation step for good design, and (d) shear mode strain field at the end of the relaxation step for good design for good design.

intervals). The experimental results indicate that the preloaded stamp step does not collapse when the step size $S_l \geq 100$ µm (critical size belongs to the uncertainty band). Preloading step height H_l = 5 µm has been selected for the same reason as that discussed for cavity stamps.

6.3.2 Preloaded Stamp Printing Performance

The results for printing 200×200×3 µm square silicon ink using preloaded stamps (S_l = 100 µm; H_l = 5 µm) are shown in Fig. 6.10-a, 6.10-b, and 6.10-c for the delamination times, energies, and interface temperatures, respectively. The experimental results (Fig. 6.10-a and 6.10-b) show that printing using preloaded stamps has no improvement in the delamination times and energies over flat stamps at 10 A current level. For 15 and 20 A current levels, the delamination time and
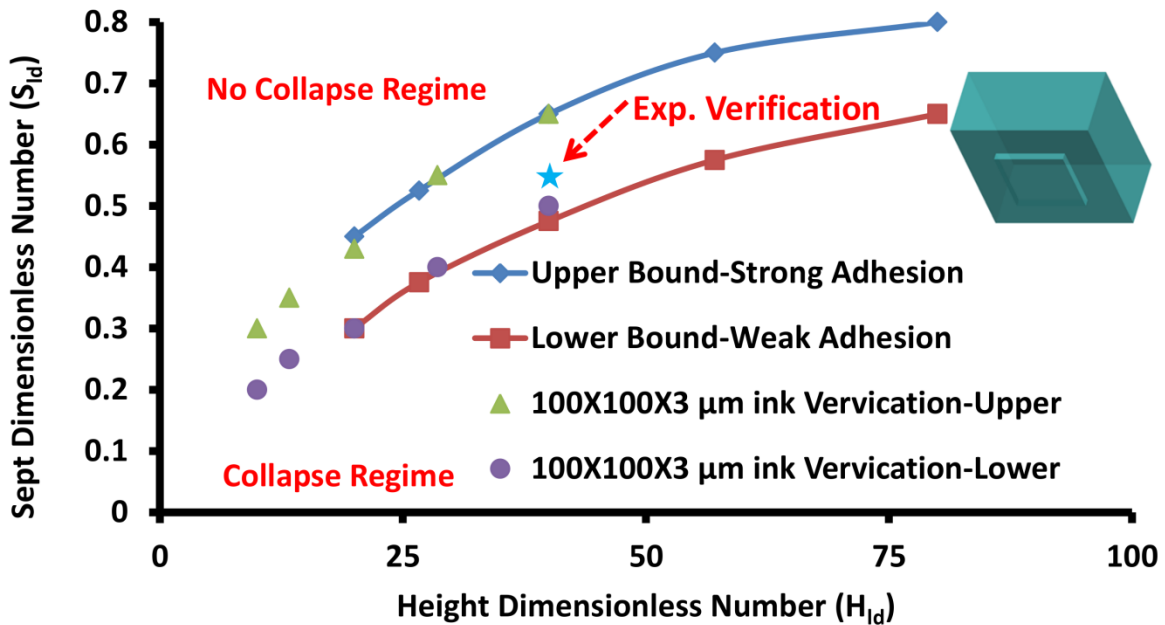
Figure 6.9. 2D CZM model results for 200×200×3 µm silicon ink pick up with different preloaded stamp sizes (S_l) and patterns heights (H_l), the results are verified using 100×100×3 µm silicon ink pick-up simulations.

energies are improved by 15% and 32 % as expected from the CZM printing model. Moreover, the temperature of the interface at the delamination point improves only at 20 A current. For printing $200\times200\times30$ μm square silicon inks using preloaded stamps ($S_l = 100$ μm; $H_l = 5$ μm), the results (Fig. 6.11-a and 6.11-b) indicate that preloaded stamps improve on the delamination times and energies by ~8% at 10 and 15 A current levels, while printing at 20 A current level shows no improvement. The CZM print model shows good agreement with the experimental results at 15 and 20 A current, while it underestimates the actual delamination time at 10 A current due to the strain relaxation issue at low heating rates. Further, no improvement on the temperatures of the interface at the delamination time (Fig. 6.11-c) is estimated based on the print model for printing $200\times200\times30$ μm silicon inks. Therefore, preloaded stamps improve the LMTP process in printing thin ink at high power levels only ($200\times200\times3$ μm; 20 A current).
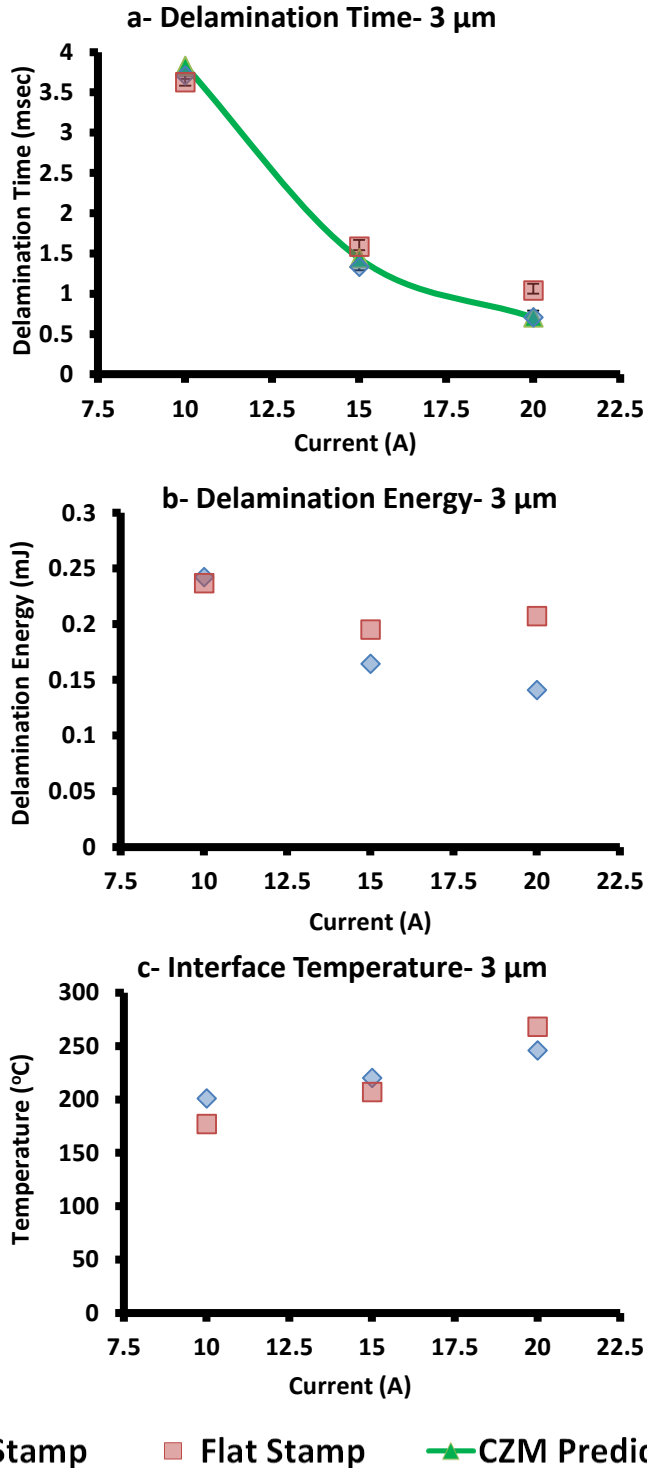
Figure 6.10. Printing 200×200×3 µm silicon inks using preloaded stamps (S_l = 100 µm and stamp height H_l = 5 µm) at different laser diode current, (a) delamination times, (b) delamination energies, and (c) model estimates for interface temperatures.
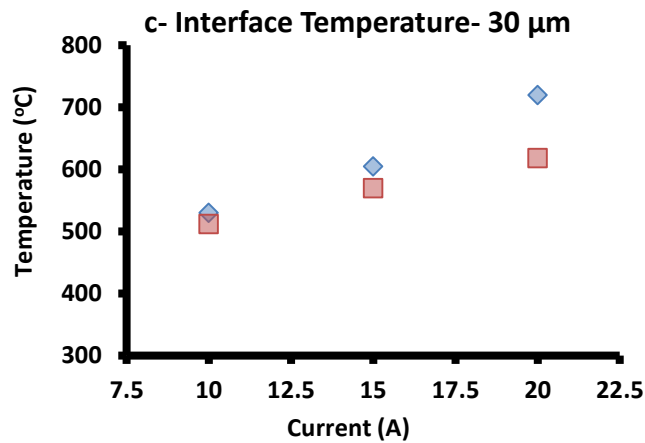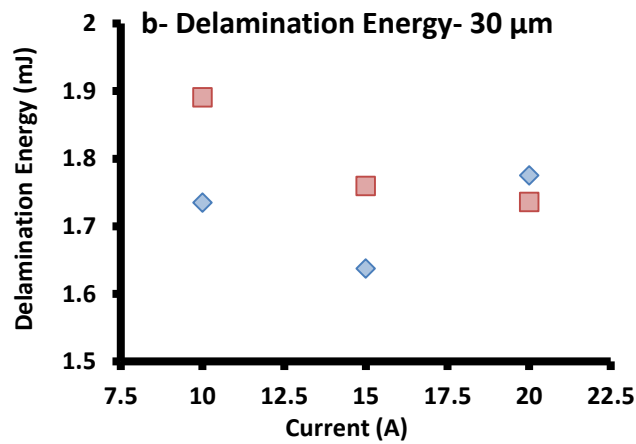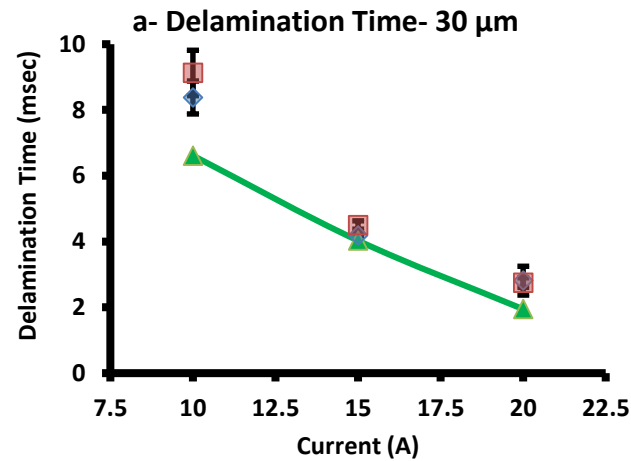
Figure 6.11. Printing 200×200×30 μm silicon inks using preloaded stamps ($S_l = 100$ μm and stamp height $H_l = 5$ μm) at different laser diode current, (a) delamination times, (b) delamination energies, and (c) model estimates for interface temperatures.

6.4 Thin-Wall Stamps

The thin-wall stamp has been proposed as a hybrid design (combines cavity and preloaded stamps, see Fig. 6.12) to generate thermally-induced air pressure and collapse the thin-wall pattern to store strain energy at the interface edges. Similar to use with cavity and preloaded stamps, a pick-up model has been developed to design the critical stamp dimensions (S_{t1} and S_{t2}) for given thin-wall pattern heights (H_t). For $H_t = 5$ μm; the critical outer dimension for stamp collapse (similar to preloading stamps) is estimated to be $S_{t2} = 90$ μm from the pick-up model to achieve collapse of the thin-wall feature. For the critical outer dimension value, the cavity does not sag given a pattern height of $H_t = 5$ μm. Therefore, the inner thin-wall feature dimension is chosen to be $S_{t1} = 60$ μm (larger S_{t1} generates higher stress at the interface edges; however, it is difficult to fabricate a SU8 mold feature with a resolution of less than 15 μm).

Figure 6.12. 2D pick-up model estimation for the strain energy density (mJ/mm³) at the end of the relaxation step for 200×200×3 μm ink pick up using thin-wall stamp ($S_{t1} = 60$ μm, $S_{t2} = 90$ μm, and $H_t = 5$ μm).

The results for printing $200\times200\times3$ μm square silicon inks using thin-wall stamps ($S_{t1} = 60$ μm; $S_{t2} = 90$ μm; $H_t = 5$ μm) are shown in Fig. 6.13-a, 6.13-b, and 6.13-c for the delamination times, energies, and interface temperatures, respectively. The results show improvements up to ~35% in the delamination times and energies observed for all power levels. The print CZM model for thin-wall stamp estimates show similar behaviors for 15 and 20 A current levels, while it underestimates the improvement at 10 A current. The temperatures of the interface at the delamination point (Fig. 6.13-c) are improved for all laser current levels, and the highest improvement is estimated at 10 A current level (~16%). For printing $200\times200\times30$ μm square silicon inks using thin-wall stamps ($S_{t1} = 60$ μm; $S_{t2} = 90$ μm; $H_t = 5$ μm), the experimental results (Fig. 6.14-a and 6.14-b) indicate that these stamps improve the delamination times and energies by ~20%, 22%, and 9% for 10, 15, and 20 A current levels, respectively. Similar to printing $200\times200\times3$ μm inks, the print CZM model for thin-wall stamps reasonably estimates these improvements for 15 and 20 A current levels, while it underestimates that for the 10 A current level. The interface temperatures at the delamination point for printing $200\times200\times30$ μm (Fig. 6.14-c) improve only at 10 and 15 A current levels. Therefore, thin-wall stamps improve the LMTP process performance in printing thick ink at a low power level ($200\times200\times30$ μm; 10 and 15 A current levels) and thin inks for all power levels ($200\times200\times3$ μm; 10, 15, and 20 A current). Further, the process enhancement in printing using thin-wall stamps mainly follows from the cavity effects.
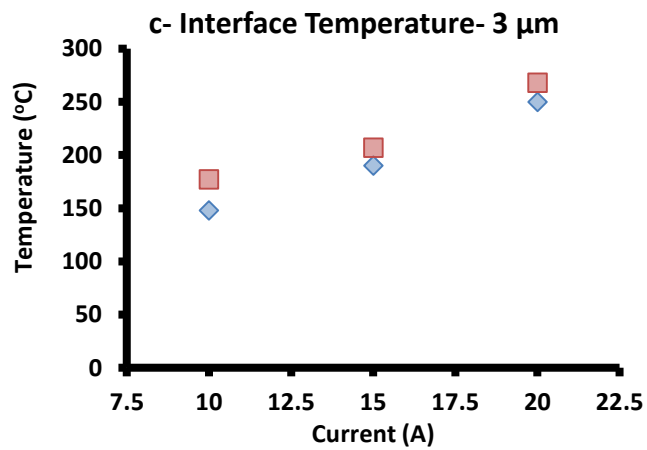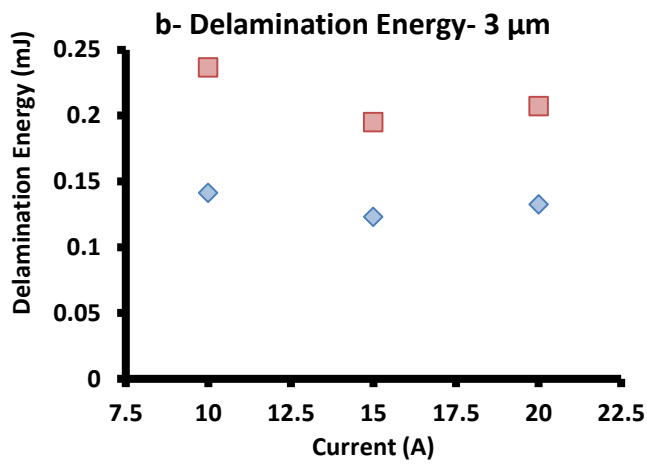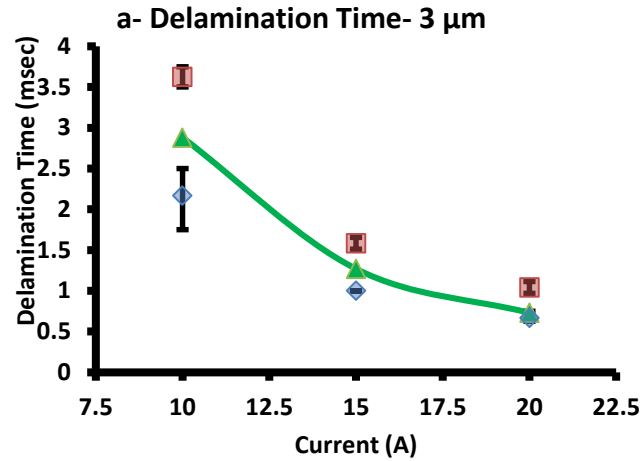
Figure 6.13. Printing 200×200×3 μm silicon inks using thin-wall stamps ($S_{t1} = 60$ μm, $S_{t2} = 90$ μm, and $H_t = 5$ μm) at different laser diode current, (a) delamination time, (b) delamination energy, and (c) model estimates for interface temperature.
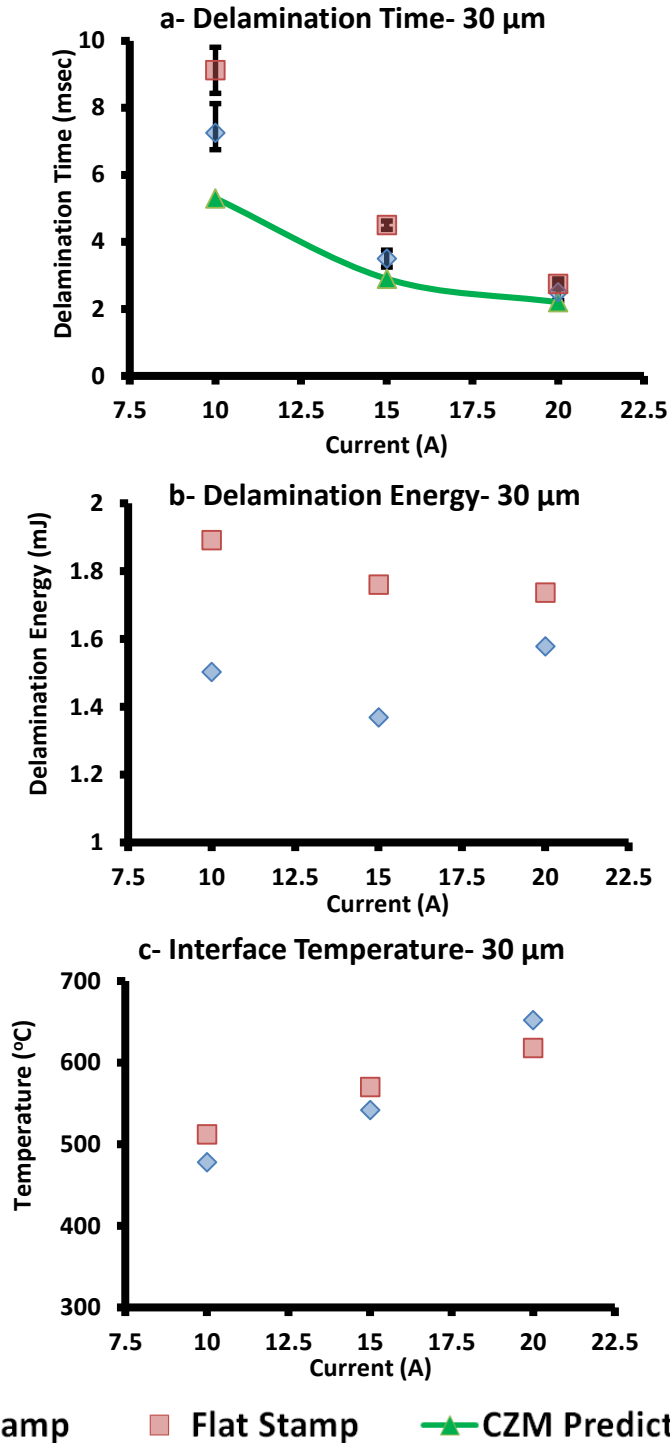
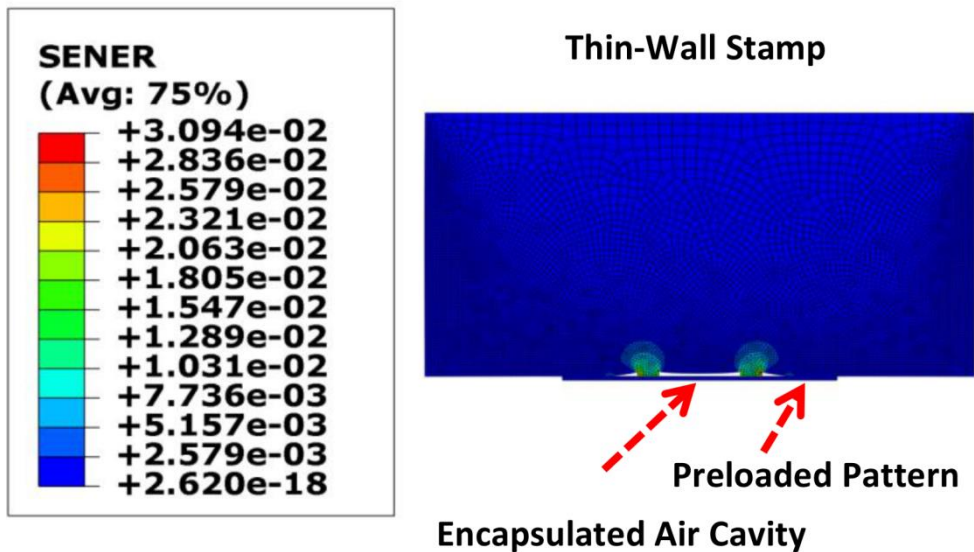**Figure 6.14. Printing 200×200×30 μm silicon inks using thin-wall stamps (S_{t1} = 60 μm, S_{t2} = 90 μm, and H_t = 5 μm) at different laser diode current, (a) delamination time, (b) delamination energy, and (c) model estimates for interface temperature.**

130

6.5 Summary

In this chapter, patterned stamps are proposed to achieve printing at lower energy and interface temperature by enhancing mode I loading. Three different stamp designs (cavity, preloaded, and thin-wall) have been proposed to improve the LMTP process performance. Both pick-up and printing CZM models for each design have been developed to evaluate the stamp's performance in ink pick-up and LMTP printing. The results show that both cavity and thin-wall stamps can improve the delamination times and energies up to ~35% compared to flat stamps with no patterns. The improvements on the interface temperatures of up to 16% are reported for thin-wall stamps, and around 8% for cavity stamps. The preloaded stamps show some improvements in the delamination times, energies, and interface temperatures; however, these improvements are smaller compared with the cavity and the thin-wall stamps. Further, printing thin inks using patterned stamps showed more improvement compared with printing thick inks for all different patterned stamp designs.

CHAPTER 7: CONCLUSIONS AND FUTURE WORK

7.1 Conclusions

A second generation LMTP printer was developed to automate the printing cycle and improve the process accuracy and repeatability. The printer head is calibrated and used to measure the laser beam power absorbed by square silicon inks of different sizes and thicknesses. Then, a series of experiments were conducted to measure the time required to start delamination for different square ink sizes and thicknesses at different laser beam power levels. The results show high process repeatability with the general tendency for an increase in delamination time, with an increase in ink size from 100 to 200 µm, an ink thickness increase from 3 to 50 µm, and a laser beam diode current decrease from 20 to 10 A. The results from both the delamination time with amount laser beam power absorbed by the square silicon ink are used to determine the amount of energy required to start the LMTP delamination process. The energy required for delamination increases with the increase of the ink size from100 to 200 µm or thickness from 3 to 50 µm. The range of the required energy for delamination ~0.1 to 3 mJ shows that the LMTP process energy requirements for delamination are highly dependent upon the ink dimensions.

A multi-physics model has been developed to understand and predict the effects of the multi-physics (opto-thermo-mechanical) involved in the LMTP delamination process. The modeling approach is based on decoupling the laser optical absorbance physics from the laser-driven coupled thermo-mechanical physics, which generate the thermal stresses at the interface. A series of experiments were conducted to verify the heating rate estimated from the optical absorption model. Comparisons of measured laser beam powers absorbed with those powers computed by a theoretical model (developed based on the optical absorbance) showed good agreements in both

132

trend and values. Both of the inks' heating rates from the optical absorption model and the delamination times from the high-speed camera are then used as inputs for a coupled thermo-mechanical FEA model. The FEA model was calibrated based on the increase of the lateral dimensions of the PDMS post that were experimentally measured using a high-speed camera. The model was then simplified to an axisymmetric model to study the LMTP process mechanism. The model allows for the estimation of the temperatures reached in the ink during the LMTP process. It also identified that the thermal gradient features in the strain field, in addition to CTE mismatch strain, assist in initiating and driving the delamination process. In addition, the model also predicted the vertical translation of the ink due to expansion on the PDMS. Such predictions are useful in planning the stand-off height for the LMTP process. The model indicates that any current level can be used to print because the temperature at the delamination point for printing square silicon ink is nearly independent of the laser diode current level.

The study has shown that the LMTP process is a mixed-mode process (mode II is two times more dominant than mode I) where the critical ERR and SIFs (in both modes) were of equal magnitude for printing the same ink thickness at different laser current levels. However, for printing different ink thicknesses, the critical ERR and SIFs (in both modes) were dependent on the ink thickness. Given the higher temperatures encountered in printing thicker inks, it is possible that plastic strain and temperature-dependent properties of the PDMS at these temperatures relax the mismatch strains or lower the developed energy levels at the interface, respectively, to produce the apparent high critical ERR computed for thick inks. This implies that the LMTP process is more efficient and better understood for the case of printing thin inks ($h_s < 10$ μm) hence the model predictions for delamination time agree with the experimental values. Furthermore, the ERR or SIFs at the edge of the interface where the delamination crack originates decomposed into two

133

components: one due to CTE mismatch and the other due to the thermal gradients within the PDMS. Both components are significant in both fracture loading directions (mode I and mode II), suggesting that both the high coefficient of thermal expansion and the low thermal conductivity of the PDMS are essential properties for it to function as a stamp material in the LMTP process.

Other studies have been conducted to investigate the effect of the stamp post dimensions, the effect of ink-stamp misalignment, the effect of different PDMS formulations, and the effect of the ink shape on the LMTP process performance and mechanism. The effects of modifying these parameters are explored using FEA model estimations and experimental measurements. For example, in printing with different post sizes, printing with a stamp that has a smaller post compared to the ink can reduce the delamination times and energies; however, it increases the interface's temperature. Therefore, printing with a stamp post that has ink-post lateral dimension ratio $R > 1.5$ value is always preferable to improve the printing accuracy (unlike printing at $R = 1$) and lower the interface temperature compared with $R < 1$ value stamp posts. Further, the height of the post and the thickness of the PDMS backing layer should not affect the LMTP printing performance as long as it is enough to selectively pick up the ink and hold the stamp with the glass holder substrate, respectively. Moreover, printing at $R = 1$ value is highly sensitive to misalignment between the ink and the stamp post and generates unbalanced energy releases at the interface's edges, leading to a reduction in the printing accuracy, while print $200 \times 200 \times 3$ μm inks at $R = 2$, for example, are unaffected by any misalignment less than ± 50 μm.

Printing with h-PDMS stamps might reduce the LMTP delamination time over printing s-PDMS (mixing ratio of s-PDMS does not show a significant effect on improving the delamination time). However, s-PDMS is still preferable due to its simplicity with fabrication and its reliability during printing (h-PDMS is brittle and fractures easily). In the case of printing different ink shapes,

even though at a given time annular inks usually have less interface temperatures, compared to solid inks, the interface temperature at the delamination point is usually lower for solid inks. Therefore, for printing active devices where the high temperature might damage the film, users should preferably use solid inks rather than annular inks with 10 A current level. For annular inks, using 15 and 20 A current levels, where the temperatures of interface are lower, are recommended.

Patterned stamps are proposed to achieve printing at lower energy and interface temperature by enhancing mode I loading (opening mode SIF is lower than shear mode II SIF while the work of adhesion required to break the interface is usually higher in mode I). Three different stamp designs (cavity, preloaded, and thin-wall) have been proposed to improve the LMTP process performance. Both pick-up and printing CZM models for each design have been developed using ABAQUS to evaluate the stamp's performance in ink pickup and LMTP printing. The results show that both cavity and thin-wall stamps can improve the delamination times and energies up to ~35% compared to flat stamps with no patterns. Improvements on the interface temperatures of up to 16% were observed for thin-wall stamps, and around 8% for cavity stamps. The preloaded stamps show some improvements in the delamination times, energies, and interface temperatures; however, these improvements are smaller compared to the cavity and the thin-wall stamps. Further, printing thick inks using patterned stamps showed less improvement compared with printing thin inks for the three different patterned stamp designs.

7.2 Recommendations for Future Work

➢ The design and fabrication of a laser scanner to control the laser beam path; so as to achieve strip ink and batch array printing, is recommended.

➢ The stamp material can be engineered to embed a NIR absorbance layer, so that the laser beam energy can be absorbed to make the LMTP process independent from the optical properties of the ink material. The idea is to achieve a self-expandable stamp and print different ink materials.

➢ The stamp material can be engineered to embed an absorbance layer of silicon micro/nano-wires for absorbing the laser beam energy and reducing the lateral stamp stiffness to make the LMTP process independent from the optical properties of the ink material.

➢ The stamp material can be engineered to embed capsules of a phase-transformation material to enhance the energy conversion efficacy to print at lower ink temperatures. Micro-capsules can be made out of water, NIR dye (i.e. Epolight 2735) dissolved in water, sublime materials, or low boiling point fluorocarbon materials (i.e. Perfluorohexane, Perfluoroheptane, Perfluorooctane, Perfluorononane, Perfluorodecane, Perfluorodecalin, and Perfluorocyclohexane). These stamps should enhance the stamp efficiency to get larger expansion with shorter laser pluses.

➢ The stamp material can be engineered to print using porous or multi-cavity PDMS stamps to reduce the contact surface area and generate thermally-induced air pressure. These cavities can also be filled with NIR dye dissolved in water.

➢ The PDMS temperature-dependent behavior of the PDMS can be investigated to develop a full understanding of the delamination when printing thick inks, where high temperatures are involved. Further, the thermal decomposed PDMS material should be investigated to

understand how the PDMS decomposes in oxygen-rich vs. oxygen-poor environments. These results should help in understanding why the stamp degrades at high temperatures and how to increase the stamp life.

➢ The LMTP process can be used to build functional MEMS devices or passive MEMS microstructures. For example, 3D microstructures on a silicon surface can be assembled using the LMTP process because it is a non-contact process. The built structure can be used as a mask to create 3D features on the receiving substrate using the Deep Reactive-Ion Etching (DRIE) process.

➢ The CZM model in Chapter 4 can be used to estimate the ERR as a function of the crack propagation length using Virtual Crack Closure Technique (VCCT). Such understanding should help in further investigations of the LMTP process mechanism.

REFERENCES

[1]   Meitl, M. A., et al., 2005. Transfer printing by kinetic control of adhesion to an elastomeric stamp. Nature Materials, 5/1: 33-38

[2]   Kim, S., et al., 2010. Microstructured elastomeric surfaces with reversible adhesion and examples of their use in deterministic assembly by transfer printing. Proceedings of the National Academy of Sciences of the USA, 107/40: 17095-17100.

[3]   Saeidpourazar, R., et al., 2012. A prototype printer for laser driven micro-transfer printing. Journal of Manufacturing Processes, 14/4: 416-424.

[4]   Saeidpourazar, R., et al., 2012. Laser-driven micro transfer placement of prefabricated microstructures. Journal of Microelectromechanical Systems, 21/5: 1049-1058.

[5]   Chanda, D., et al., 2011. Large-area flexible 3D optical negative index metamaterial formed by nanotransfer printing. Nature Nanotechnology, 6: 402-407.

[6]   Kim, H., et al., 2011. Unusual strategies for using indium gallium nitride grown on silicon (111) for solid-state lighting. Proceedings of the National Academy of Sciences of the USA, 108/25: 10072-10077.

[7]   Kim, T.-H., et al., 2011. Full-colour quantum dot displays fabricated by transfer printing. Nature Photonics, 5: 176-182.

[8]   Cao, Q., et al., 2008. Medium-scale carbon nanotube thin-film integrated circuits on flexible plastic substrates. Nature 2008, 454: 495-500.

[9]   Carlson, A., et al., 2012. Transfer printing techniques for materials assembly and micro/nanodevice fabrication. Advanced Materials, 24/39: 5284-5318.

[10]   Rajaraman, V., et al., 2012. Below-IC post-CMOS integration of thick MEMS on a thin-SOI platform using embedded interconnects. International Conference on Micro Electro Mechanical Systems, 25: 220-223.

[11]   Fedder, G. K., et al., 2008. Technologies for cofabricating MEMS and electronics. Proceedings of the IEEE, 96/2: 306-322.

[12]   Smith, J., et al., 1995. Embedded micromechanical devices for the monolithic integration of MEMS with CMOS. International Electron Devices Meeting, 199: 609-612.

[13]   Tummala, R., 2004. SOP: what is it and why? A new microsystem-integration technology paradigm-Moore's law for system integration of miniaturized convergent systems of the next decade. IEEE Transactions on Advanced Packaging, 27/2: 241-249.

[14]   Beica, R., et al., 2008. Through silicon via copper electrodeposition for 3D integration. Electronic Components and Technology Conference, 58: 577-583.

[15] Lee, K., et al., 2011. Three-dimensional hybrid integration technology of CMOS, MEMS, and photonics circuits for optoelectronic heterogeneous integrated systems. IEEE Transactions on Electron Devices, 58/3: 748-757.

[16] Lapisa, M., et al., 2011. Wafer-level heterogeneous integration for MOEMS, MEMS, and NEMS. IEEE Journal of Selected Topics in Quantum Electronics, 17/3: 629-644.

[17] Fischer, A., et al., 2010. Heterogeneous integration for optical MEMS. Annual Meeting of the IEEE Photonics Society, 23: 487-488.

[18] Lee, K., et al., 2009, Heterogeneous integration technology for MEMS-LSI multi-chip module. IEEE International Conference on 3D System Integration, 1-6.

[19] Yi, Y., and Liu, C., 1998. High-yield assembly of hinged 3D optical MEMS devices using magnetic actuation. Proceeding Micromachining and Microfabrication Process Technology, 3511: 125-134.

[20] Xue, Y., and He, S., 2013. Novel Automated microassembly mechanism based on on-chip actuators. Journal of Micro/Nanolithography, MEMS, and MOEMS, 12/1: 013003-8.

[21] Tanaka, S., et al., 2013. Wafer-to-wafer selective flip-chip transfer by sticky silicone bonding and laser debonding for rapid and easy integration test. International Conference on Micro Electro Mechanical Systems, 26: 271-274.

[22] Yi, Y., and Liu, C., 1998. Mechanically-stable micro assembly using magnetic actuation. International Conference on Solid-State and Integrated Circuit Technology, 5: 939-942.

[23] Kaajakari, V., and Lal, A., 1999. Pulsed ultrasonic release and assembly of micromachines. Transducer, 99: 7-10.

[24] Kaajakari, V., and Lal, A., 2003. Thermokinetic actuation for batch assembly of microscale hinged structures. Journal of Microelectromechanical Systems, 12/4: 425-432.

[25] Chu, H. K., et al., 2012. Automated parallel microassembly for MEMS application. Journal of Micromechanics and Microengineering, 22/3: 035017-9.

[26] Fantoni, G., 2003. Assembly of mini and microparts: development of an electrostatic feeder. AITEM Conference Enhancing the Science of Manufacturing, 6: 352-366.

[27] Gullo, M. R., et al., 2013. In-liquid MEMS assembly by optical rapping. IEEE International Conference on Micro Electro Mechanical Systems, 26: 78-81.

[28] Ostendorf, A., et al., 2013. Optical tweezers in microassembly. SPIE LASE, 86070U-86070U-11.

[29] Hesselbach, J., et al., 2001. Centering electrostatic microgripper and magazines for microassembly Tasks. Proceeding SPIE, 4568: 270-277.

[30] Bohringer, K., et al., 1998. Parallel microassembly with electrostatic force fields. IEEE International Conference on Robotics and Automation, 2: 1204-1211.

[31]   Erzincanli, F., et al., 1998. Design and operational considerations of a non-contact robotic handling system for non-rigid materials. International Journal of Machine Tools and Manufacture, 38/4: 353-361.

[32]   Vikramaditya, B., et al., 2001. Microassembly of hybrid magnetic MEMS. Journal of Micromechatronics, 1/2: 99-116.

[33]   Nof, S.Y., 1999. Handbook of Industrial Robotics. John Wiley & Sons.

[34]   Lai, K. W., 2004. Automated micro-assembly of optical MEMS structure by centrifugal force. World Congress on Intelligent Control and Automation, 5: 5624-5628.

[35]   Cho, Y. S., and Drayton, R., 2006. Novel integration technique for flip-chip bonding circuit in wafer scale packaging. IEEE Antennas and Propagation Society International Symposium, 57-60.

[36]   Kim, C., 1992. Silicon-processed overhanging microgripper. Journal of Microelectromechanical Systems, 1/1: 31-36.

[37]   Grunow, M., et al., 2004. Operations planning for collect-and-place machines in PCB assembly. Computers & Industrial Engineering, 47/4: 409-429.

[38]   Braun, S., 2010. Wafer-level heterogeneous integration of MEMS actuators. Ph.D. Dissertation, KTH.

[39]   Cicek, P., et al., 2013. A novel prototyping method for die-level monolithic integration of MEMS above-IC. Journal of Micromechanics and Microengineering, 23/6: 065013.

[40]   Goyal, A., et al., 2004. Tin-based solder bonding for MEMS fabrication and packaging applications. Journal of Micromechanics and Microengineering, 14/6: 819-825.

[41]   Cohn, M. B., et al., 1998. Microassembly technologies for MEMS. Micromachining and Microfabrication Process Technology, 4: 2-16.

[42]   Chang, C., and Hsu, W., 2009. Three-dimensional micro assembly of a hinged nickel micro device by magnetic lifting and micro resistance welding. Journal of Micromechanics and Microengineering, 19/10: 105026-8.

[43]   Benson, R. C., et al., 2008. Polymer adhesives and encapsulants for microelectronic applications. Johns Hopkins APL Technical Digest, 28/1: 58-71.

[44]   Berthold, A., et al., 2000. Glass-to-glass anodic bonding with standard IC technology thin films as intermediate layers. Sensors and Actuators A: Physical, 82/1: 224-228.

[45]   Cheng, Y., et al., 2000. Localized silicon fusion and eutectic bonding for MEMS fabrication and packaging. Journal of Microelectromechanical Systems, 9/1: 3-8.

[46]   Tiensuu, A., et al., 1994. Assembling three-dimensional microstructures using gold-silicon eutectic bonding. Sensors and Actuators A: Physical, 45/3: 227-236.

[47] Thompson, K., et al., 2002. Direct silicon-silicon bonding by electromagnetic induction heating. Journal of Microelectromechanical Systems, 11/4: 285-292.

[48] Sun, Y., et al., 2012. Micro energy director array in ultrasonic precise bonding for thermoplastic micro assembly. Journal of Materials Processing Technology, 212/6: 1331-1337.

[49] Yang, L., et al., 2011. Self-assembly of three-dimensional microstructures in MEMS via fluxless laser reflow soldering. International Conference on Electronic Packaging Technology and High Density Packaging, 12: 1-4.

[50] SUN, L., et al., 2006. Localized CO_2 laser bonding process for MEMS packaging. Transactions of Nonferrous Metals Society of China, 16: 577-581.

[51] Arnold, C. B., and Piqué, A., 2007. Laser direct-write processing. MRS Bulletin, 32/01: 9-15.

[52] Bohandy, J., et al., 1986. Metal deposition from a supported metal film using an excimer laser. Journal of Applied Physics, 60: 1538-1539.

[53] Arnold, C. B., et al., 2007. Laser direct-write techniques for printing of complex materials. MRS Bulletin, 32/01: 23-31.

[54] Gower, M. C., 2001. Laser micromachining for manufacturing MEMS devices. MEMS Components and Applications for Industry, Automobiles, Aerospace, and Communication, 4559: 53-59.

[55] Abbott, C., et al., 2002. New techniques for laser micromachining MEMS devices. International Symposium on High-Power Laser Ablation, 4760: 281-288.

[56] Minami, K., et al., 1993. YAG laser assisted etching for releasing silicon micro structure. Micro Electro Mechanical Systems, 93: 53-58.

[57] Allen, S., et al., 1982. Direct writing using laser chemical vapor deposition. MRS Proceedings, 17: 207-214.

[58] Ikuta, K., and Hirowatari, K., 1993. Real three dimensional micro fabrication using stereo lithography and metal molding. Micro Electro Mechanical Systems, 93: 42-47.

[59] Holmes, A. S., et al. 2000. Laser-assisted assembly for hybrid microelectromechanical systems. Laser Microfabrication-ICALEO, D1-D9.

[60] Holmes, A. S., and Saidam, S. M., 1998. Sacrificial layer process with laser-driven release for batch assembly operations. Journal of Microelectromechanical Systems, 7/4: 416-422.

[61] Spletter, P., 1990. A laser based system for tape automated bonding to integrated circuits. Electronic Components and Technology Conference, 40: 757-761.

[62] Krebs, H., et al., 2003. Advances in solid state physics. Springer, 40: 505-518.

[63]   Abraham, M., et al., 1995. Laser LIGA: a cost-saving process for flexible production of microstructures. Micromachining and Microfabrication Process Technology, 2639: 164-173.

[64]   Fujita, M., et al., 2009. Low stress dicing assisted by pulsed laser for multilayer MEMS. SPIE Laser-based Micro- and Nanopackaging and Assembly, 72020F-7.

[65]   Sameshima, T., et al., 1986. XeCl excimer laser annealing used in the fabrication of poly-Si TFT's. IEEE Electron Device Letters, 7/5: 276-278.

[66]   Grum, J., 2007. Comparison of different techniques of laser surface hardening. Journal of Achievements in Materials and Manufacturing Engineering, 24/1: 17-25.

[67]   Liu, Y., et al., 2009. Temperature monitoring in laser assisted polymer bonding for MEMS packaging using a thin film sensor array. IEEE Sensors Applications Symposium, 52-55.

[68]   Chediak, J. A., et al., 2003. Heterogeneous integration of CdS filters with GaN LEDs for fluorescence detection microsystems. Sensors and Actuators A: Physical, 111/1:1-7.

[69]   Atre, A. C., and Arnold, C. B., 2011. $LiCoO_2$ texturing by laser induced forward transfer for printed microbatteries. Laser-based Micro- and Nanopackaging and Assembly, 5: 79210o-8.

[70]   Wartena, R., et al., 2004. Li-Ion microbatteries generated by a laser direct-write method. Journal of Power Sources, 126/1:193-202.

[71]   Brown, M. S., et al., 2011. Time-resolved dynamics of laser-induced micro-jets from thin liquid films. Microfluidics and Nanofluidics, 11/2: 199-207.

[72]   Kattamis, N. T., et al., 2009. Laser direct write printing of sensitive and robust light emitting organic molecules. Applied Physics Letters, 94: 1033063.

[73]   Piqué, A., et al., 1999. A novel laser transfer process for direct writing of electronic and sensor materials. Applied Physics A, 69/1: 279-284.

[74]   Piqué, A., et al., 2000. Direct writing of electronic and sensor materials using a laser transfer technique. Journal of Materials Research, 15/9: 1872-1875.

[75]   Duocastella, M., et al., 2008. Laser-induced forward transfer of liquids for miniaturized biosensors preparation. Journal of Laser Micro Nanoengineering, 3/1:1-4.

[76]   Mailis, S., et al., 2009. Laser-induced-forward-transfer: a rapid prototyping tool for fabrication of photonic devices. Applied Physics A, 101/2: 333-338.

[77]   Schultze, V., and Wagner, M., 1991. Laser-induced forward transfer of aluminium. Applied Surface Science, 52/4: 303-309.

[78]   Kantor, Z., et al., 1992. Laser induced forward transfer: the effect of support-film interface and film-to-substrate distance on transfer. Applied Physics A, 54/2: 170-175.

[79] Kantor, Z., et al., 1994. Deposition of micrometer-sized tungsten patterns by laser transfer technique. Applied Physics Letters, 64/25: 3506-3508.

[80] Sano, T., et al., 2002. Experimental investigation of laser induced forward transfer process of metal thin films. Applied Surface Science, 186/1: 221-226.

[81] Zergioti, I., et al., 1998. Microdeposition of metal and oxide structures using ultrashort laser pulses. Applied Physics A: Materials Science & Processing, 66/5: 579-582.

[82] Greer, J. A., and Parker, T. E., 1988. Laser-induced forward transfer of metal oxides to trim the frequency of surface acoustic wave resonator devices. Proceeding SPIE, Excimer Beam Applications, 0998: 113-125.

[83] Chakraborty, S., et al., 2007. Laser-induced forward transfer technique for maskless patterning of amorphous V_2O_5 thin film. Applied Surface Science, 254/2: 638-643.

[84] Klini, A., et al., 2007. ZnO nanorod micropatterning via laser-induced forward transfer. Applied Physics A, 87/1: 17-22.

[85] Fogarassy, E., et al., 1989. Laser-induced forward transfer of high-T_C YBaCuO and BiSrCaCuO superconducting thin films. Journal of Applied Physics, 66/1: 457-459.

[86] Palla-Papavlu, A., et al., 2011. Laser induced forward transfer for materials patterning. Romanian Reports in Physics, 63:1285-1301.

[87] Fernández-Pradas, J., et al., 2004. Laser-induced forward transfer of biomolecules. Thin Solid Films, 453: 27-30.

[88] Boutopoulos, C., et al., 2010. Polymer/carbon nanotube composite patterns via laser induced forward transfer. Applied Physics Letters, 96/4: 041104-3.

[89] Kononenko, T. V., et al., 2009. Laser transfer of diamond nanopowder induced by metal film blistering. Applied Physics A, 94/3: 531-536.

[90] Rigout, M. L., et al., 2008. Fabrication and photoluminescence of hyperbranched silicon nanowire networks on silicon substrates by laser-induced forward transfer. Nanotechnology, 19/24: 245303-5.

[91] Wang, L., et al., 2013. Silicon solar cells based on all-laser-transferred contacts. Progress in Photovoltaics: Research and Applications, DOI: 10.1002.

[92] Mathews, S. A., et al., 2007. Use of laser direct-write in microelectronics assembly. Journal of Laser Micro/Nanoengineering, 2/1:103-107.

[93] Kim, T., et al., 2009. Kinetically controlled, adhesiveless transfer printing using microstructured stamps. Applied Physics Letters, 94/11: 113502-3.

[94] Kim, S., et al., 2012. Enhanced adhesion with pedestal-shaped elastomeric stamps for transfer printing. Applied Physics Letters, 100/17: 171909-4.

[95]   Carlson, A., et al., 2011. Shear-enhanced adhesiveless transfer printing for use in deterministic materials assembly. Applied Physics Letters, 98/26: 264104-3.

[96]   Carlson, A., et al., 2012. Active, programmable elastomeric surfaces with tunable adhesion for deterministic assembly by transfer printing. Advanced Functional Materials, 22/21: 4476-4484.

[97]   Li, R., et al., 2012. Axisymmetric thermo-mechanical analysis of laser-driven non-contact Transfer printing. International Journal of Fracture, 176/2: 189-194.

[98]   Philipp, S., et al., 2013. Effects of mechanical layering on hydrofracture emplacement and fluid transport in reservoirs. Frontiers in Earth Science, DOI: 10.3389.

[99]   Rice, J. R., 1968. A path independent integral and the approximate analysis of strain concentration by notches and cracks. Journal of Applied Mechanics, 35/2: 379-386.

[100]   Nakamura, T., and Parks, D., 1992. Determination of elastic T-stress along three-dimensional crack fronts using an interaction integral. International Journal of Solids and Structures, 28: 1597-1611.

[101]   Suo, Z., 1989. Singularities interacting with interfaces and cracks. International Journal of Solids and Structures, 25/10: 1133-1142.

[102]   Feng, X., et al., 2007. Competing fracture in kinetically controlled transfer printing. Langmuir, 23:12555-12560.

[102]   Yang S., et al., 2012. Elastomer surfaces with directionally dependent adhesion strength and their use in transfer printing with continuous roll-to-roll applications. Advanced Materials, 24/16: 2117-2122.

[104]   Reeder, J., 1992. 3D mixed-mode delamination fracture criteria-an experimentalist's perspective. NASA Technical Memorandum, 104210.

[105]   Feng, Y., and Wu, L., 2001. Analysis of interfacial thermal stresses of chip-substrate structure, 38/9: 1551-1562.

[106]   Kang L., 1995. Thermal stress intensity factors for partially insulated interface crack under uniform heat flow. Engineering Fracture Mechanics, 50/4: 475-482.

[107]   Sundaram, S., 2013. The Influence of transient thermal gradients and substrate constraint on delamination of thermal barrier coatings, Journal of Applied Mechanics, 80: 011002-13.

[108]   Lu, K., 2010. Thermal stress induced delamination of through silicon vias in 3-D interconnects. Electronic Components and Technology Conference, 60: 40-45.

[109]   Tran, P., et al., 2010. Dynamic delamination of patterned thin films: a numerical study. International Journal of Fracture, 162:77-90.

[110] Wang, J., et al., 2004. Tensile and mixed-mode strength of a thin film-substrate interface under laser induced pulse loading. Journal of the Mechanics and Physics of Solids, 52/5: 999-1022.

[111] Maiti, S., and Geubelle, P., 2005. A cohesive model for fatigue failure of polymers. Engineering Fracture Mechanics, 72/5:691-708.

[112] Barenblatt, G., 1959. The formation of equilibrium cracks during brittle fracture. Journal of Applied Mathematics and Mechanics, 23/3: 622-636.

[113] Shet, C., and Chandra, N., 2002. Analysis of energy balance when using cohesive zone models to simulate fracture processes. Journal of Engineering Materials and Technology, 124/4: 440-450.

[114] Hattiangadi, A., and Siegmund, T., 2004. Thermomechanical cohesive zone models for analysis of composites failure under thermal gradients and transients. Mechanics of Microstructured Materials, 464: 57-86.

[115] Li, X., 2012. Cohesive zone model for delamination analysis of an embedded die system in package. Thermal, Mechanical and Multi-Physics Simulation and Experiments in Microelectronics and Microsystems, 13: 1-10.

[116] Caminoa, G., et al., 2001. Polydimethylsiloxane thermal degradation part 1. kinetic aspects. Polymer, 42/6: 2395-2402.

[117] Tomer, N., et al., 2012. Oxidation, chain scission and cross-linking studies of polysiloxanes upon ageings. Open Journal of Organic Polymer Materials, 2: 13-22.

[118] Malyarchuk, V., et al., 2005. High performance plasmonic crystal sensor formed by soft nanoimprint lithography. Optics Express, 13/15: 5669-5675.

[119] Huang, Y., et al., 2005. Stamp collapse in soft lithography. Langmuir, 21/17: 8058-8068.

APPENDIX A

The optical absorption mode described in Section 4.5 assumes uniform heating for silicon ink to estimate the power absorbed by the ink. In case the ink is larger than the beam flat-top area and the laser beam profile can be approximate to be perfect Gaussian shape, the power intensity of the beam at the focused plane in the polar coordinate system is given by Eq. (A.1):

$$I(r, \theta) = I_o e^{-2r^2/w_o^2} \tag{A.1}$$

Further, the laser beam intensity at the center axis is given by Eq. (A.2):

$$I_o = \frac{2P_o}{\pi w_o^2} \tag{A.2}$$

Where P_o and w_o are the Gaussian beam power and the beam radius. Therefore, the laser beam power portion passes through a circular aperture with radius r_o is given by Eq. (A.3):

$$P_a = \int_0^{r_0} 2\pi \, I(r, \theta) r dr = \frac{\pi I_o w_o^2}{2}(1 - e^{-2r_o^2/w_o^2}) \tag{A.3}$$

On the other hand, if the ink has a square shape, the laser beam power portion passes through a square aperture with size L_s is given by Eq. (A.4):

$$P_a = \int_{-\frac{L_s}{2}}^{\frac{L_s}{2}} \int_{-\frac{L_s}{2}}^{\frac{L_s}{2}} I_o e^{-2(x^2+y^2)/w_o^2} dxdy = P_o erf^2(\frac{L_s}{\sqrt{2} w_o}) \tag{A.4}$$

The power density absorbed by the silicon ink for each pass is given by Eq. (A.5):

$$Q_i(r, \theta, z) = \begin{cases} R_i(1 - R_T)\alpha I(r, \theta)e^{-\alpha z} ; & i \, odd \\ R_i(1 - R_T)\alpha I(r, \theta)e^{-\alpha(h_s-z)}; & i \, Even \end{cases} \tag{A.5}$$

Integrating the power density over the ink volume (ink area A_o; and ink thickness h_s) gives the total power absorbed by each absorption path as shown in Eq. (A.6):

$$P_i = R_i(1 - R_T)P_a e^{-(i-1)\alpha h_s}[1 - e^{-\alpha h_s}] \tag{A.6}$$

APPENDIX B

The viscoelastic properties of the PDMS as a function of the PDMS bulk temperature are measured using a Dynamic Mechanical Analysis (DMA) machine. The results (see Fig. B.1) show that the PDMS tends to loss its viscous properties (lower loss modulus and higher storage modulus) when the bulk temperature is higher than $200^{\circ}C$. These experiments are conducted in atmospheric controlled temperature test environments. Further, the PDMS sample after the test, where high temperatures up to $550^{\circ}C$ are used, tends to be brittle and easy to fracture.
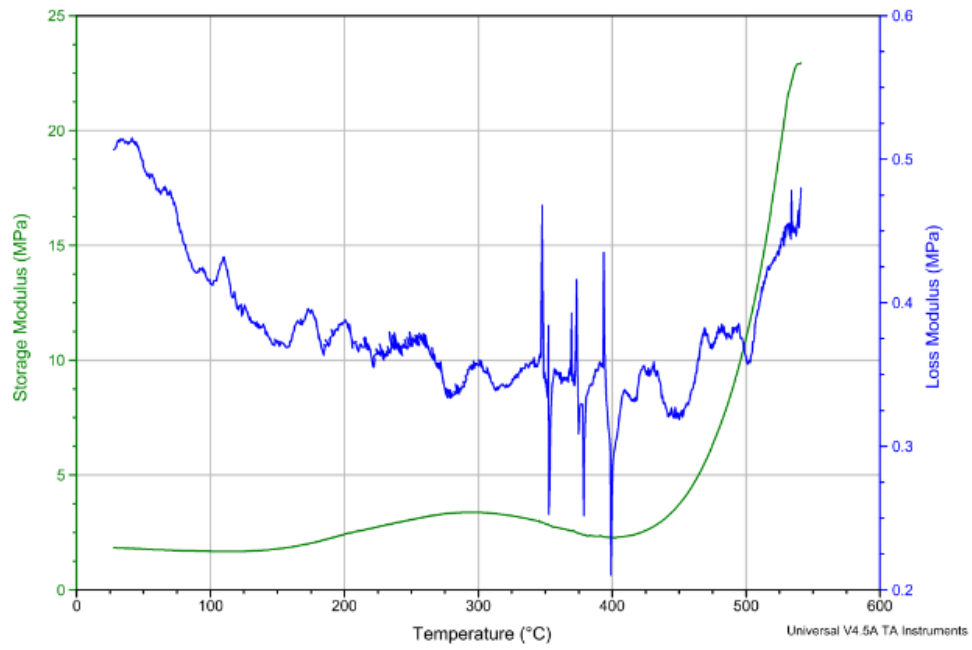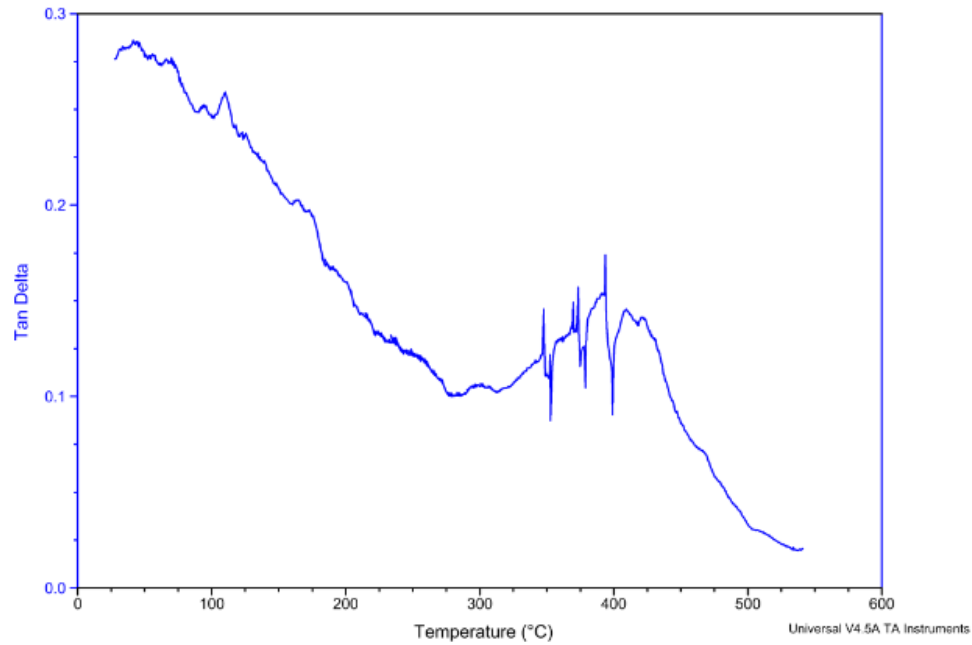
Figure B.1. Viscoelastic properties of PDMS as a function of the bulk temperature, (a) storage and loss modulus, and (b) tan delta.